

**Could Global Warming Affect Space Weather?
Case Studies of Intense Ionospheric Plasma
Turbulence Associated with Natural Heat Sources**

by
Rezy Pradipta

B.S. Physics, Massachusetts Institute of Technology (2006)

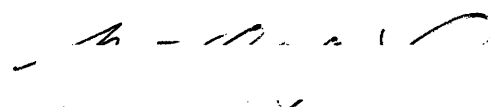
Submitted to the Department of Nuclear Science and Engineering
in partial fulfillment of the requirements for the degree of
Master of Science in Nuclear Science and Engineering
at the



MASSACHUSETTS INSTITUTE OF TECHNOLOGY


September 2007

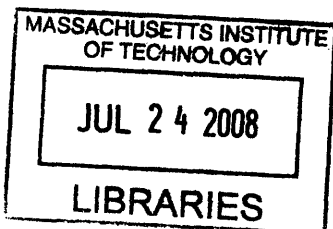
© Massachusetts Institute of Technology 2007. All rights reserved.

Author ...
Department of Nuclear Science and Engineering
August 27, 2007

Certified by: 
Prof. Min-Chang Lee
Head, Ionospheric Plasma Research Group
Plasma Science and Fusion Center
Thesis Supervisor

Read by
 Prof. Jeffrey P. Freidberg
Associate Director, Plasma Science and Fusion Center
Department of Nuclear Science and Engineering
 Thesis Reader

Accepted by
 Prof. Jeffrey A. Coderre
Chairman, Committee for Graduate Students
Department of Nuclear Science and Engineering



ARCHIVES

Could Global Warming Affect Space Weather?
Case Studies of Intense Ionospheric Plasma Turbulence
Associated with Natural Heat Sources

by

Rezy Pradipta

Submitted to the Department of Nuclear Science and Engineering
on August 27, 2007, in partial fulfillment of the
requirements for the degree of
Master of Science in Nuclear Science and Engineering

Abstract

We report on observations of a series of highly-structured ionospheric plasma turbulence over Arecibo on the nights of 22/23 and 23/24 July, 2006. Incoherent scatter measurements by Arecibo radar, airglow measurements using MIT PSFC's all-sky imaging system (ASIS), together with TEC measurements from GPS satellite network provide well-integrated diagnostics of turbulent plasma conditions. Two kinds of turbulent structures were seen as slanted stripes and filaments/quasi-periodic echoes on the range-time-intensity (RTI) plots of radar measurements. Detailed analyses of radar, airglow, and GPS data allow us to determine the drift velocity/direction, the orientation/geometry, and the scale lengths of these plasma turbulence structures. They are large plasma sheets with tens of kilometer scale lengths, moving in the form of traveling ionospheric disturbances (TIDs) southward within the meridional plane or westward in zonal plane at tens of meter per second. The signatures of observed TIDs indicate that they were triggered by internal gravity waves that had reached the altitudes of ionospheric F region. All possible sources producing gravity waves have been examined. We rule out solar/geomagnetic conditions which were quiet, and the atmospheric weather anomalies which were absent, during the period of time for our experiments. It is found that the heat wave fronts, which occurred in US, were plausible sources of free energy generating intense gravity waves and triggering large plasma turbulence over Arecibo. In other words, anomalous heat sources can be responsible for the occurrence of intense space plasma turbulence all over the world. The reported research suggests that global warming may affect the space weather conditions significantly. Further GPS data analysis is outlined as our future efforts to verify some predictions based on the current research outcomes. Simulation experiments can be conducted at Gakona, Alaska using the powerful high-frequency active auroral research programs (HAARP) heating facility, to generate gravity waves for the controlled study of concerned intriguing phenomenon.

Thesis Supervisor: Prof. Min-Chang Lee
Title: Head, Ionospheric Plasma Research Group
Plasma Science and Fusion Center

Acknowledgments

First of all, I would like to thank Professor Min-Chang Lee as my thesis supervisor for his selfless support, guidance, and encouragement for me to accomplish this work. For many years, Professor Lee has been extraordinarily supportive to all of his undergraduate and graduate students. Many thanks also to my fellow students Joel Cohen, Laura Burton, and Anna Labno for their teamwork and invaluable help during Arecibo and/or HAARP experiments in the past years. They have been very pleasant to work and exchange ideas with. Finally, I would like to thank Professor Jeffrey P. Freidberg for becoming my thesis reader.

In addition, I would like to thank Dr. David L. Byers and Dr. Kent L. Miller from the Air Force Office of Scientific Research (AFOSR) for their generous and continuous support to our space/ionospheric plasma research program here at MIT PSFC. This thesis work has been sponsored by the Air Force Office of Scientific Research (AFOSR) through the AFOSR grant FA9550-05-1-0091 [Program managers: Dr. David L. Byers and Dr. Kent L. Miller (earlier)].

The Arecibo Observatory is the principal facility of the National Astronomy and Ionosphere Center, which is operated by the Cornell University under a cooperative agreement with the National Science Foundation.

Contents

1	Introduction	17
1.1	Background and Motivations	17
1.2	Summary of The Observed Phenomena	19
1.3	Proposed Hypothesis	23
2	Ionospheric Disturbances: An Overview	25
2.1	Internal Gravity Waves	25
2.2	Sporadic-E Plasma Layer and Kelvin-Helmholtz Instability	28
2.3	Ionospheric Disturbances Induced by Gravity Waves	32
3	Airglow Diagnostics	35
3.1	Ionospheric Plasma Diagnostics Through Airglow Measurement	35
3.2	All-Sky Airglow Measurement on The Night of 22/23 July 2006	38
3.3	All-Sky Airglow Measurement on The Night of 23/24 July 2006	40
3.3.1	Observation of a Southward Airglow Motion	40
3.3.2	Observation of a Westward Airglow Motion	42
4	Incoherent Scatter Radar Diagnostics	45
4.1	Overview of ISR Measurement Basics	45
4.2	ISR Measurement on 22/23 July 2006	47
4.2.1	Observation of Slanted Stripe Structure	48
4.2.2	Observation of a Train of Turbulent Filaments	50
4.3	ISR Measurement on 23/24 July 2006	52

4.3.1	Observation of Slanted Stripe Structures	52
4.3.2	Observation of Filament Structures/ Quasi-Periodic Echoes . .	54
5	GPS TEC Diagnostics	57
5.1	The Basics of TEC Measurement using GPS Network	57
5.2	TID Signatures on GPS TEC Signals for 22/23 July 2006 and 23/24 July 2006	59
5.3	Detailed Analysis of GPS TEC Signal from GPS Satellite #8 on 23/24 July 2006	62
6	Data Discussion	67
6.1	Combined Analysis of Airglow and ISR Diagnostics	67
6.1.1	Train of Turbulent Filaments on The Night of 22/23 July 2006 — Westward Airglow Motion	69
6.1.2	Slanted Stripes on The Night of 23/24 July 2006 — Southward Airglow Motion	70
6.1.3	Filament Structures on The Night of 23/24 July 2006 — West- ward Airglow Motion	71
6.2	The Search for Possible Gravity Wave Sources	72
7	Conclusion and Future Research	79
A	Geocoordinate Transformations for All-Sky Imaging Data	83
A.1	Data Array Manipulations	83
A.2	Determining Center Pixel and Image Radius	87
B	Airglow Structure Tracking	91

List of Figures

1-1	Sheet-like ionospheric plasma irregularities generated by Arecibo HF heater during the 1997 heating experiment. From <i>Lee et al.</i> [1998].	18
1-2	The observed slanted stripes on the RTI display of Arecibo ISR backscatter power data on the night of 23/24 July 2006. A dense and wavy sporadic E layer was also observed on that night.	20
1-3	All-sky imager data for 6300 Å airglow emission recorded on the night of 23/24 July 2006, indicating a plasma structure drifting southward.	21
1-4	Summer 2006 North American heat waves as mapped by NASA's Clouds and the Earth's Radiant Energy System (CERES). The heat waves swept across from the Northwest toward the Southeast. Figure taken from <i>Atmospheric Science Data Center</i> [2006].	23
2-1	Neutral wind speed fluctuations associated with internal gravity waves at meteor heights (upper left & upper right). A pictorial illustration of internal gravity wave amplitude growth and its phase/energy propagation (bottom). After <i>Hines</i> [1960].	26
2-2	(a) A diagram showing the direction of ion motion under the influence of neutral wind in a collisional magnetized plasma. (b) Schematic illustration of the wind shear mechanism for sporadic E layer formation. Adapted from <i>Kelley</i> [1989].	30
2-3	Examples of Kelvin-Helmholtz billows that could develop in the sporadic E plasma layer due to a strong wind shear.	31

2-4	Sample contour plots that describe the induced plasma density fluctuations during the passage of internal gravity waves in the ionosphere for two different orientations of wavevector relative to the magnetic field. Taken from <i>Hooke</i> [1968].	33
3-1	A portion of energy level diagram for atomic oxygen showing specific transitions that give rise to the 5577 Å and 6300 Å OI emission, which is commonly used for airglow diagnostics of ionospheric plasmas. Adapted from <i>Carlson and Egeland</i> [1995].	36
3-2	A map of Puerto Rico and the surrounding islands in the Caribbean area. The 1200 km × 800 km frame represents the coverage area of 6300 Å airglow measurement using ASIS at Arecibo Observatory. . .	37
3-3	Three airglow intensity maps from the night of 22/23 July 2006 which were recorded at 03:29:07 LT, 04:07:07 LT, and 04:21:07 LT. These airglow structures had an approximately westward direction of motion during this time period.	38
3-4	Airglow structure tracking analysis for the ~westward moving airglow on the night of 22/23 July 2006. The airglow speed was calculated to be 46.3 ± 2 m/s.	39
3-5	Three airglow intensity maps from the night of 23/24 July 2006 which were recorded at 22:41:07 LT, 23:05:07 LT, and 23:23:07 LT. These airglow structures had an approximately southward direction of motion during this time period.	40
3-6	Airglow structure tracking analysis for the ~southward moving airglow on the night of 23/24 July 2006. The airglow speed was calculated to be 97.3 ± 7 m/s.	41
3-7	Three airglow intensity maps from the night of 23/24 July 2006 which were recorded at 02:13:07 LT, 02:53:07 LT, and 03:17:07 LT. These airglow structures had an approximately westward direction of motion during this time period.	42

3-8	Airglow structure tracking analysis for the ~westward moving airglow on the night of 23/24 July 2006. The airglow speed was calculated to be 67.3 ± 5 m/s.	43
4-1	A schematic illustration of incoherent scatter frequency spectrum.	46
4-2	A sample ISR backscatter power profile together with the derived ionospheric plasma density profile. Signatures of plasma structures can be seen as dips/depletions (marked by the red arrows) in both backscatter power and plasma density profile. Note that the signatures can be seen better in the backscatter power profile.	47
4-3	RTI plot of radar backscatter power during time period 22:30 LT – 23:30 LT on the night of 22/23 July 2006, showing a slanted stripe structure at ionospheric F region altitudes.	48
4-4	RTI plot of net backscatter power perturbations that correspond to the slanted stripe structures observed on the night of 22/23 July 2006 during time period 22:30 LT – 23:30 LT.	49
4-5	RTI plot of radar backscatter power during time period 01:30 LT – 03:30 LT on the night of 22/23 July 2006. A train of turbulent filaments in the F region can be seen from this data set.	50
4-6	Detailed look at a specific portion of the turbulent filaments.	51
4-7	RTI plot of radar backscatter power during time period 22:00 LT – 23:00 LT on the night of 23/24 July 2006, showing some of the observed slanted stripes.	52
4-8	RTI plot of net backscatter power perturbations on the night of 23/24 July 2006 during time period 22:00 LT – 23:00 LT. In this RTI plot, four slanted stripe structures can be identified.	53
4-9	RTI plot of radar backscatter power during time period 03:40 LT – 04:00 LT on the night of 23/24 July 2006, where filament structures/quasi-periodic echoes were seen at ionospheric F region altitudes.	54

4-10	RTI plot of net backscatter power perturbations on the night of 23/24 July 2006 during time period 03:40 LT - 04:00 LT. The filaments/quasi-periodic echoes can now be seen much more clearly. Red arrow marks a particular filament that we used for slope estimation.	55
5-1	A diagram showing the geometry of total electron content (TEC) measurements made by pairs of GPS satellite and receiver station. . . .	58
5-2	Several selected plots of GPS TEC measurement made by the GPS receiver station in Isabella, PR on 23 July 2006 UTC in which TID signatures (wavelike fluctuations in the TEC signal) were seen. . . .	60
5-3	Several selected plots of GPS TEC measurement made by the GPS receiver station in St. Croix, USVI on 24 July 2006 UTC in which TID signatures (wavelike fluctuations in the TEC signal) were seen.	61
5-4	Absolute TEC measurement on 24 July 2006 UTC from GPS satellite #8 by Isabella GPS receiver station (upper panel). The corresponding TEC perturbation (TECP) from this measurement after the background signals were removed (lower panel).	63
5-5	A comparison between TECP signals from GPS receiver station in Isabella, PR (upper panel) and St. Croix, USVI (lower panel). The red arrows mark the corresponding TID signatures that can be identified in both TECP signals.	64
5-6	Trajectory lines of GPS satellite #8's ionospheric piercing points that correspond to TEC measurements made by Isabella and St. Croix GPS receiver stations, respectively. Also shown along these trajectories are the locations where each of the corresponding TID signatures A-E (Isabella station) and A'-E' (St. Croix station) were detected.	65
6-1	The geometry of plasma density striations when the TID structures are progressing southward.	69
6-2	The geometry of plasma density striations when the TID structures are progressing westward.	70

6-3	Summary plots of space weather condition on 21-27 July 2006 from NOAA's Space Physics Interactive Data Resource (SPIDR) database [2006]. Low values of A_p and K_p indices show that the geomagnetic condition was quiet during our experiment.	72
6-4	Hurricane track map for the 2006 Atlantic hurricane season [<i>National Hurricane Center, 2006</i>]. No major hurricane had passed near Puerto Rico during our experiment.	74
6-5	The progression of summer 2006 North American heat waves on 20–25 July 2006. Data from the National Climatic Data Center, NOAA [2006].	76
7-1	North American and West European heat waves during summer 2006 as mapped by the Moderate Resolution Imaging Spectroradiometer (MODIS) on NASA's Terra satellite [2006].	80
A-1	A schematic description of the first two steps of the required array manipulations before a more intensive analysis can be performed on the ASIS airglow data.	84
A-2	Transformations from the top-view array $\mathbf{A3}$ into the geographical array \mathbf{G} . Matrix element $\mathbf{A3}(i,j)$ from top-view array will become matrix element $\mathbf{G}(i',j')$ in geographical array.	85
A-3	Basic geometry relating the height of airglow layer to the horizontal extent of airglow measurement using an all-sky imager.	86
A-4	Contour map of a sample airglow intensity data recorded using ASIS. The image edge is located at the transition between the area where the contour is clean and the area where clusters of random dark noise start to develop. Center pixel and image radius is determined through analytical curve fitting of the image edge.	88
A-5	Curve fitting results of ASIS image edge for the lower arc (left) and for the upper arc (right), respectively.	90

B-1 Basic schematics of the airglow structure tracking procedures. The distinctive part of airglow structure is “locked-on” first in Datafile #1. We will then locate the new position of this structure in Datafile #2 onwards by scanning the “lock-on” frame around, looking for the best-matched pattern. 92

B-2 A sample likelihood surface plot that was obtained after scanning an ASIS snapshot. In each ASIS snapshots following the reference snapshot, the tracked airglow structure position is found by locating the coordinate (X_i, Y_i) where the likelihood is maximum. 93

B-3 A plot of the tracked airglow structure positions from a number of ASIS snapshots following a particular reference snapshot. This airglow trail is the end result of the first stage in our tracking procedures. . . 94

B-4 A sample linear regression result in determining the overall airglow motion direction from the airglow trails. Also shown in the figure is a schematic illustration of the *reference point* and the *null point* that are used in the “projection” procedures as a preliminary step for determining the speed of airglow motion. 95

B-5 Determining the airglow motion speed through curve fitting. Most of the time, we only need linear regression since the airglow motion speed is \sim constant. 96

List of Tables

- 1.1 Arecibo ISR observation summary for our experiment on the night of 22/23 and 23/24 July 2006. 22
- 1.2 ASIS airglow observation summary for our experiment on the night of 22/23 and 23/24 July 2006. 22

- A.1 The values for the center pixel and the image radius that were obtained from the curve fitting of the image edge. Shown are the individual fitting parameter results from upper and lower arc, together with the weighed average of the two results. 89

Chapter 1

Introduction

On 21 March former US Vice President Al Gore delivered his testimony for the US House of Representatives regarding the issue of global warming and climate crisis [Gore, 2007]. There have been indications that higher atmospheric temperatures associated with global warming may cause various ecological effects such as the occurrences of more intense weather anomalies and the rise of sea levels due to melting of polar cap ice. These are a few examples of observable effects on the Earth's surface (litosphere/hydrosphere) and in the lower atmosphere (troposphere). We can now ask another question: are there any effects that global warming may impose on space plasmas? This would involve regions even farther away from the Earth's surface (e.g. upper atmosphere, ionosphere, and probably magnetosphere). This thesis will discuss our observation of intense ionospheric plasma disturbances that could have been closely linked to the summer 2006 US heat wave—one of the most recent indication of global warming.

1.1 Background and Motivations

Plasma turbulence is a topic of great interest in both space plasma and fusion research. In most cases, plasma turbulence is something that we want to avoid because it can pose serious problems (e.g. radio communication blackouts due to space plasma disturbances, disruptions in fusion processes). Therefore, it is important for us to

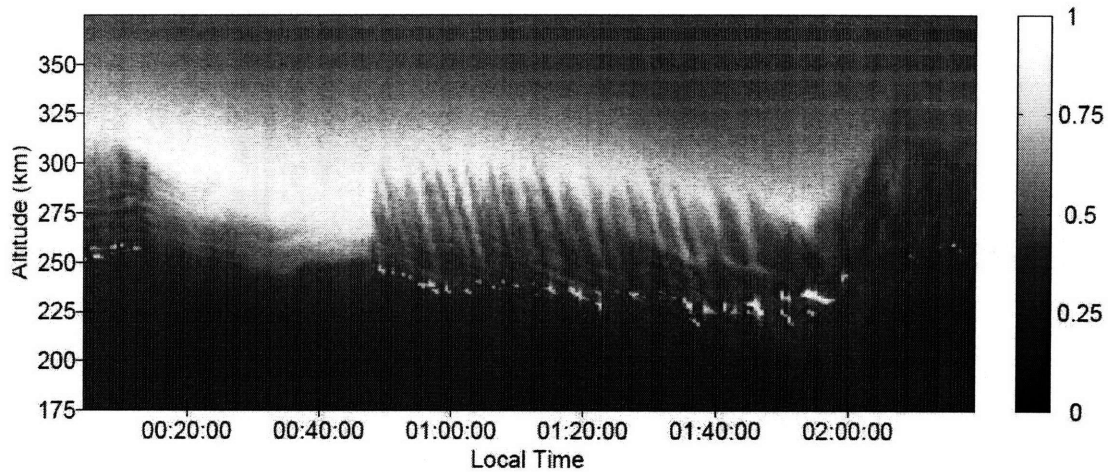


Figure 1-1: Sheet-like ionospheric plasma irregularities generated by Arecibo HF heater during the 1997 heating experiment. From *Lee et al.* [1998].

study the nature and the source of plasma turbulence. With a good understanding on this subject matter, we would be able to prevent any potential problems from occurring.

In general, space plasma turbulence can be excited by either natural or man-made sources. Artificial space plasma disturbances are often generated during controlled-studies of space plasma using ground-based radio frequency (RF) heater, as an attempt to study various aspects of physics involved in the plasma turbulence. During the 1997 experimental campaign at the Arecibo Observatory, sheet-like plasma density irregularities were formed at ionospheric F region altitudes as a result of injection of powerful high-frequency (HF) heater waves [*Lee et al.*, 1998]. These parallel-plate structures were successfully detected by the Arecibo incoherent scatter radar (ISR) as they drifted westward. In the radar backscatter power data, these parallel-plate structures appeared as slanted stripes, as depicted in Figure 1-1.

While Arecibo HF heater could generate artificial parallel-plate plasma structures, we also had observed a few cases of highly-structured naturally-occurring ionospheric plasma disturbances over Arecibo in our most recent (July 2006) experiments. Some of these natural ionospheric plasma disturbances were detected by the Arecibo ISR as slanted stripes, which means that they were also sheet-like plasma structures—just

like the heater-generated plasma irregularities in 1997 Arecibo heating experiment. More interestingly, these highly-structured ionospheric plasma turbulence were observed during geomagnetically quiet nights. It is thus a challenge for us to pinpoint the source of these disturbances. On the bright side, however, we might be able to identify new interesting sources that had not been noticed before.

1.2 Summary of The Observed Phenomena

During our experimental campaign at the Arecibo Observatory on 21–27 July 2006, we observed a very turbulent ionosphere on some of the nights. Based on the data from our diagnostics instruments, there had been some indications of a turbulent plasma state at the beginning of our experiment, prior to the occurrence of fully-developed turbulent plasma structures.

First, ionosonde measurement shows that the ionospheric F region peak plasma frequency early in the evening was quite high (around 8 MHz or so) on most nights. This was unusual because we are currently in the solar minimum. High plasma density early in the evening indicates that recombination process in the F region was very slow at that time. From the all-sky imager data, we also observed a post-twilight enhancement for the 6300 Å airglow emission on those nights, which confirmed that the recombination rate in the ionospheric F region was indeed very slow at that time. High plasma density in general will lower the threshold for various plasma instabilities in the ionosphere.

Second, shortly after the F region peak plasma frequency fall into its normal nighttime value (around 3-4 MHz) later in the evening, sharp density gradients often formed at the bottomside ionosphere. This will enhance the possibility for the (generalized) Rayleigh-Taylor instability to develop. Following the formation of this sharp density gradient, often there was also some intermediate (peel-off) plasma layers that separated and descended from ionospheric F region into E region altitudes.

Finally, we also observed intense sporadic E plasma layers around an altitude of 110–120 km, with wavelike structures embedded in those layers. This would be an in-

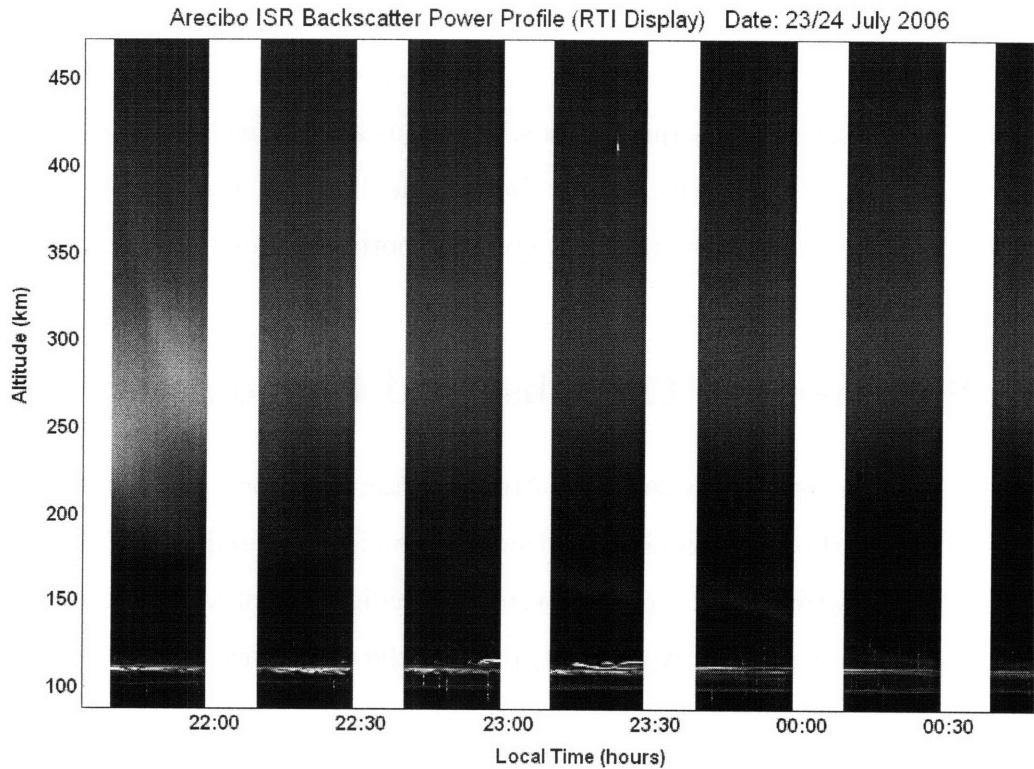


Figure 1-2: The observed slanted stripes on the RTI display of Arecibo ISR backscatter power data on the night of 23/24 July 2006. A dense and wavy sporadic E layer was also observed on that night.

dication of a strong neutral wind shear which formed the layer and excite the wavelike structures via Kelvin-Helmholtz instability. The presence of such strong neutral wind shear also implies an intense perturbation in the neutral atmosphere, most likely in the form of internal gravity waves, that could even couple into ionospheric F region plasmas and produce some traveling ionospheric disturbances (TID).

One of the most prominent plasma structures that we observed was the slanted stripe pattern that appeared on the night of 23/24 July 2006, as shown in the Range-Time-Intensity (RTI) plot of Arecibo ISR data (Figure 1-2). These slanted stripes, which appeared for almost 3 hours in the Arecibo ISR data, were downward-sloping. Such slanted stripe pattern is typically caused by sheet-like plasma structures that move across the radar beam. Since plasma density irregularities must be field-aligned and because the radar beam was pointed vertically during our experiment, then we may deduce that these sheet-like plasma structures were tilted following the magnetic

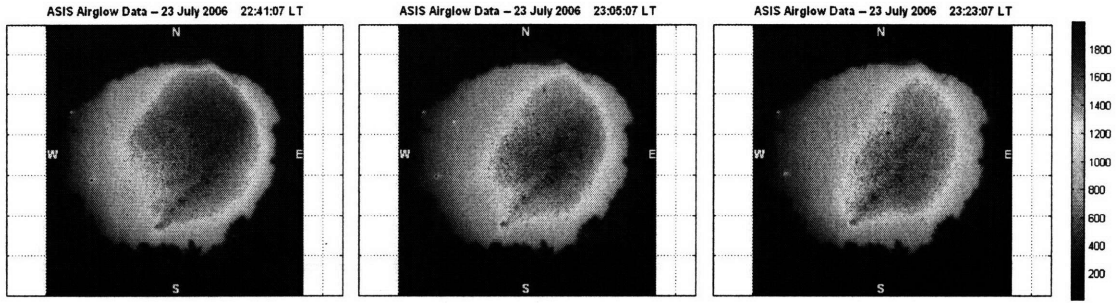


Figure 1-3: All-sky imager data for 6300 \AA airglow emission recorded on the night of 23/24 July 2006, indicating a plasma structure drifting southward.

dip angle ($\sim 50^\circ$ at Arecibo) while drifting southward and downward perpendicularly across the magnetic field lines. This is one of the simplest configuration that will result in downward sloping stripes in the RTI plot of Arecibo ISR data.

The above conjecture was also consistent with the airglow measurement made by our all-sky imager. In the 6300 \AA airglow data, we observed an airglow structure which moved in the \sim southward direction during the time period of interest. Depicted in Figure 1-3 is a sequence of all-sky imager data that shows this southward airglow motion. The 6300 \AA airglow emission originates from altitude range of 250–300 km, which largely coincides with the altitude range of the observed slanted stripes.

There are a few other cases of turbulent plasma structures that we had observed during our July 2006 campaign at the Arecibo Observatory, as well. We are going to discuss them in detail in later chapters of this thesis. The data presentation of these turbulent plasma structures is going to include both airglow diagnostics (Chapter 3) and ISR diagnostics (Chapter 4). A short summary of radar and airglow observation that we are going to report in this thesis can be found in Table 1.1 and Table 1.2, respectively.

In addition, we are also going to present some GPS TEC data from these two nights in Chapter 5. The GPS TEC diagnostics is particularly useful for identifying TID signatures, and can be extended to provide 2-D map of ionospheric plasma disturbances [Rideout and Coster, 2006; Nicolls et al., 2004]. The results from each diagnostics are finally going to be reconciled and combined to provide a complete picture of these plasma disturbances. The combined analysis is going to be presented

Table 1.1: Arecibo ISR observation summary for our experiment on the night of 22/23 and 23/24 July 2006.

Date / Time Period	Description	ASIS Data Support [†]
NIGHT OF 22/23 JULY 2006		
22:30 LT – 23:30 LT	Slanted stripe	NO
01:30 LT – 03:30 LT	Train of turbulent filaments	YES
NIGHT OF 23/24 JULY 2006		
21:30 LT – 00:45 LT	Slanted stripes	YES
03:40 LT – 04:00 LT	Quasi-periodic echoes/filaments	YES

[†]This indicates whether any recognizable airglow structure motion was seen in the ASIS airglow data.

Table 1.2: ASIS airglow observation summary for our experiment on the night of 22/23 and 23/24 July 2006.

Date / Time Period	Description	Airglow Emission Type
NIGHT OF 22/23 JULY 2006		
20:00 LT – 05:00 LT [‡]	Ripple structure/patches	OI / 5577 Å
20:00 LT – 21:59 LT	Post-twilight enhancement	OI / 6300 Å
03:41 LT – 04:45 LT	Westward airglow motion	OI / 6300 Å
NIGHT OF 23/24 JULY 2006		
20:00 LT – 05:00 LT [‡]	Ripple structure/patches	OI / 5577 Å
20:00 LT – 22:29 LT	Post-twilight enhancement	OI / 6300 Å
20:29 LT – 21:53 LT	Northward airglow motion	OI / 6300 Å
22:31 LT – 23:31 LT	Southward airglow motion	OI / 6300 Å
02:00 LT – 03:30 LT	Westward airglow motion	OI / 6300 Å

[‡]This is essentially the whole night of airglow observation.

North American Heat Waves (July 2006 - August 2006)

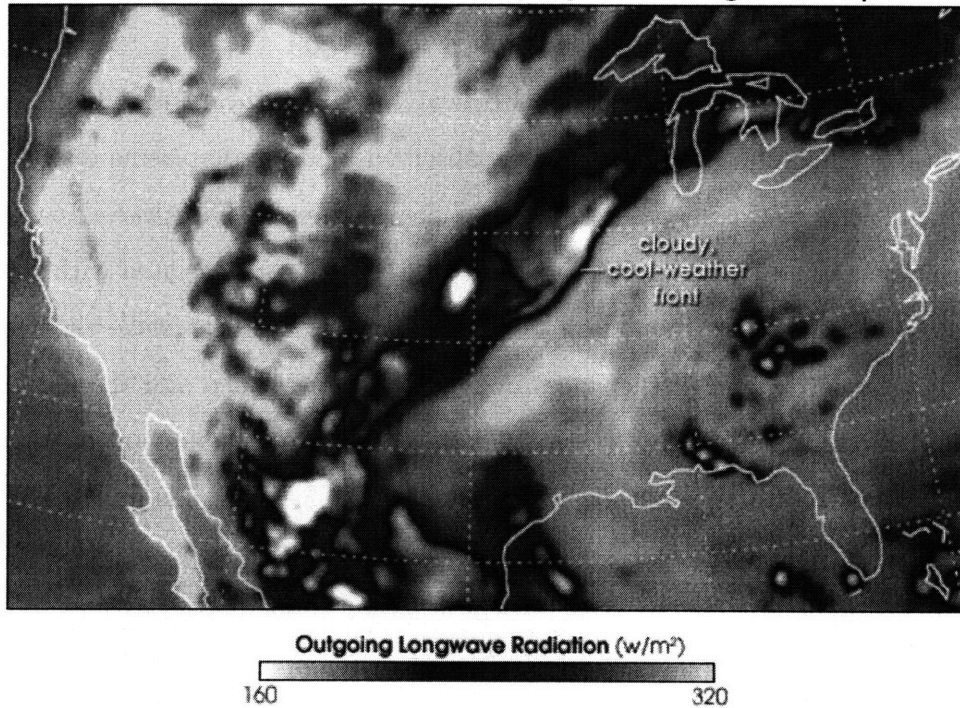


Figure 1-4: Summer 2006 North American heat waves as mapped by NASA's Clouds and the Earth's Radiant Energy System (CERES). The heat waves swept across from the Northwest toward the Southeast. Figure taken from *Atmospheric Science Data Center* [2006].

in Chapter 6 of this thesis.

1.3 Proposed Hypothesis

We strongly believe that the observed ionospheric plasma turbulence must have been caused by internal gravity waves that had reached ionospheric F region altitudes. One reason is that, as briefly discussed in the previous section, we had also observed some wavy sporadic E plasma layers during our July 2006 experiment. This observation indicates a strong perturbation in neutral atmosphere during that period of time, which is very likely to be in the form of internal gravity waves. Thus, our task has finally been narrowed down to finding the source of these gravity waves.

As also briefly mentioned before, the geomagnetic condition was generally quiet during our July 2006 Arecibo experiment. This implies that auroral activity cannot

possibly be the source of these gravity waves. Hence, we have to look for gravity wave source that is either terrestrial or meteorological in origin.

We suspect that the summer 2006 US heat wave was the responsible source of gravity waves that subsequently excite the observed ionospheric plasma disturbances over Arecibo. As it swept across the United States from the Northwest toward the Southeast, there had been reports on severe weather events associated with the heat wave. It is thus possible that upon leaving the shore, the heat wave then further seeded more atmospheric disturbances over the Gulf of Mexico and the Caribbean. Figure 1-4 shows the summer 2006 US heat wave, based on the amount of long wave radiation from the Earth's surface, as mapped by NASA's Clouds and the Earth's Radiant Energy System (CERES) [ASDC, 2006].

It should be noted that no other nearby weather anomalies could have been responsible for the observed ionospheric plasma disturbances. First of all, there was no close encounter of hurricanes near Puerto Rico around the time of our observation. Furthermore, there was no other major catastrophic weather event such as volcano eruptions, earthquakes, or tsunamis—which had been known as powerful source of strong gravity waves in the Earth's atmosphere. The absence of such “conventional” gravity wave sources leads us to focus our attention to the summer 2006 US heat wave, which was the most relevant weather anomaly in terms of its timing and location. Detailed discussion on the search of the responsible gravity wave source is presented in Chapter 6 of this thesis.

The above speculation has the implication that global warming-related events might have real and significant effects on space plasmas, even though this type of plasmas are located very far away from the Earth's surface. This certainly warrant further investigation and scrutiny. An outline of planned future work to further investigate this phenomenon is given in Chapter 7 along with the conclusion of the current work.

Chapter 2

Ionospheric Disturbances: An Overview

This chapter is going to provide some background information on gravity waves and the related ionospheric plasma disturbances. This is particularly relevant for our current study of ionospheric plasma turbulence in the mid-latitude regions, because gravity waves are often the cause of plasma turbulence there.

Gravity waves are important in mid-latitude ionospheric studies for the following reason. Unlike in polar or equatorial regions, magnetic field configuration in mid-latitudes is not conducive to the Rayleigh-Taylor instability and auroral current usually does not reach that far except during severe substorms. Thus, other types of source mechanism usually drive plasma turbulence in mid-latitudes. When there exist some disturbances in the neutral atmosphere, internal gravity waves could provide coupling between neutral atmosphere and the ionosphere. By carrying energy away from lower atmosphere and dissipate it in the ionosphere, gravity waves would subsequently trigger plasma turbulence [Lastovicka, 2006].

2.1 Internal Gravity Waves

Gravity waves are disturbances in the atmosphere that usually appear as neutral wind fluctuations. The magnitude of these wind fluctuations might not be very

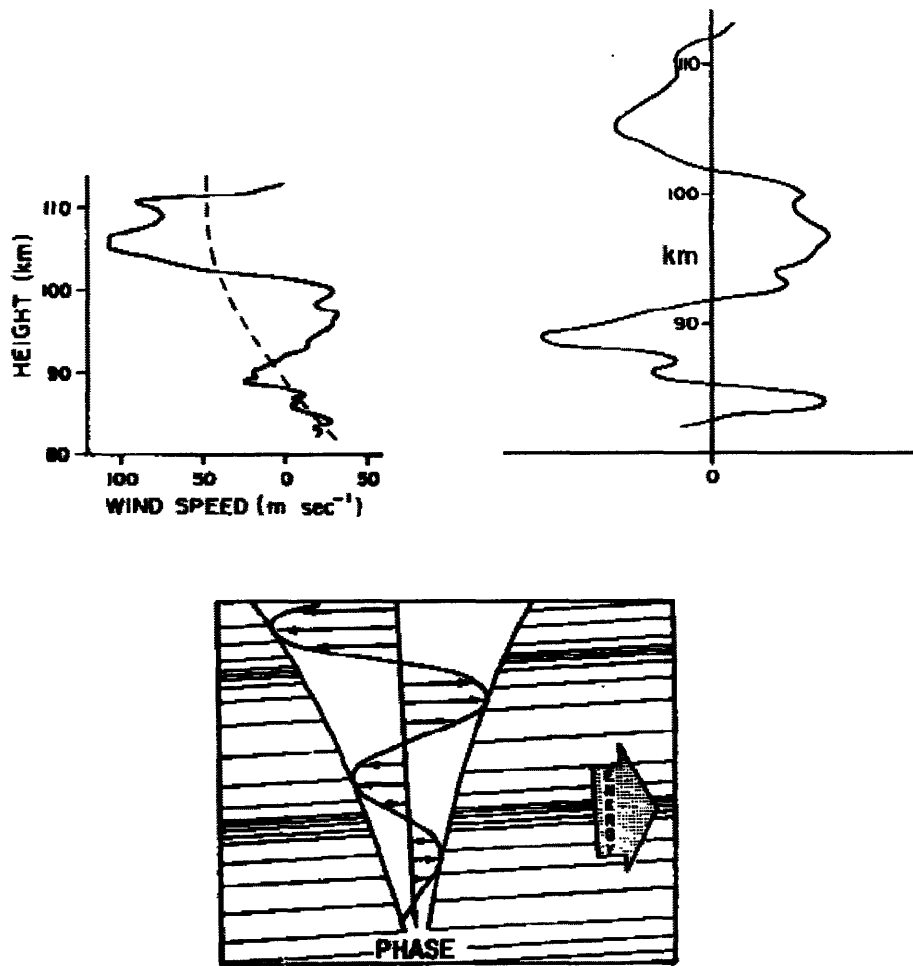


Figure 2-1: Neutral wind speed fluctuations associated with internal gravity waves at meteor heights (upper left & upper right). A pictorial illustration of internal gravity wave amplitude growth and its phase/energy propagation (bottom). After *Hines* [1960].

significant near the ground, but they could be far more noticeable when they had reached the upper atmosphere. The two upper graphs in Figure 2-1 show an example of horizontal neutral wind speed fluctuation at meteor heights due to internal gravity waves. It should be noted that even in the absence of gravity waves, a background wind velocity profile/shear could still exist in the upper atmosphere (shown as dashed lines in the upper left graph of Figure 2-1). Thus, background wind profile and the wind fluctuations due to gravity waves will typically be superposed on top of each other. The upper right graph in Figure 2-1 shows the net wind fluctuations associated with the gravity waves, without the background wind profile contribution.

Roughly speaking, atmospheric gravity waves can be divided into two categories: (1) internal gravity waves and (2) surface waves. The difference between the two lies in their capability of having vertical propagation [Hines, 1960; Yeh and Liu, 1972]. Internal gravity waves could support a substantial vertical propagation, while surface waves are evanescent along vertical direction. Internal gravity waves are the ones of interest to us because we will be dealing with coupling processes between neutral atmosphere and the ionosphere. We shall next look into some defining features of internal gravity waves.

There are several important features of internal gravity waves [Hines, 1960; Nappo, 2002]. First of all, internal gravity waves need to have wave periods larger than a certain characteristic value given by $\tau_g \equiv \frac{2\pi c_s}{g\sqrt{\gamma-1}}$. Otherwise, the internal wave will become evanescent. Here c_s denotes the speed of sound; g is the gravitational acceleration; and γ is the ratio of specific heats. Furthermore, the amplitude of internal gravity waves tends to increase ($\propto \exp[\frac{\gamma g z}{2c_s^2}]$) as they propagate upwards because atmospheric density generally decreases with altitudes. This is a direct consequence of energy flux conservation during gravity wave passage in the atmosphere. Another interesting feature of internal gravity wave is that the direction of phase propagation is nearly perpendicular to the direction of energy propagation (i.e., phase velocity is \sim perpendicular to group velocity). Some of these features are illustrated in the bottom graph of Figure 2-1: The growth of gravity wave oscillation amplitudes can be seen from the enveloped arrows of wind velocity vectors. In the case shown here, the energy propagation is obliquely upwards and the phase propagation is almost vertically downward.

A dispersion relation that describes internal gravity waves has been derived by Hines [1960], and it is given by (assuming an isothermal atmosphere):

$$\omega^4 - \omega^2 c_s^2 (k_x^2 + k_z^2) + (\gamma - 1) g^2 k_x^2 - \frac{\gamma^2 g^2 \omega^2}{4c_s^2} = 0 \quad (2.1)$$

where c_s is the sound speed; g is the gravitational acceleration; γ is the ratio of specific heats; ω is the wave frequency; and k_x (k_z) denotes the horizontal (verti-

cal) wavenumber, respectively. The roots of the above quartic equation in ω divide this wave mode into two regimes: a high-frequency branch and a low-frequency branch. The high-frequency branch has wave frequencies $\omega > \omega_a \equiv \gamma g/2c_s$, and is termed acoustic waves. Meanwhile, the low-frequency branch has wave frequencies $\omega < \omega_b \equiv \sqrt{\gamma - 1} g/c_s$, and it is *the* internal gravity waves. For any intermediate frequencies $\omega_b < \omega < \omega_a$, no internal gravity wave modes are allowed. The characteristic frequency ω_b is known as the Brunt-Vaisala frequency, which is the natural frequency for air parcels in the atmosphere to oscillate up and down due to buoyancy [Kelley, 1989; Yeh and Liu, 1972].

The dissipation of internal gravity waves primarily depends on two atmospheric properties: viscosity and thermal conductivity [Hines, 1960; Yeh and Liu, 1972]. Dissipation generally becomes important at greater heights, such as in the upper atmosphere or the ionosphere. This is where internal gravity waves finally break apart and dissipate energy after growing in amplitudes. Furthermore, the dissipation turned out to be more severe for internal gravity waves with smaller scale/wavelength. In other words, internal gravity waves with smaller scale/wavelength would be dissipated at lower altitudes compared to larger-scale gravity waves.

2.2 Sporadic-E Plasma Layer and Kelvin-Helmholtz Instability

Sporadic E layers are thin, patchy, yet dense plasma layers in the ionospheric E region at around 100–120 km altitudes. In the mid-latitudes, sporadic E layers are formed by neutral wind shear in the upper atmosphere. Typically, zonal (east-west) wind shear is more effective in creating sporadic E layers compared to meridional (north-south) wind shear [Kelley, 1989]. The wind shear itself might be due to internal gravity waves, which makes the presence of sporadic E layers an indication of gravity wave occurrences. Furthermore, if the wind shear is strong enough, plasma structures/irregularities could subsequently develop in the sporadic E layer [Bern-

hardt, 2002]. This is likely due to a type of magnetohydrodynamic (MHD) instability known as the Kelvin-Helmholtz instability.

We will now discuss the wind shear mechanism for sporadic E layer formation. We begin the analysis by writing down the ion momentum equation (for a particular ion species j):

$$\rho_j \left(\frac{\partial \vec{v}_j}{\partial t} + (\vec{v}_j \cdot \nabla) \vec{v}_j \right) = -\nabla p + \rho_j \vec{g} + n_j q_j (\vec{E} + \vec{v}_j \times \vec{B}) - \sum_k \rho_j \nu_{jk} (\vec{v}_j - \vec{v}_k) \quad (2.2)$$

where ρ_j denotes the ion mass density, p is the pressure, \vec{g} is the gravitational acceleration vector, n_j is the ion number density, q_j is the ionic charge, \vec{E} is the electric field, \vec{B} is the magnetic field, and ν_{jk} is the collision frequency between species j and k . Assuming steady-state condition, we can set the LHS of Equation 2.2 to be zero. Furthermore, we will only consider collisions with neutral particles (i.e., the index k will represent the neutral particles). We will also ignore pressure gradient, gravity, and any electric field. We then have:

$$\begin{aligned} \mathcal{O} &= \mathcal{O} + n_i e (\mathcal{O} + \vec{v}_i \times \vec{B}) - \rho_i \nu_{in} (\vec{v}_i - \vec{U}_n) \\ \rho_i \nu_{in} (\vec{v}_i - \vec{U}_n) &= n_i e (\vec{v}_i \times \vec{B}) \end{aligned} \quad (2.3)$$

where \vec{U}_n represent the background neutral wind velocity, and we have assumed singly-ionized ions. The background magnetic field is assumed to be constant and uniform everywhere. Meanwhile, the neutral wind velocity is chosen to be flowing perpendicularly to the magnetic field lines, and have no time dependence.

We will adopt a coordinate system where the magnetic field is pointing in the \hat{z} direction, and the background neutral wind is flowing along the \hat{x} direction. Then the vector quantities can be written explicitly as $\vec{U}_n = [U_n, 0, 0]$; $\vec{B} = [0, 0, B]$; and $\vec{v}_i = [v_{ix}, v_{iy}, v_{iz}]$. Let us define $\kappa \equiv eB/M_i \nu_{in}$ where M_i is the ion mass. Also recall that $\rho_i = M_i n_i$. After performing the explicit vector operations and using the above

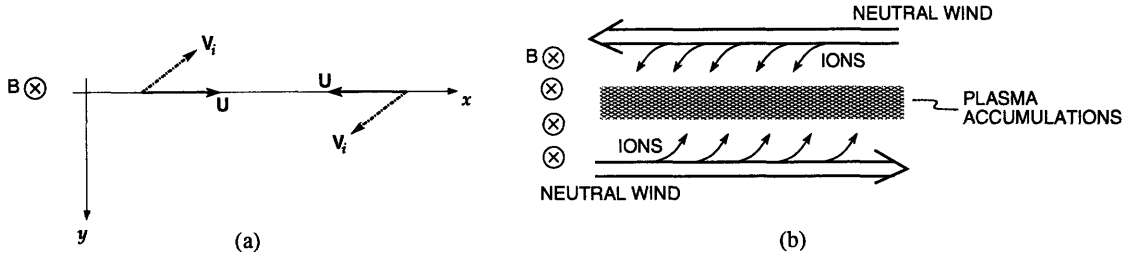


Figure 2-2: (a) A diagram showing the direction of ion motion under the influence of neutral wind in a collisional magnetized plasma. (b) Schematic illustration of the wind shear mechanism for sporadic E layer formation. Adapted from *Kelley* [1989].

definition, we will obtain:

$$\kappa[v_{iy}, -v_{ix}, 0] = [v_{ix} - U_n, v_{iy}, v_{iz}] \quad (2.4)$$

which forms a system of equations for v_{ix} , v_{iy} , and v_{iz} . Solving these coupled equations, we will have:

$$v_{ix} = \frac{U_n}{1 + \kappa^2} ; \quad v_{iy} = -\frac{\kappa U_n}{1 + \kappa^2} ; \quad v_{iz} = 0 \quad (2.5)$$

for the ion velocity components. The results given in Equation 2.5 thus give a general idea on how the ions will move as a response to a constant background neutral wind in a collisional magnetized plasma.

Figure 2-2(a) give a graphical illustration of the resulting ion motion as described by Equation 2.5. As shown in this figure, the ions will be dragged by the neutral wind, but because of the magnetic Lorentz force, the ion motion will be deflected sideways from the original neutral wind direction. For opposite neutral wind directions, the direction of the resulting ion motion will be reversed as well. Now consider a case where neutral wind at two different altitudes are in opposite directions (an example of wind shear) as depicted in Figure 2-2(b). In the configuration shown here, ions from higher altitudes will be deflected downwards and vice versa. As a consequence, the ions will be accumulated at the center—in between these sheared streams. The electrons will subsequently follow the ions to accumulate there, thus maintaining the overall charge neutrality. This is the wind shear mechanism for the formation of

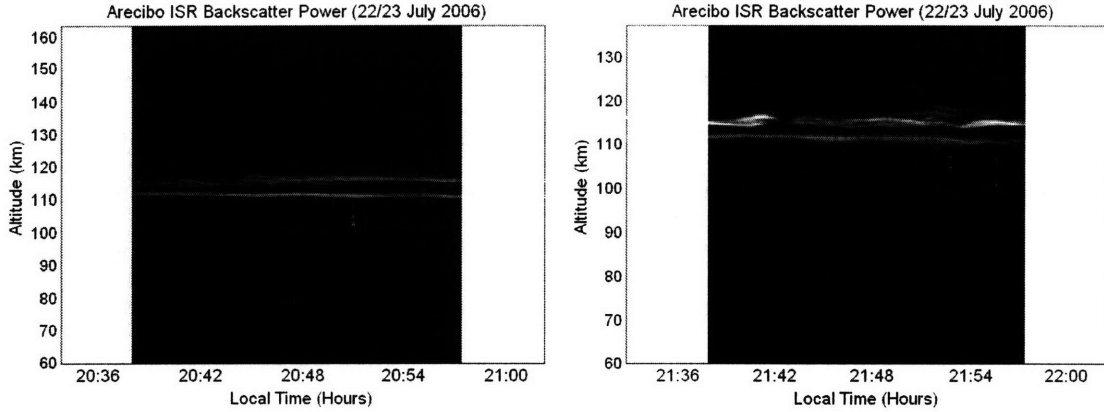


Figure 2-3: Examples of Kelvin-Helmholtz billows that could develop in the sporadic E plasma layer due to a strong wind shear.

sporadic E plasma layers in mid-latitude regions [*Kelley, 1989*].

If we have a sufficiently strong wind shear, some wave structures might also develop in the sporadic E layers due to Kelvin-Helmholtz instability. This instability is driven by velocity shear and it could develop in neutral fluids as well as in plasmas.

An analysis of Kelvin-Helmholtz instability in plasmas using incompressible ideal MHD equations had been discussed by *Siscoe [1983]*. The analysis considered two plasma regions that are separated by a tangential discontinuity in fluid velocity, density, and magnetic field. Wave fluctuations in the boundary/interface could grow via Kelvin-Helmholtz instability if a threshold condition is satisfied:

$$(\Delta\vec{v} \cdot \vec{k})^2 > \frac{1}{\mu_0} \left(\frac{1}{\rho_1} + \frac{1}{\rho_2} \right) \left[(\vec{B}_1 \cdot \vec{k})^2 + (\vec{B}_2 \cdot \vec{k})^2 \right] \quad (2.6)$$

where $\Delta\vec{v}$ is the difference in plasma fluid velocity across the interface; \vec{k} denotes the wavevector of the fluctuations; ρ_1 (ρ_2) denotes the mass density in region 1 (region 2); and \vec{B}_1 (\vec{B}_2) denotes the magnetic field in region 1 (region 2), respectively. Once the instability is excited and eventually saturates, there would be a dominant wavenumber that determine the characteristic wavelength of the fully-developed Kelvin-Helmholtz modes. During experiments, we would typically see this characteristic wavelength only.

Figure 2-3 shows some examples of wavy and intense sporadic E layers that we

observed during the July 2006 experimental campaign at the Arecibo Observatory. Wavelike fluctuations in those plasma layers are presumably Kelvin-Helmholtz modes that were driven by a strong wind shear. The neutral wind fluctuations causing the shear might have been associated with internal gravity waves. Thus, the existence of wavy and intense sporadic E layers on that night was probably an early indication of strong internal gravity waves entering the ionosphere from the lower atmosphere.

2.3 Ionospheric Disturbances Induced by Gravity Waves

In addition to neutral wind fluctuations, there are also neutral density and pressure fluctuations associated with internal gravity waves. Due to interactions between plasma and neutral particles, some plasma density fluctuations in the ionosphere could be generated as gravity waves propagate through. The induced plasma fluctuations are usually referred to as traveling ionospheric disturbances (TID). It should be noted, however, that wavefronts of the induced TID might not necessarily coincide with wavefronts of the gravity waves. The movement of TID might also be different from the propagation direction of the inertial gravity waves. This is because charged particle motions are restricted by the Earth's magnetic field while neutral particles are not. Since TIDs are plasma disturbances, their movement will generally follow $\vec{E} \times \vec{B}$ drift.

Fluctuations in neutral particle density and pressure could significantly affect ion production rate and plasma recombination rate in the ionosphere. This is the main reason for the formation of plasma density perturbations in the ionosphere during the passage of internal gravity waves. An early theoretical foundation for this process was carried out by *Hooke* [1968]. This basic model for the gravity wave-induced TIDs had implemented the above ideas on how neutral density perturbation affects ion production and recombination.

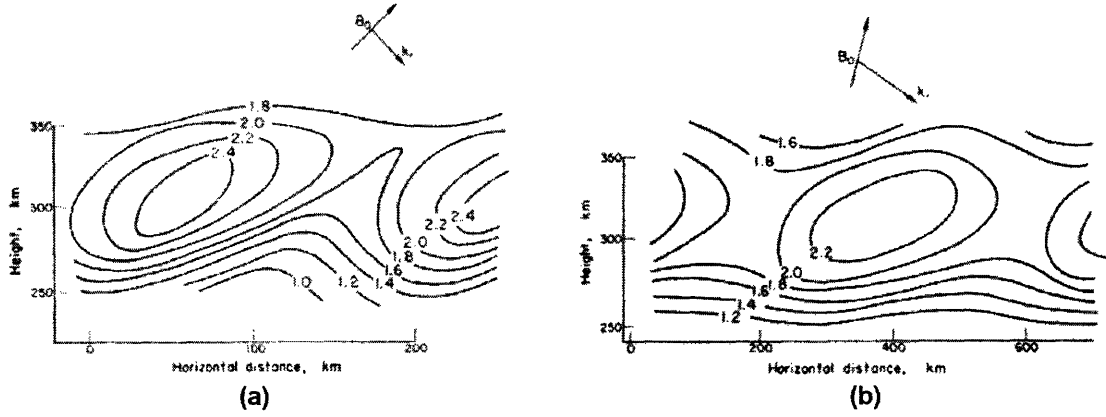


Figure 2-4: Sample contour plots that describe the induced plasma density fluctuations during the passage of internal gravity waves in the ionosphere for two different orientations of wavevector relative to the magnetic field. Taken from *Hooke* [1968].

The expression for the induced electron plasma density fluctuation as calculated by *Hooke* [1968] is given by:

$$\delta N_e(x, y, z, t) = N_{e0}(z) U_b(z_0) \sin I \exp[k_{z,Im}(z - z_0)] \frac{1}{\omega} \sqrt{\left(\frac{1}{N_{e0}} \frac{\partial N_{e0}}{\partial z}\right)^2 + \left(\frac{k_{b,Re}}{\sin I}\right)^2} \times \exp \left[i \left(\omega t - k_x x - k_y y - k_{z,Re} z + \frac{\pi}{2} - \tan^{-1} \left[\frac{k_{b,Re}}{\sin I \left(\frac{1}{N_{e0}} \frac{\partial N_{e0}}{\partial z} + k_{z,Im} \right)} \right] \right) \right] \quad (2.7)$$

where z_0 is an arbitrary reference height; U_b is the amplitude of wind fluctuations along the magnetic field; I is the magnetic dip angle; $k_b \equiv \vec{k} \cdot \hat{B}$ is the projection of gravity wave wavevector along the magnetic field; and subscripts *Re* (*Im*) indicates the real (imaginary) part, respectively. Figure 2-4 shows two examples of the calculated plasma density perturbations based on this model. Both cases describe the situation for mid-latitude regions where the neutral wind fluctuations is in the order of ~ 100 m/s. Figure 2-4(a) is the case where the wavevector is exactly perpendicular to the magnetic field lines, whereas Figure 2-4(b) is the not-exactly-perpendicular case.

As one can see, the resulting plasma density perturbations might not be exactly aligned with the gravity wave wavefronts. Nonetheless, if the overall phase progression of gravity waves had a downward component then typically so did the plasma density

striations. The TID configuration therefore would mimic the phase progression of inertial gravity waves to some extent. Hence, judging from their configuration, TIDs with geometry of slanted plasma sheets/stripes are probably the ones triggered by inertial gravity waves from neutral atmosphere.

Chapter 3

Airglow Diagnostics

Presented in this chapter are the results of airglow measurement using MIT All-Sky Imaging System (ASIS) performed on the night of 22/23 and 23/24 July 2006 at Arecibo Observatory, Puerto Rico. There was no (or very few) clouds on these two nights, thus giving us an opportunity to utilize airglow diagnostics using an all-sky imager to its fullest potential. This chapter is going to begin with a brief overview of using airglow measurement to diagnose ionospheric plasma turbulence, followed with a thorough data presentation from the two nights of successful airglow measurements.

3.1 Ionospheric Plasma Diagnostics Through Airglow Measurement

Lights that are emitted by atoms/molecules from the Earth's atmosphere can in principle be observed, and they are known as *airglows*. Although airglow is difficult to observe during the daytime, the nighttime airglow can be observed much more easily and we can obtain a good diagnostics on ionospheric plasma turbulence by looking at airglow structures using an all-sky imager. Airglow measurement using an all-sky imager has a great advantage due to its capability to map the turbulent ionospheric structures in 2-D, giving us a clear picture of the situation.

Airglow emission lines originated from energy level transitions of bound electrons

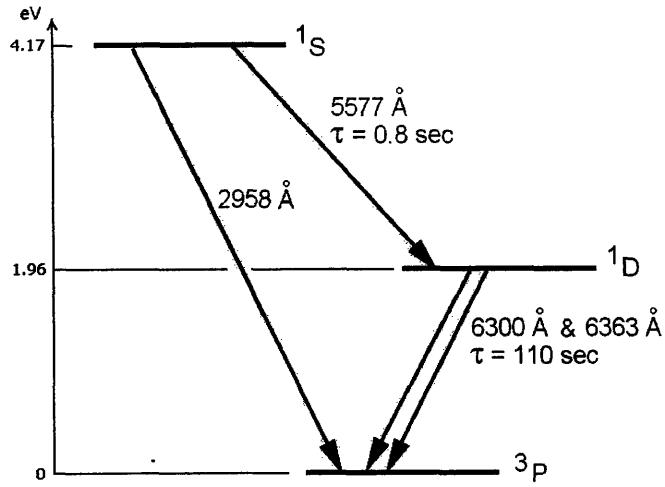


Figure 3-1: A portion of energy level diagram for atomic oxygen showing specific transitions that give rise to the 5577 Å and 6300 Å OI emission, which is commonly used for airglow diagnostics of ionospheric plasmas. Adapted from *Carlson and Egeland [1995]*.

inside atoms/molecules. Thus, specific emission lines usually characterize specific regions of the ionosphere where the population density of a particular atomic/molecular species is dominant, and where a particular energy level transition occurs at a significantly fast rate. The two commonly used emission lines for diagnosing ionospheric plasma are the 5577 Å (green) and 6300 Å (red) OI (neutral atomic oxygen) emission. The 5577 Å OI emission mainly originated from ~90 km altitude, around the ionospheric E-region, whereas the 6300 Å OI emission comes from the ionospheric F-region (around 250-300 km altitude). Figure 3-1 illustrates the specific energy level transitions inside neutral atomic oxygen that give rise to the 5577 Å and 6300 Å OI emission.

The 6300 Å emission is mainly caused by a chain of chemical reactions in the ionospheric F-region, started with molecular ion formation through [*Chamberlain, 1961*]



and followed by dissociative recombination process



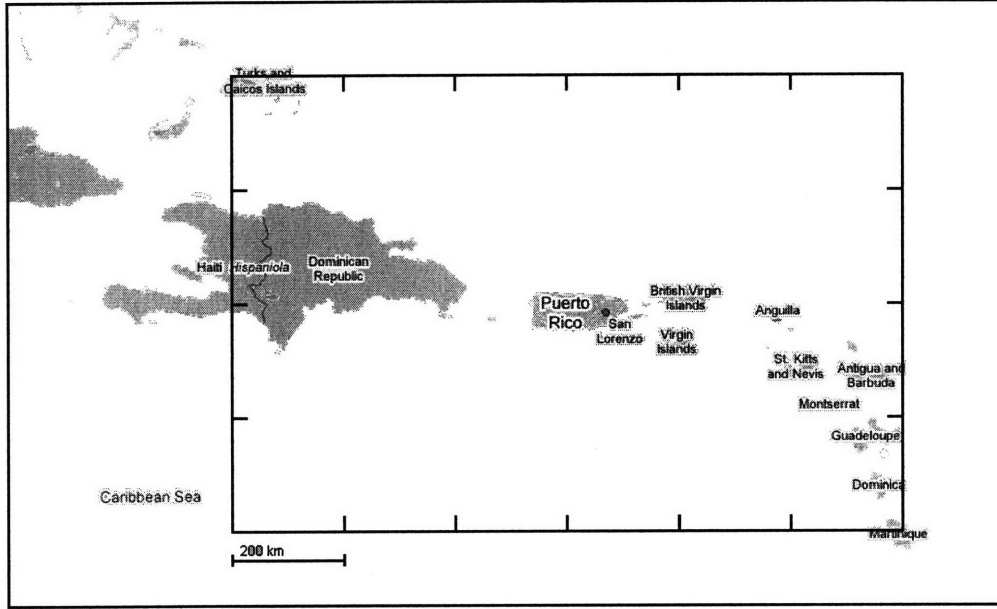


Figure 3-2: A map of Puerto Rico and the surrounding islands in the Caribbean area. The $1200 \text{ km} \times 800 \text{ km}$ frame represents the coverage area of 6300 \AA airglow measurement using ASIS at Arecibo Observatory.

where O^* indicates neutral atomic oxygen in its excited state. The excited O^* then relaxes to a lower energy state, emitting the 6300 \AA photon. Alternatively, the molecular ion formation can also occur in a different way [Chamberlain, 1961]:



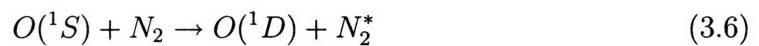
which is then followed by the following dissociative recombination:



Meanwhile, the origin of 5577 \AA OI emission is the reaction [Chamberlain, 1961]



and it is suppressed by collisional de-excitation through the reaction



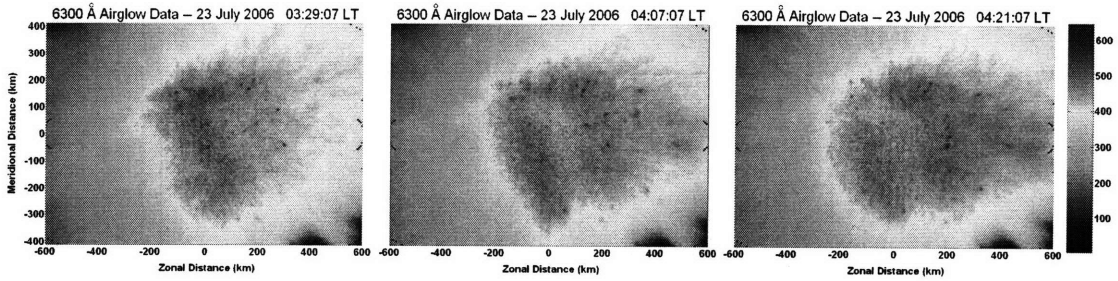


Figure 3-3: Three airglow intensity maps from the night of 22/23 July 2006 which were recorded at 03:29:07 LT, 04:07:07 LT, and 04:21:07 LT. These airglow structures had an approximately westward direction of motion during this time period.

where N_2^* is left in a vibrational excited state.

In this thesis, we will be focusing on the 6300 Å airglow emission for the diagnostics of ionospheric F-region plasma turbulence. Figure 3-2 schematically shows the geographical area that is covered by the all-sky imager’s field of view for the 6300 Å airglow measurement. All airglow intensity maps presented in this chapter have been transformed into geographic coordinates with linear distances (kilometers) along zonal and meridional directions. The detailed description of coordinate transformation from an all-sky image into a geographic airglow map can be found in Appendix A of this thesis.

3.2 All-Sky Airglow Measurement on The Night of 22/23 July 2006

During the night of 22/23 July 2006, the sky was overall clear even though there were a few cloud patches right after sunset and shortly before sunrise. On this night, an overall westward motion of airglow was observed during time period 03:41 LT – 04:45 LT. Figure 3-3 shows three sequential airglow intensity maps recorded by ASIS at 03:29:07 LT, 04:07:07 LT, and 04:21:07 LT which illustrate this westward motion.

A further analysis to track the motion of the observed airglow structures was also performed to determine its actual speed and direction of motion. The detailed procedures for the airglow structure tracking can be found in Appendix B of this

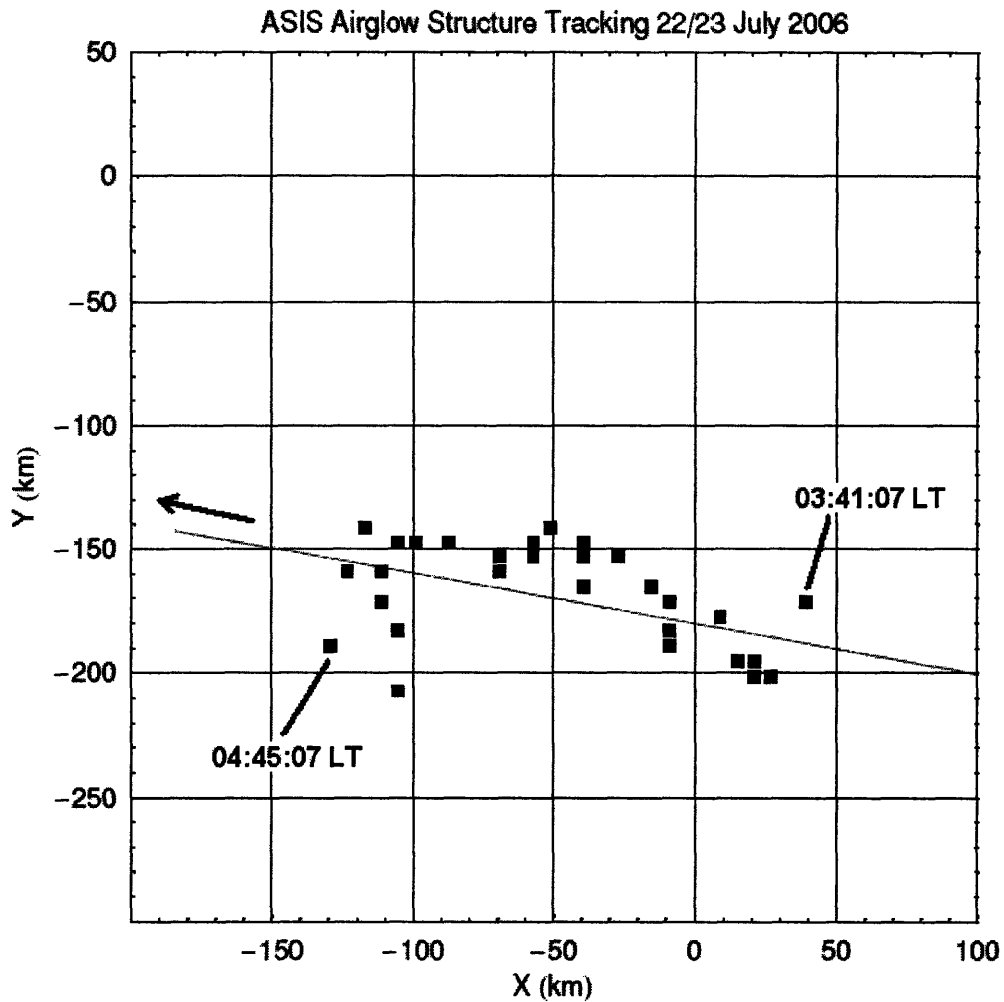


Figure 3-4: Airglow structure tracking analysis for the ~westward moving airglow on the night of 22/23 July 2006. The airglow speed was calculated to be 46.3 ± 2 m/s.

thesis. Figure 3-4 shows the result of this analysis. The fitted straight-line trajectory tells us that the airglow motion was toward the 281.3° direction (11.3° north of west). The airglow structures started to spread apart toward north and south as it progressed westward, thus causing more uncertainty in the exact direction of airglow. Nonetheless, a result of overall ~westward direction was established from this analysis. The speed of this airglow motion was determined to be approximately 46.3 m/s, with an uncertainty of ~ 2 m/s.

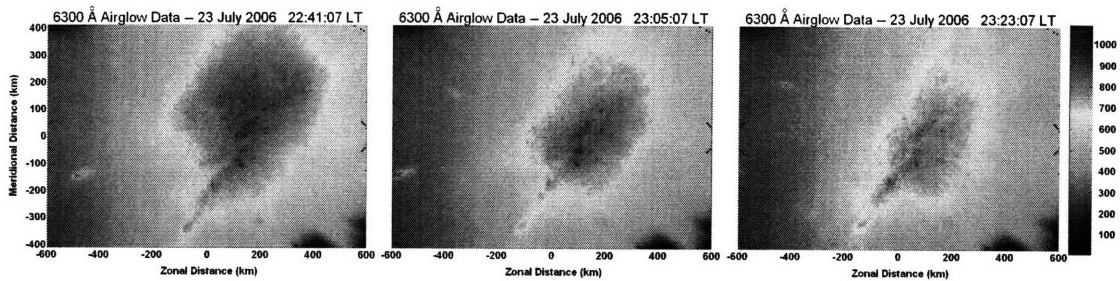


Figure 3-5: Three airglow intensity maps from the night of 23/24 July 2006 which were recorded at 22:41:07 LT, 23:05:07 LT, and 23:23:07 LT. These airglow structures had an approximately southward direction of motion during this time period.

3.3 All-Sky Airglow Measurement on The Night of 23/24 July 2006

During the night of 23/24 July 2006, a richer airglow motion pattern was observed. The sky condition was also much better than the night before, with absolutely no cloud patches interrupting our observations. Presented in this section are the analysis of two different airglow structures that were observed at two distinct period of time. Earlier that night, a southward airglow motion was observed; whereas later that night, a westward airglow motion was observed.

3.3.1 Observation of a Southward Airglow Motion

During the night of 23/24 July 2006, a \sim southward motion of airglow was observed during time period 22:31 LT – 23:31 LT. Figure 3-5 shows three sequential airglow intensity maps recorded by ASIS at 22:41:07 LT, 23:05:07 LT, and 23:23:07 LT which illustrate this southward motion.

A further analysis to track the motion of the observed airglow structures was again performed to determine its actual speed and direction of motion. Figure 3-6 shows the result of this airglow tracking procedures. From the fitted straight-line trajectory, we found that the airglow motion was toward the 170.1° direction (9.9° east of south). The airglow motion was quite firm, so that only a relatively small uncertainty of $\sim 0.45^\circ$ was affecting the result for the direction of motion. The speed of this southward

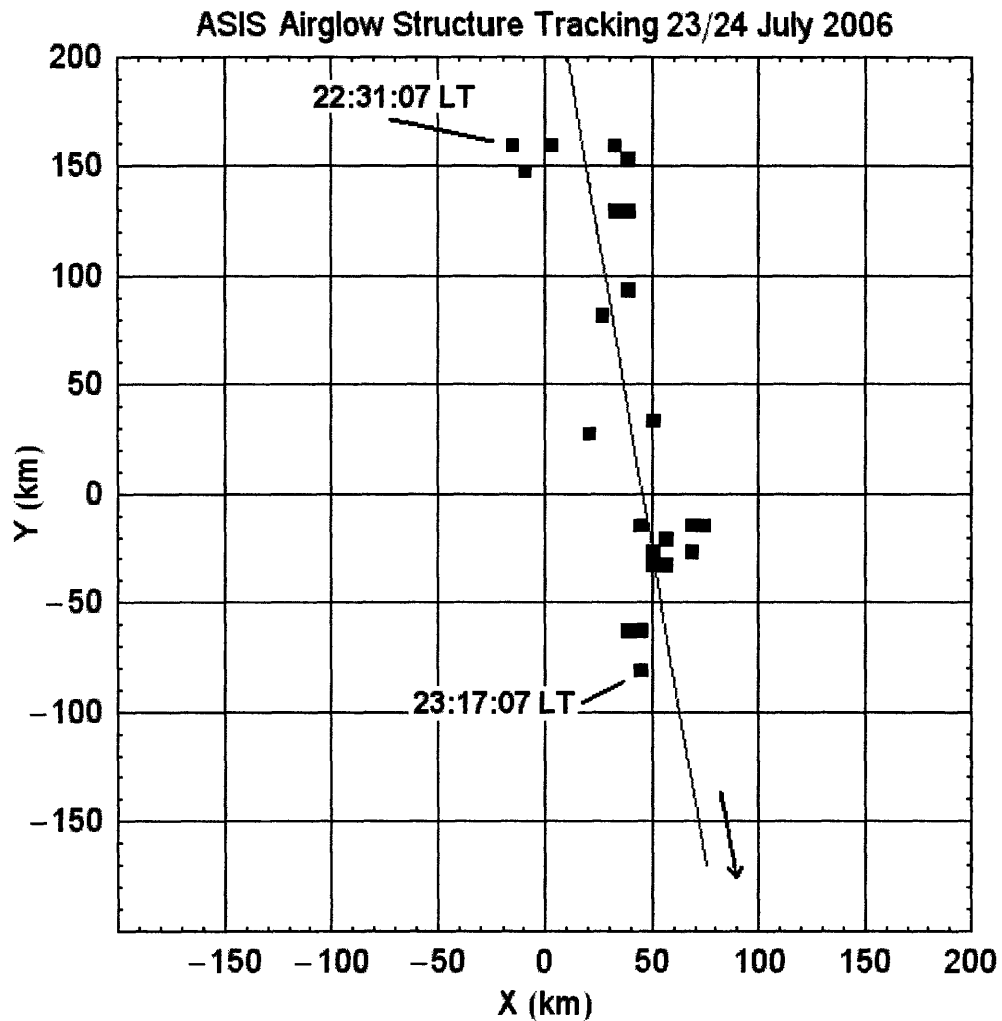


Figure 3-6: Airglow structure tracking analysis for the ~southward moving airglow on the night of 23/24 July 2006. The airglow speed was calculated to be 97.3 ± 7 m/s.

airglow motion was determined to be approximately 97.7 m/s, with an uncertainty of ~ 7 m/s. This value of airglow motion speed is the largest one of all three airglow structure motion analysis that are discussed in this thesis. In fact, this southward airglow motion coincides with the observation of a train of slanted stripes/ parallel plate structures on the Arecibo ISR backscatter power profile.

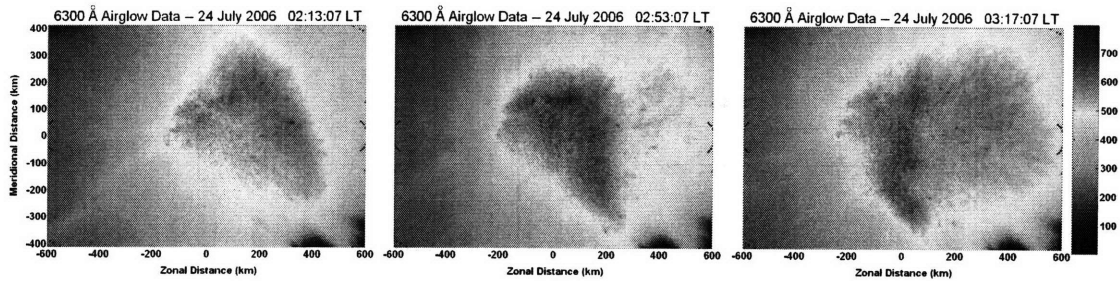


Figure 3-7: Three airglow intensity maps from the night of 23/24 July 2006 which were recorded at 02:13:07 LT, 02:53:07 LT, and 03:17:07 LT. These airglow structures had an approximately westward direction of motion during this time period.

3.3.2 Observation of a Westward Airglow Motion

During the night of 23/24 July 2006, a \sim westward motion of airglow was observed during time period 02:00 LT – 03:30 LT. Figure 3-7 shows three sequential airglow intensity maps recorded by ASIS at 02:13:07 LT, 02:53:07 LT, and 03:17:07 LT which illustrate this westward motion.

The airglow structure tracking analysis was also performed for this period of time to determine the airglow’s actual speed and direction of motion. Figure 3-8 shows the result of the airglow tracking procedures. From the fitted straight-line trajectory, we found that the airglow motion was toward the 256.5° direction (13.5° south of west). The tracking procedures did not work too well for this set of data, and a large uncertainty of $\sim 11^\circ$ is affecting this result. From linear regression of the data points, the speed of this westward airglow motion was determined to be approximately 67.3 m/s, with an uncertainty of ~ 5 m/s. This westward-moving airglow coincides with the observation of some filament structures/ quasi-periodic echoes from the ionospheric F-region as shown in the Arecibo ISR backscatter power profile data.

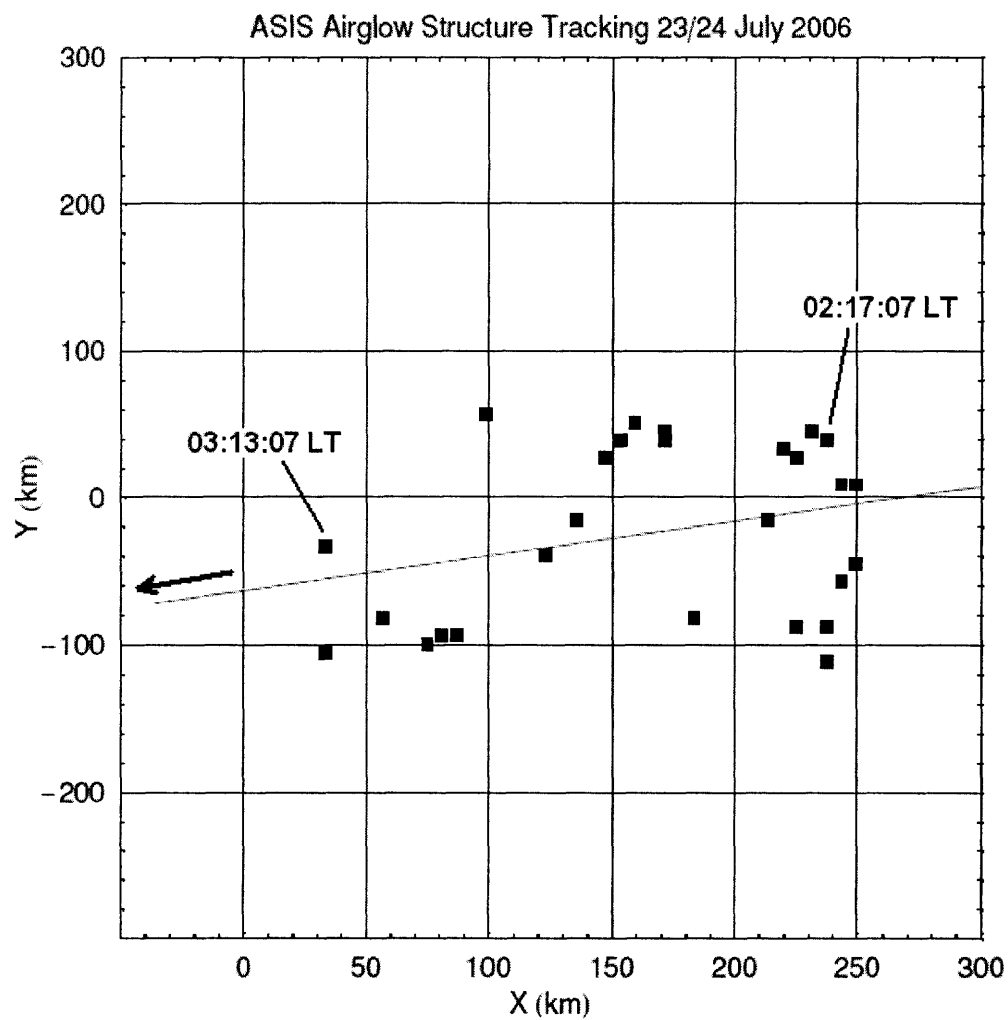


Figure 3-8: Airglow structure tracking analysis for the ~westward moving airglow on the night of 23/24 July 2006. The airglow speed was calculated to be 67.3 ± 5 m/s.

Chapter 4

Incoherent Scatter Radar Diagnostics

This chapter will be dealing with ionospheric plasma diagnostics using incoherent scatter radar (ISR) that had been used at the Arecibo Observatory, Puerto Rico. We will begin with a brief overview regarding the basics of this diagnostics. Then, we are going to discuss the result of our ISR observation at the Arecibo Observatory on the night of 22/23 July 2006 and 23/24 July 2006 when turbulent plasma structures in the form of slanted stripes/parallel plates and filaments were observed.

4.1 Overview of ISR Measurement Basics

In diagnosing ionospheric plasmas, an incoherent scatter radar (ISR) relies primarily on the scattering of radio waves by plasma density fluctuations that are associated with ion-acoustic and Langmuir waves. In laboratory/ fusion plasmas, this type of diagnostics is usually referred to as the *collective Thomson scattering* diagnostics. Nonetheless, the terminology *incoherent scatter* is retained in space plasma community for various reasons.

The frequency spectrum of typical backscattered radar signals is schematically shown in Figure 4-1. Portion of the backscattered signals due to ion-acoustic waves is called the *ion line*, and it shows up as the double-humped part of the spectrum

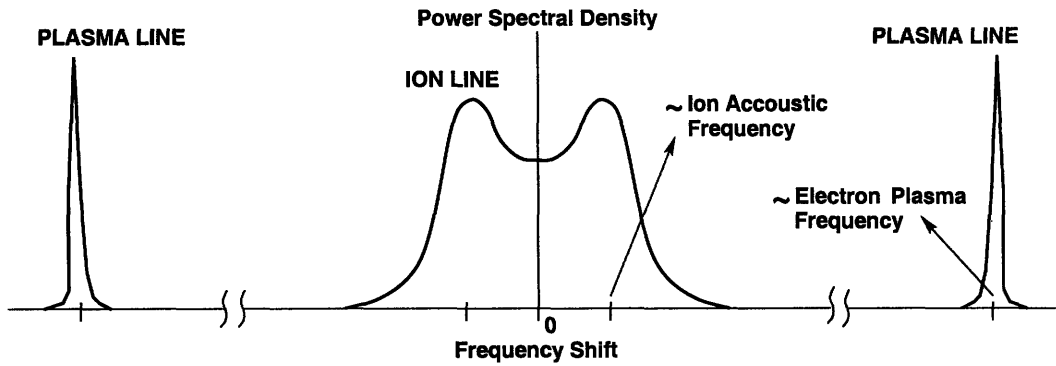


Figure 4-1: A schematic illustration of incoherent scatter frequency spectrum.

(Doppler spreading due to thermal motion of ions). Meanwhile, the other portion due to Langmuir waves is called the *plasma line*, and it will show up as a sharper peak at around the electron plasma frequency. The right hand part of the graph (positive Doppler frequency shift) corresponds to scattering by electrostatic waves that propagate downward (towards the radar), and the left hand part of the graph is due to the upgoing electrostatic waves. Most of the backscattered power comes within the ion line spectrum, and a much smaller amount of power is contained in the plasma line spectrum [Dougherty and Farley, 1960; Farley, Dougherty and Barron, 1961; Bauer, 1975].

For determining ionospheric plasma density profile, one will only need the ion line portion of the incoherent scatter spectrum (since most of the backscattered power is contained there). This type of ISR operation is known as *backscatter power* measurement. The required radar receiver bandwidth for backscatter power measurement is fairly small because the width of the ion line itself is only a few ion-acoustic frequencies. The signal-to-noise ratio in the ion line signals is also quite high, so we only need a relatively short integration time for backscatter power measurement. The Arecibo 430 MHz ISR typically requires ~ 10 seconds integration time for each backscatter power profile.

Shown in the left part of Figure 4-2 is a sample backscatter power measurement using Arecibo ISR on the night of 22/23 July 2006. Note that the received radar power will fall as the square of altitude/range, so that a range-squared correction will

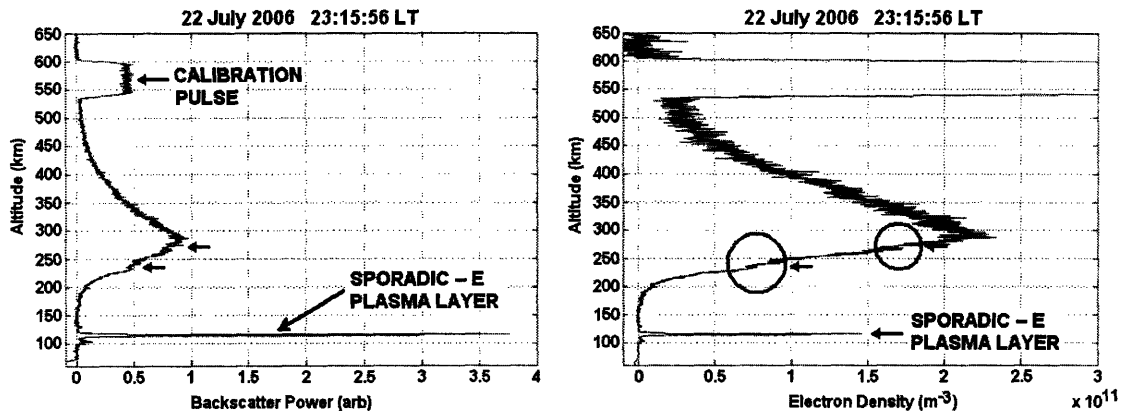


Figure 4-2: A sample ISR backscatter power profile together with the derived ionospheric plasma density profile. Signatures of plasma structures can be seen as dips/depletions (marked by the red arrows) in both backscatter power and plasma density profile. Note that the signatures can be seen better in the backscatter power profile.

be needed if we want to convert this backscatter power profile into a plasma density profile. Together with ionosonde measurements of peak plasma frequency and some appropriate linear scalings, we can obtain the corresponding plasma density profile which is shown in the right part of Figure 4-2.

The ISR backscatter power data shown in Figure 4-2 were recorded when parallel plate plasma structure was moving across the radar beam. The signatures of this plasma structure appeared in both backscatter power and plasma density profile as dips/depletions. However, these signatures can be seen better in the backscatter power profile plot. Thus, the ISR data presentation of the observed plasma structures in this thesis will be given in terms of backscatter power profile.

4.2 ISR Measurement on 22/23 July 2006

On the night of 22/23 July 2006, the ISR observation started at approximately 20:00 LT and ended at 04:00 LT in the early morning. We pointed the radar beam vertically to perform backscatter power and plasma line measurements alternately throughout the night. In each half-hour, we took 20 minutes worth of backscatter power data and 10 minutes worth of plasma line data.

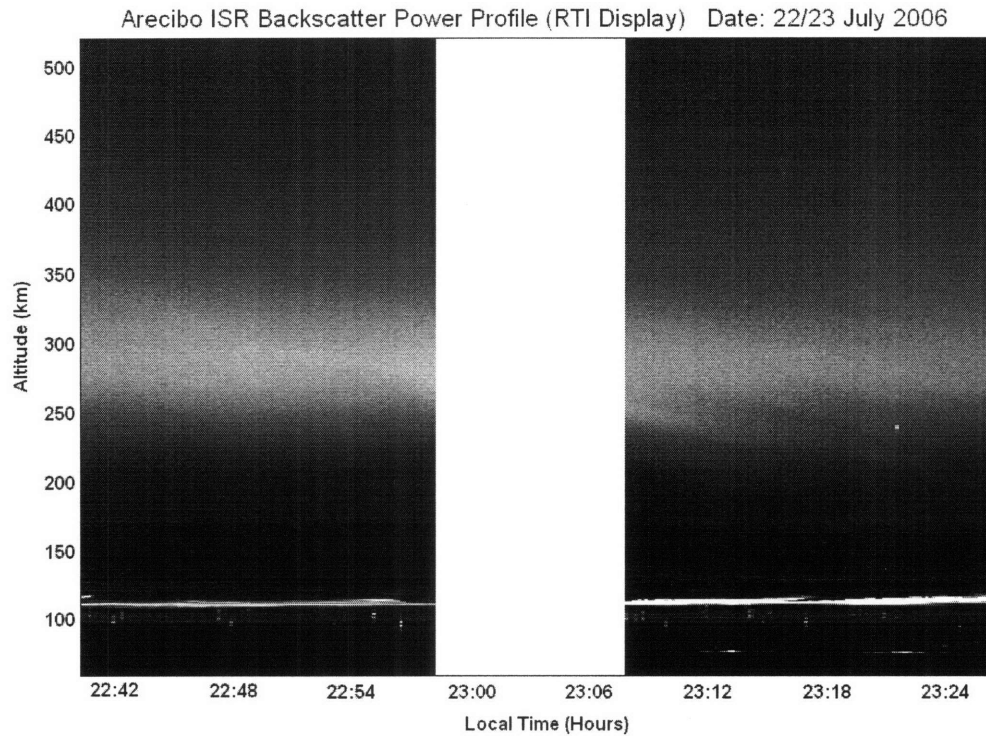


Figure 4-3: RTI plot of radar backscatter power during time period 22:30 LT – 23:30 LT on the night of 22/23 July 2006, showing a slanted stripe structure at ionospheric F region altitudes.

4.2.1 Observation of Slanted Stripe Structure

During the time period 22:30 LT – 23:30 LT, depletions were seen in the backscatter power profile data. In the Range-Time-Intensity (RTI) display of this data (see Figure 4-3), a slanted stripe structure can be seen. The backscatter power measurement was interrupted for ~ 10 minutes for plasma line measurement, which results in a radar data gap around 23:00 LT. From this RTI plot, we can see that an intense and wavy sporadic E plasma layer was also present at around 100 km altitude. This wavy sporadic E plasma layer could be an indication for the presence of strong neutral wind shear in the ionosphere.

In order to see the slanted stripe structure a bit more clearly, one can remove the background signal from the power profile data and isolate the fluctuations. In this thesis, we isolate the fluctuations by subtracting out the smoothed average of 5 consecutive power profiles prior to the power profile of interest. Using this method,

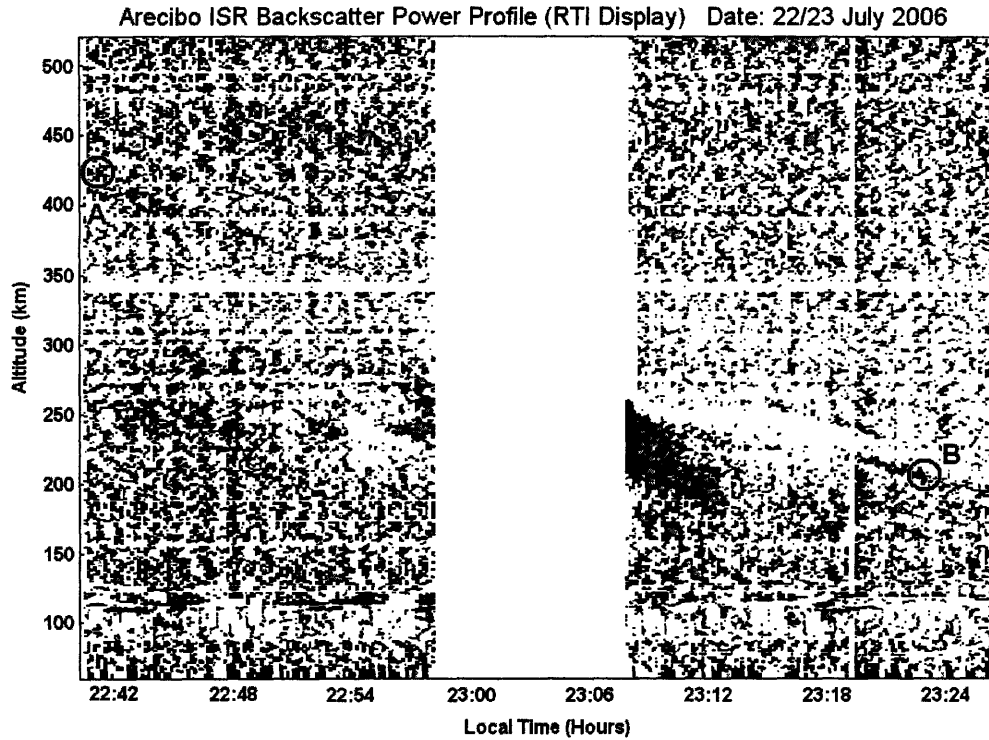


Figure 4-4: RTI plot of net backscatter power perturbations that correspond to the slanted stripe structures observed on the night of 22/23 July 2006 during time period 22:30 LT – 23:30 LT.

the net perturbations in the data were computed and the result is shown in Figure 4-4 as an RTI plot.

From the RTI plot of net backscatter power, the slanted stripe appears as a more coherent pattern compared to the noise-like background, and can be identified without much difficulty. We can now indentify the two end points of this slanted stripes, marked A and B in Figure 4-4. Point A corresponds to an altitude of ~ 424 km at 22:41 LT; whereas point B corresponds to an altitude of ~ 206 km at 23:23 LT. The fact that the stripe is downward-sloping means that the radar beam intercept the upper part of the sctructure first, and the lower part later on. The apparent vertical speed at which the intercepted part is moving down the radar line of sight can then be calculated as $\dot{z} = \Delta z / \Delta t \approx 218 \text{ km} / 42 \text{ min} = 86.5 \text{ m/s}$.

The apparent vertical speed \dot{z} can be used to determine the actual drift speed of these plasma structures, provided that we know in what direction this structure is moving horizontally. The information on the horizontal direction of motion can be

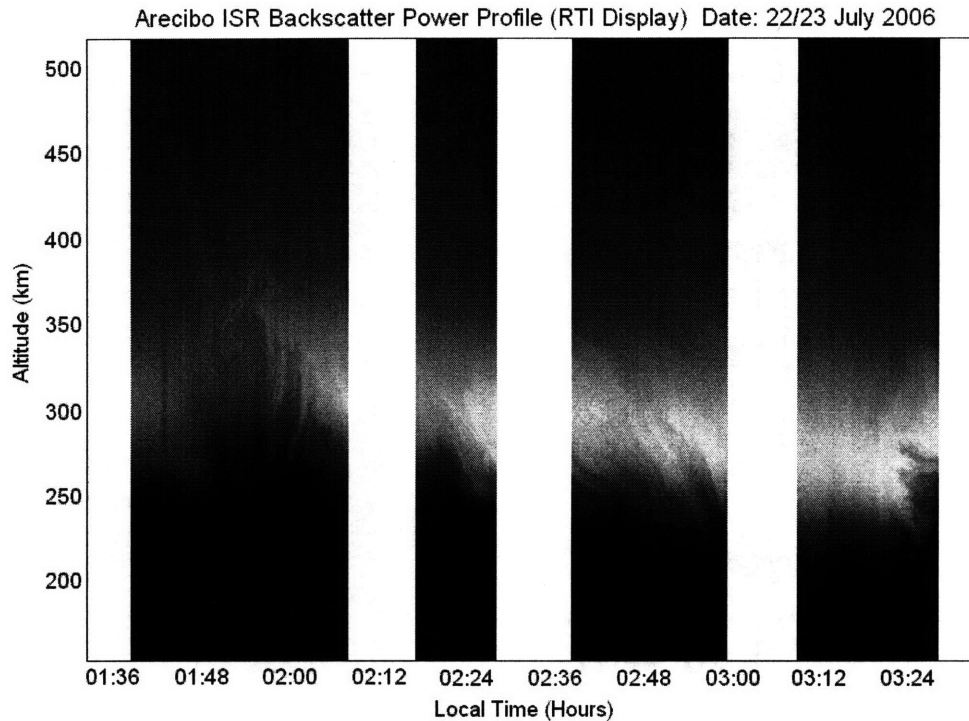


Figure 4-5: RTI plot of radar backscatter power during time period 01:30 LT – 03:30 LT on the night of 22/23 July 2006. A train of turbulent filaments in the F region can be seen from this data set.

obtained from the result of airglow measurement by the all-sky imager. Unfortunately, no recognizable airglow structures were seen in ASIS data during this time period.

4.2.2 Observation of a Train of Turbulent Filaments

During time period 01:30 LT – 03:30 LT on the night of 22/23 July 2006, another set of turbulent plasma structures was seen on the radar backscatter power profile. The RTI plot of radar backscatter power during this time period is shown in Figure 4-5. This time, the observed pattern in the RTI plot is in the form of turbulent filaments. Some of these filaments are upward-sloping or oriented vertically (occurring during \sim 01:48 LT – 02:24 LT), but nonetheless, the majority of them are still downward-sloping.

Unlike the slanted stripe that was observed earlier, these filament structures can be seen sufficiently well in the RTI plot. Therefore, this time we are not going to

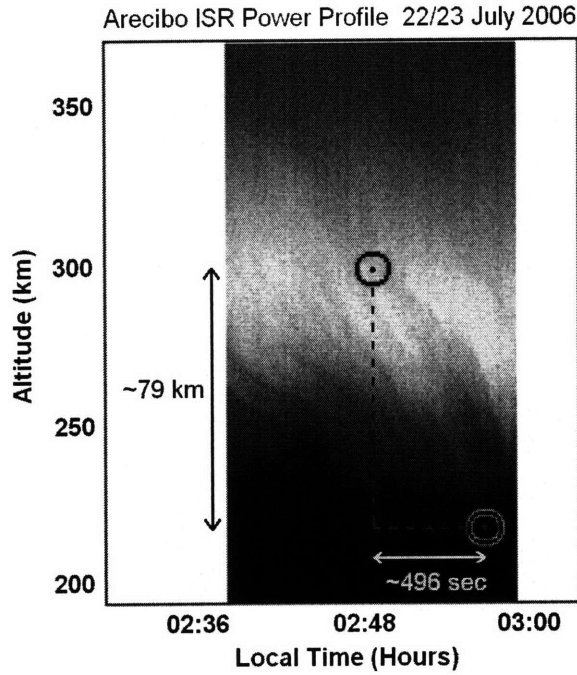


Figure 4-6: Detailed look at a specific portion of the turbulent filaments.

perform any background signal subtraction on the data.

Figure 4-6 shows a detailed view of certain portion of these turbulent filaments, so that we can examine these filaments more closely. In particular, we would like to obtain an estimate for the apparent vertical speed \dot{z} associated with these filaments, which can be found from the slope of these filaments in the RTI plot. We will do so by examining the longest of these filaments, whose ends are marked by the two circles in Figure 4-6. The altitude difference between the two marked ends is approximately 79 km while the time interval between them is approximately 496 seconds, as indicated in the figure. Hence, the slope can easily be calculated to be $\dot{z} = 79 \text{ km}/496 \text{ s} \approx 159.4 \text{ m/s}$.

The value of apparent vertical speed \dot{z} will be used to determine the plasma drift speed of these structures, after combining it with the result of airglow measurement by the all-sky imager. During this time period, an approximately westward-moving airglow structure was seen in the airglow data. A more complete analysis of these turbulent filaments, using both ISR and all-sky imager data, will be presented in Chapter 6 of this thesis.

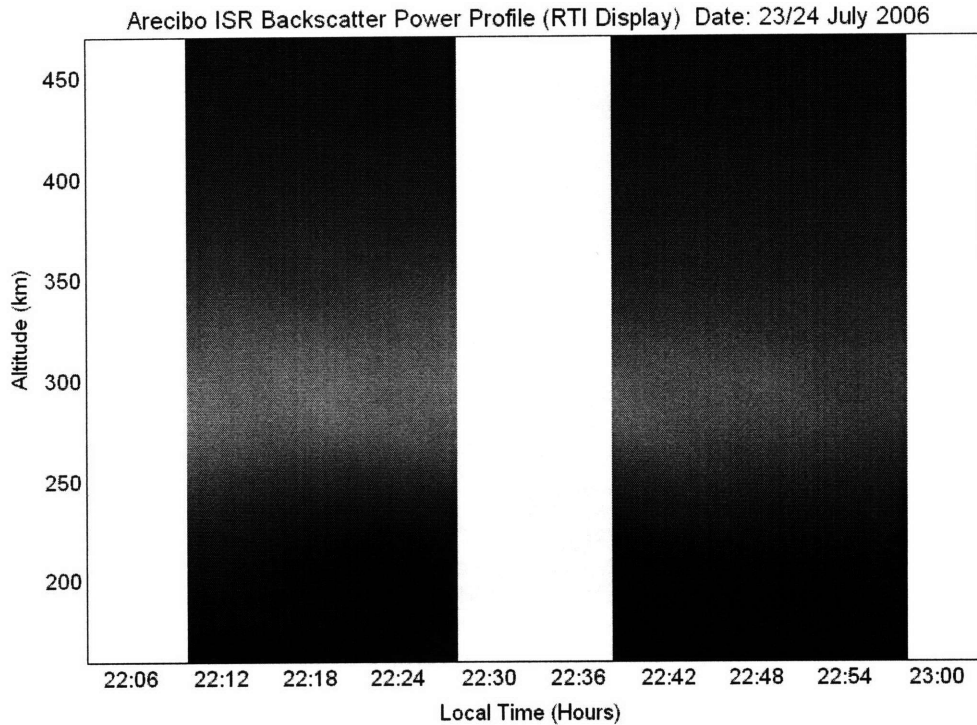


Figure 4-7: RTI plot of radar backscatter power during time period 22:00 LT – 23:00 LT on the night of 23/24 July 2006, showing some of the observed slanted stripes.

4.3 ISR Measurement on 23/24 July 2006

On the night of 23/24 July 2006, the ISR observation started shortly after 19:00 LT and ended at 04:00 LT in the early morning. The radar operation was the same as before, where we pointed the radar beam vertically to perform backscatter power and plasma line measurements alternatingly throughout the night. In each half-hour, we took backscatter power data for 20 minutes and plasma line data for 10 minutes.

4.3.1 Observation of Slanted Stripe Structures

During time period 21:30 LT – 00:45 LT on the night of 23/24 July 2006, a train of slanted stripes/ parallel-plate structures were seen on the RTI plot of Arecibo ISR backscatter power. The RTI plot for the entire ~ 3 hour of this time period had been shown in Chapter 1 of this thesis (see Figure 1-2). We are now going to focus specifically on the parallel-plate structures that were observed during time period 22:00

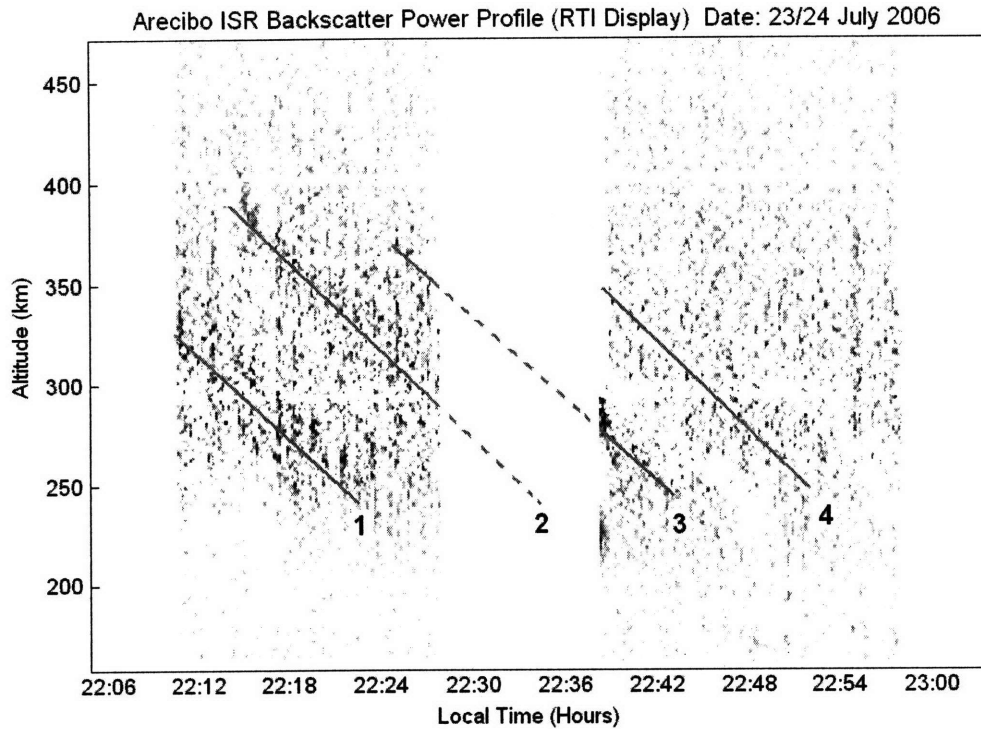


Figure 4-8: RTI plot of net backscatter power perturbations on the night of 23/24 July 2006 during time period 22:00 LT – 23:00 LT. In this RTI plot, four slanted stripe structures can be identified.

LT – 23:00 LT, primarily because this is the time period when an approximately southward-moving airglow structure was also seen in the all-sky imager data. Figure 4-7 shows the RTI plot of radar backscatter power during this one-hour period.

Using the same subtraction method as before, net backscatter power perturbation during this one-hour period was also calculated and the result is shown in Figure 4-8. From the RTI plot of net backscatter power perturbation during this time period, one can identify four distinct slanted stripes (labelled 1 – 4). The slope of these four slanted stripes (in order from #1 to #4) can be estimated to be 117.1 m/s, 122.5 m/s, 110.6 m/s and 120.8 m/s, respectively. The averaged value is thus 117.8 m/s for these four slanted stripes. This slope is the apparent vertical speed \dot{z} that we need for a further analysis of these structures. In addition, the time interval $\Delta\tau$ between each adjacent stripes at ~ 240 km altitude are 684 seconds (stripes 1–2), 540 seconds (stripes 2–3), and 540 seconds (stripes 3–4). On average, the time interval between

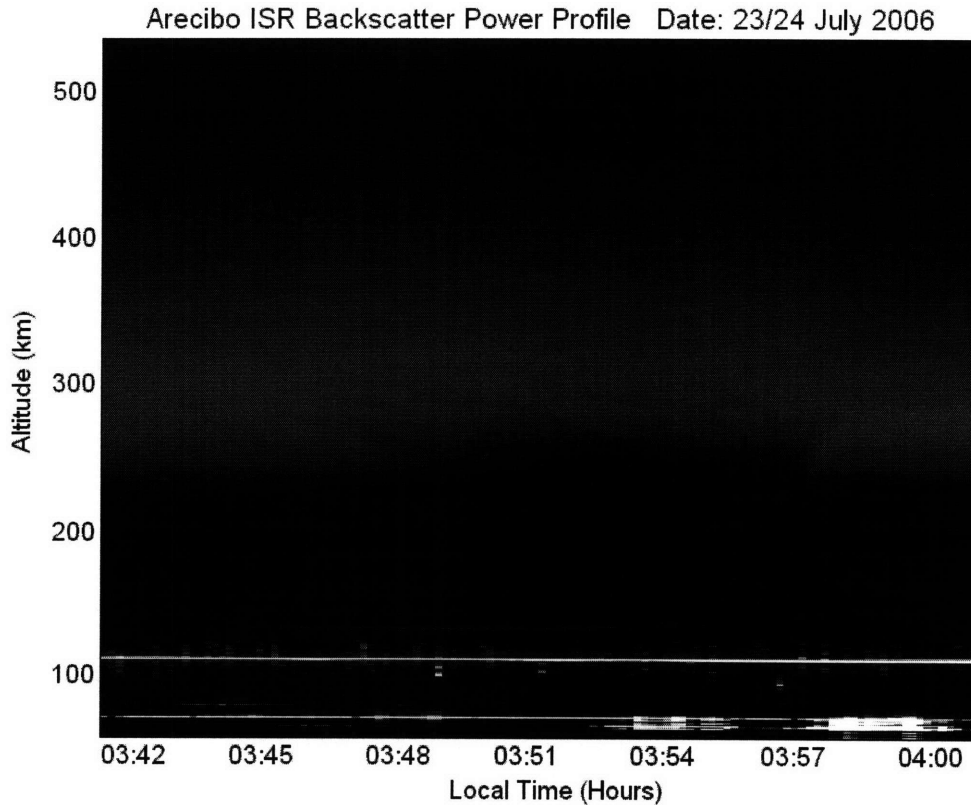


Figure 4-9: RTI plot of radar backscatter power during time period 03:40 LT – 04:00 LT on the night of 23/24 July 2006, where filament structures/ quasi-periodic echoes were seen at ionospheric F region altitudes.

consecutive stripes is then $\langle \Delta\tau \rangle = 588$ seconds. With the value of apparent vertical speed \dot{z} that we had just calculated, we can compute the actual drift speed of these parallel-plate structures from the airglow data. On the other hand, the time interval $\langle \Delta\tau \rangle$ can be used to calculate the scale size/wavelength of these density striations. The complete analysis will be presented in Chapter 6 of this thesis.

4.3.2 Observation of Filament Structures/ Quasi-Periodic Echoes

Approaching the end of our ISR observation hours on the night of 23/24 July 2006, another turbulent structures were seen in the RTI plot of radar backscatter power. Figure 4-9 shows the RTI plot of radar backscatter power during time period 03:40 LT – 04:00 LT, where some filament structures/ quasi-periodic echoes appeared in the data.

In order to better distinguish the filament structures that were observed during

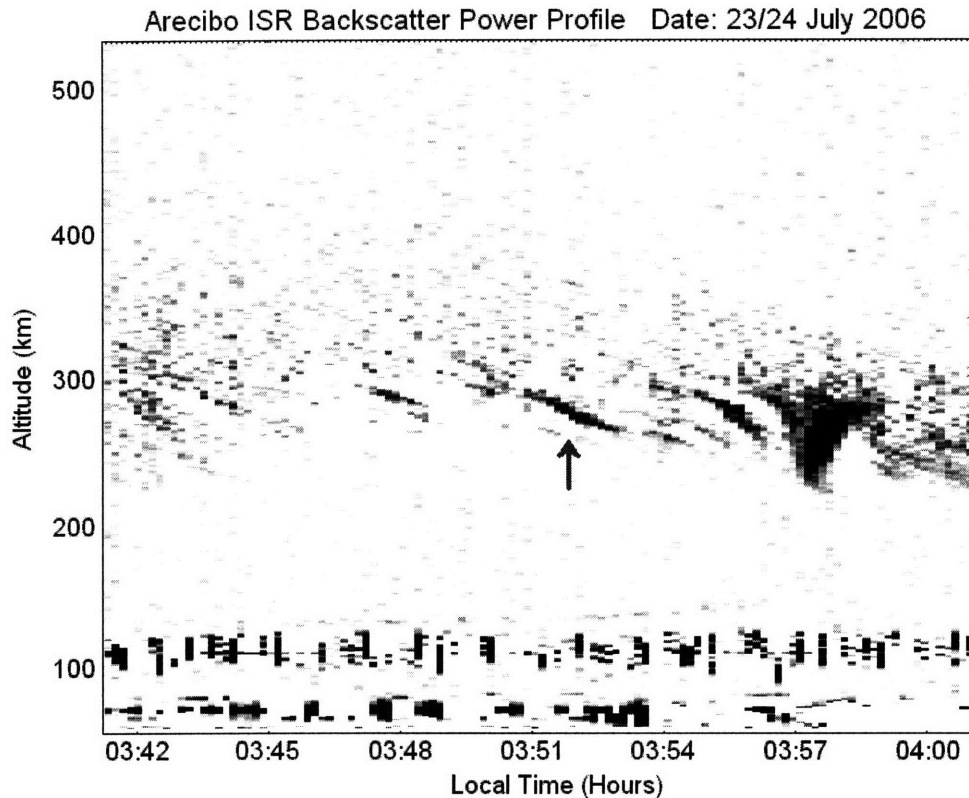


Figure 4-10: RTI plot of net backscatter power perturbations on the night of 23/24 July 2006 during time period 03:40 LT - 04:00 LT. The filaments/ quasi-periodic echoes can now be seen much more clearly. Red arrow marks a particular filament that we used for slope estimation.

this time period, we performed a background subtraction as we did to the parallel-plate structures. The RTI plot of radar backscatter power data after background subtraction is shown in Figure 4-10. This background subtraction turned out to be very effective as one can immediately recognize the shape of these filaments from the RTI plot. We can also see now that these filaments exist at an altitude of just below 300 km, and the time interval between consecutive filaments is roughly 3 minutes.

Finally, we would like to estimate the apparent vertical speed of these filaments so that we can combine it with the all-sky imager data for a more detailed analysis. In order to make this estimate, we are going to focus on one particular filament (marked with a red arrow) that appear at approximately 03:51 LT and calculate its slope. By magnifying the plot around this filament, it can be estimated that the vertical span of this filament is roughly 26.1 km. In addition, the radar detection for its upper and

lower end is separated by a time interval of about 114.5 seconds. The apparent vertical speed of this filament can then be calculated as $\dot{z} = 26.1 \text{ km} / 114.5 \text{ s} \approx 228 \text{ m/s}$.

During this time period, an approximately westward-moving airglow structure was seen in the all-sky imager data. Because we have the information on the horizontal motion from airglow measurement, it would be possible to perform a further analysis to determine the actual drift speed of this filament structure. This analysis, where we combine the ISR data and the airglow data, is going to be given in Chapter 6 of this thesis.

Chapter 5

GPS TEC Diagnostics

One type of diagnostics useful for identifying travelling ionospheric disturbances (TID) is the total electron content (TEC) measurement by GPS satellites [*Rideout and Coster, 2006; Nicolls et al., 2004*]. Arecibo Observatory maintains a database of GPS TEC measurement from 3 (three) nearby GPS receiver stations. These are the Arecibo, PR station (codename aopr); St.Croix, USVI station (codename cro1); and Isabella, PR station (codename pur3). This database can be accessed from the Arecibo Observatory (NAIC) web page at <http://www.naic.edu/aisr/GPSTEC/gpstec.html> where the current and past GPS TEC data can be downloaded. In this chapter, we are going to discuss the GPS TEC data from 23 July 2006 UTC and 24 July 2006 UTC to identify TID structures around the Caribbean area on these two nights.

5.1 The Basics of TEC Measurement using GPS Network

Radio beacon transmissions from GPS satellites used for TEC measurement are the so-called L1 and L2 signals, whose carrier frequencies are 1575.42 MHz and 1227.60 MHz, respectively [*Rideout and Coster, 2006*]. GPS receiver stations on the Earth are going to detect these signals and compare the phase delay between the L1 and L2

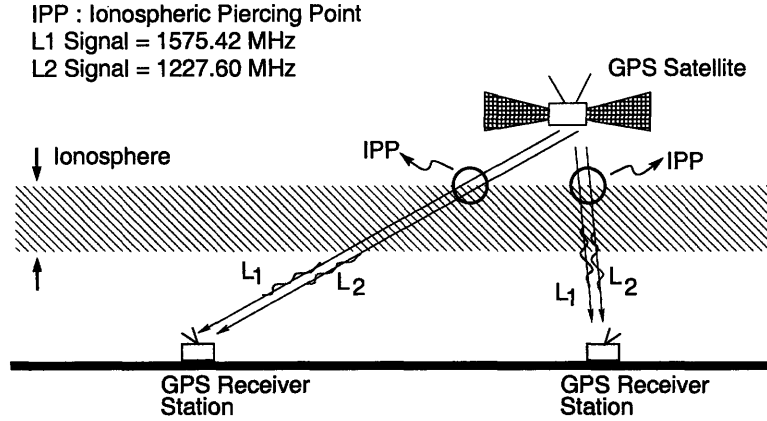


Figure 5-1: A diagram showing the geometry of total electron content (TEC) measurements made by pairs of GPS satellite and receiver station.

signals. This is illustrated schematically in Figure 5-1. The wave phase for a given wave frequency can be written as a line-of-sight integral of the wavenumber:

$$\begin{aligned}\phi &= \int \vec{k} \cdot d\vec{l} = \frac{\omega}{c} \int \left(1 - \frac{\omega_{pe}^2}{\omega^2}\right)^{1/2} dl \approx \frac{\omega}{c} \int \left(1 - \frac{\omega_{pe}^2}{2\omega^2}\right) dl \\ &= \frac{\omega}{c} \int dl - \frac{e^2}{2\omega c \epsilon_0 m} \int n_e dl\end{aligned}\quad (5.1)$$

where we have used O-mode dispersion relation and Taylor expansion because the wave frequency of L1 and L2 signals are much larger than the electron plasma frequency. Thus, the phase difference $\Delta\phi$ ($\equiv \phi_1 - \frac{\omega_1}{\omega_2}\phi_2$) between L1 and L2 is going to be proportional to the line-integrated electron plasma density along the line of sight between the satellite and the receiver [Checcacci, 1970]. The complete expression is going to be given by:

$$\text{STEC} \equiv \int n_e dl = \frac{2\epsilon_0 m \omega_1 c}{e^2} \frac{\omega_2^2 \Delta\phi}{(\omega_1^2 - \omega_2^2)}\quad (5.2)$$

where STEC stands for the slant TEC. The vertical TEC (VTEC) can be computed from the slant TEC through

$$\text{VTEC} = \text{STEC} \cdot \cos \chi\quad (5.3)$$

where χ is the zenith angle, i.e. the angle between vertical direction and the line of sight.

The intersection point between the line of sight and the topside ionosphere (at 450 km altitude) is known as the *ionospheric piercing point* (IPP). The IPP is essentially a point location at the ionosphere where TEC measurements were made. In the database, the calculated slant and vertical TEC are tabulated along with the geocoordinate (longitude and latitude) of the corresponding IPP.

5.2 TID Signatures on GPS TEC Signals for 22/23 July 2006 and 23/24 July 2006

From the GPS TEC data, we would like to identify all existing TID signatures in the recorded signals, and then focus on those which occurred around the same time as the turbulent structures in the ISR and airglow data were recorded. In the GPS TEC signals, TID signatures can be recognized as wavelike fluctuations on top of a more slowly-varying diurnal variations. The amplitude of TEC signal fluctuations associated with TID could range from fractions of TECU to a few TECU. The measurement unit TECU (\equiv TEC Unit) is defined as $1 \text{ TECU} \equiv 10^{16} \text{ electrons/m}^2$.

Each GPS receiver stations in Puerto Rico and US Virgin Islands performs TEC measurement using 30 GPS satellites that orbit around the Earth. Since GPS satellite #12 currently appears to be non-operational, we expect to have 29 sets of GPS TEC data from each receiver station for one day. Nonetheless, the anticipated TID signatures might be found only in some of these data sets because each GPS satellites are passing over the Caribbean at different times with different trajectories. In most cases, clear TID signatures can be seen in the GPS TEC signal if the satellite trajectory crosses the TID wavefront at an almost 90° angle (i.e. when the horizontal component of TID's \mathbf{k} -vector is well-aligned along the trajectory line).

Shown in Figure 5-2 is a set of selected GPS TEC data from 23 July 2006 UTC ($UT = LT + 4 \text{ hours}$), where several TID signatures can be identified. The amplitude

GPS TEC - Isabella, PR Receiver Station (23 July 2006 UTC)

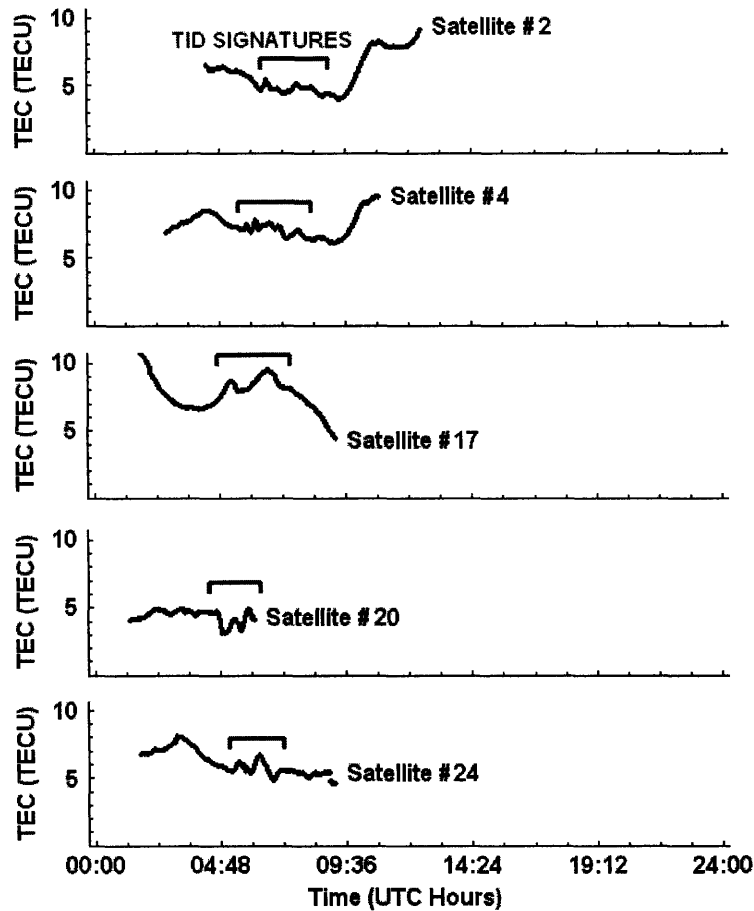


Figure 5-2: Several selected plots of GPS TEC measurement made by the GPS receiver station in Isabella, PR on 23 July 2006 UTC in which TID signatures (wavelike fluctuations in the TEC signal) were seen.

of TEC fluctuations on these TID signatures ranges between 1–2 TECU, and these TID signatures were seen during time period 04:48 UT – 08:20 UT (00:48 LT – 04:20 LT). Since this is the time period when turbulent filament structures were observed in the ISR backscatter power data on the night of 22/23 July 2006, then we can expect that the observed TEC fluctuations on 23 July 2006 UTC are also associated with those turbulent filaments. Based on the amplitude of these TEC fluctuations (1–2 TECU), we could determine that the observed filament structures on the night of 22/23 July 2006 were part of a very intense plasma turbulence.

Figure 5-3 shows another set of selected GPS TEC data, which were recorded

GPS TEC - St. Croix Receiver Station (24 July 2006 UTC)

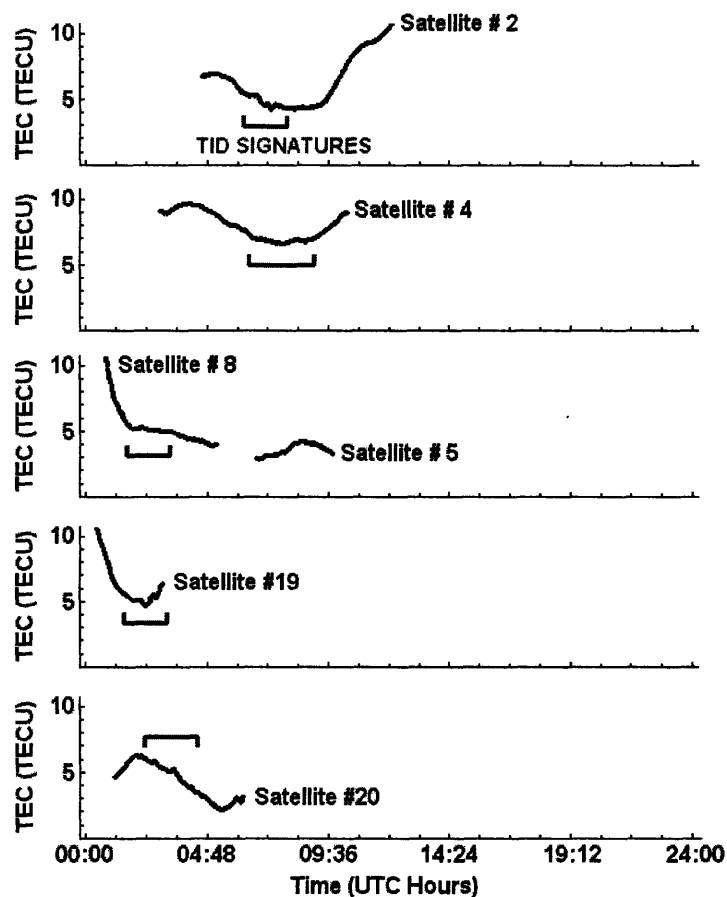


Figure 5-3: Several selected plots of GPS TEC measurement made by the GPS receiver station in St. Croix, USVI on 24 July 2006 UTC in which TID signatures (wavelike fluctuations in the TEC signal) were seen.

on 24 July 2006 UTC (UT = LT + 4 hours). Similar to what we have seen on the previous data set, TID signatures can also be identified in these TEC signals. This time the amplitude of the identified TID signatures were significantly smaller compared to the previous day. Three TID signatures that appeared sooner (satellites #8, #19, and #20) seems to be associated with the parallel plate structures that we observed on the night of 23/24 July 2006. On the other hand, two TID signatures that appeared later (satellites #2 and #4) seems to be associated to the filament structures/ quasi-periodic echoes that were seen at the end of our ISR observation that night.

An overview of GPS TEC data from 23-24 July 2006 UTC in general shows that

significant TEC fluctuations existed around the time period when turbulent structures were observed in the ISR data. The presence of TID signatures in the GPS TEC signals could further support the results from the other two diagnostics (all-sky imager and ISR) that we had already discussed in Chapter 3 and 4 of this thesis.

From these GPS TEC data, we are going to be able to explore the geometry/structure of the observed ionospheric plasma turbulence. At the very least, the orientation of TID's wavefront can be deduced by assessing the geocoordinate locations, i.e. ionospheric piercing point (IPP), of some sequential peaks/bumps in the TEC signals. To its full extent, GPS TEC diagnostics could also be used to produce a full 2-dimensional animated map of TID intensities, which will clearly show the geometry and propagation direction of these disturbances. However, that requires a larger network of GPS receiver stations, which is not quite achievable with only three GPS receiver stations.

5.3 Detailed Analysis of GPS TEC Signal from GPS Satellite #8 on 23/24 July 2006

In this section, we will closely examine a particular GPS TEC data set to confirm the geometry/structure of the observed TID on 24 July 2006 UTC. We would like to see if GPS TEC diagnostics is going to give a result consistent with the parallel-plate structures seen in the Arecibo ISR data on the night of 23/24 July 2006. Specifically, we are going to examine GPS TEC data from satellite #8 on 24 July 2006 UTC. This particular data set is chosen because it contains some TID signatures and the IPPs for this data set were the closest to Puerto Rico during the time period of interest.

The first step in our GPS TEC data analysis is to extract the TEC perturbations (TECP) from the absolute TEC measurement. This is done by removing the background DC signal, leaving only the fluctuations behind. The unwanted background DC signals are the slowly-varying diurnal variations in the TEC measurement (i.e., day-night variations in the TEC due to competing processes of ion production and

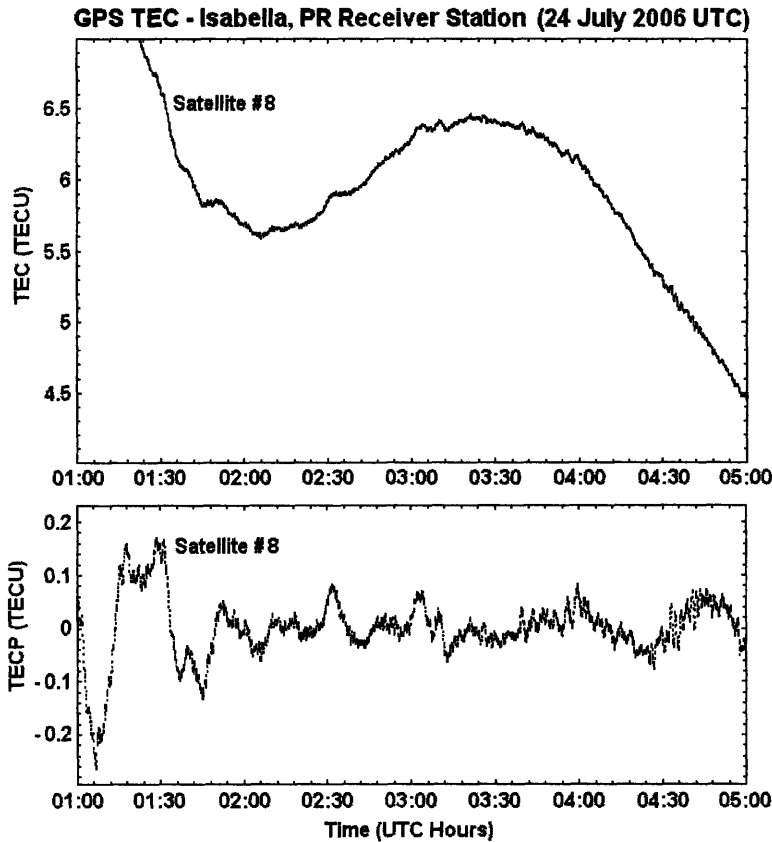


Figure 5-4: Absolute TEC measurement on 24 July 2006 UTC from GPS satellite #8 by Isabella GPS receiver station (upper panel). The corresponding TEC perturbation (TECP) from this measurement after the background signals were removed (lower panel).

recombination in the ionosphere). We can subtract the slowly-varying diurnal variations out by fitting a polynomial function (of a suitable order) to the GPS TEC data. The TECP will then be given by the fitting residuals. The existing TID signatures will be preserved because if the chosen polynomial order is not too high, this fitting function is not going to catch the more rapidly-varying fluctuations associated with TID signatures. In this thesis, a polynomial function of order ranging between 10–12 was used to subtract out the background TEC signal.

Figure 5-4 shows the absolute TEC data from GPS satellite #8 on 24 July 2006 UTC as recorded by the Isabella receiver station (codename pur3), along with the TECP signals after the background signal was subtracted out. In the TECP signals from this data set, TID signatures can be recognized as peaks/bumps with amplitudes

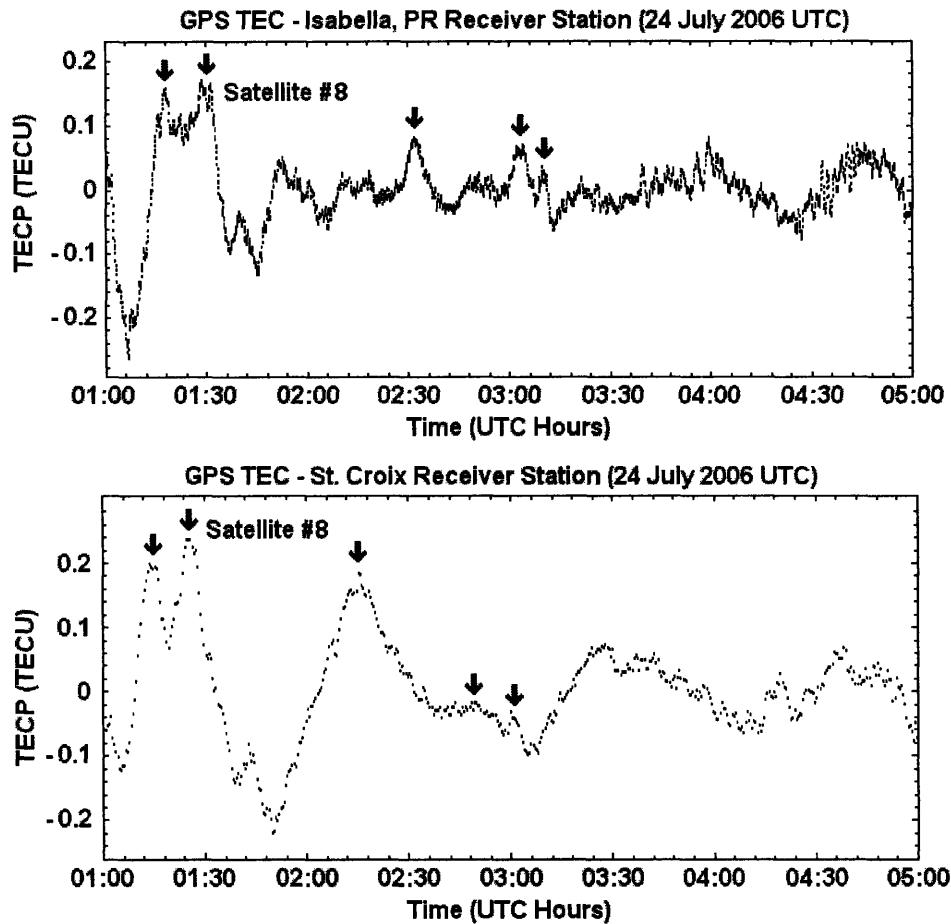


Figure 5-5: A comparison between TECP signals from GPS receiver station in Isabella, PR (upper panel) and St. Croix, USVI (lower panel). The red arrows mark the corresponding TID signatures that can be identified in both TECP signals.

of 0.1–0.2 TECU or so. The width of these peaks (e.g. the one at around 02:30 UT) can be estimated to be around ~ 6 minutes or so. The IPP of GPS TEC measurement from this satellite moves at a speed of approximately 60 m/s, thus each peaks corresponds to wavefronts of plasma disturbances with thicknesses of about $60 \text{ m/s} \times 6 \text{ min} \approx 22 \text{ km}$. This estimate is based on assumptions that the IPP trajectory line is crossing the wavefronts at a $\sim 90^\circ$ angle, and the disturbances are not changing shape very rapidly. As we proceed, it will be shown that the “perpendicular crossing” assumption is indeed justified.

In addition to the data from Isabella station, we also have a simultaneous TEC measurement from St.Croix GPS receiver station based on the same GPS satellite

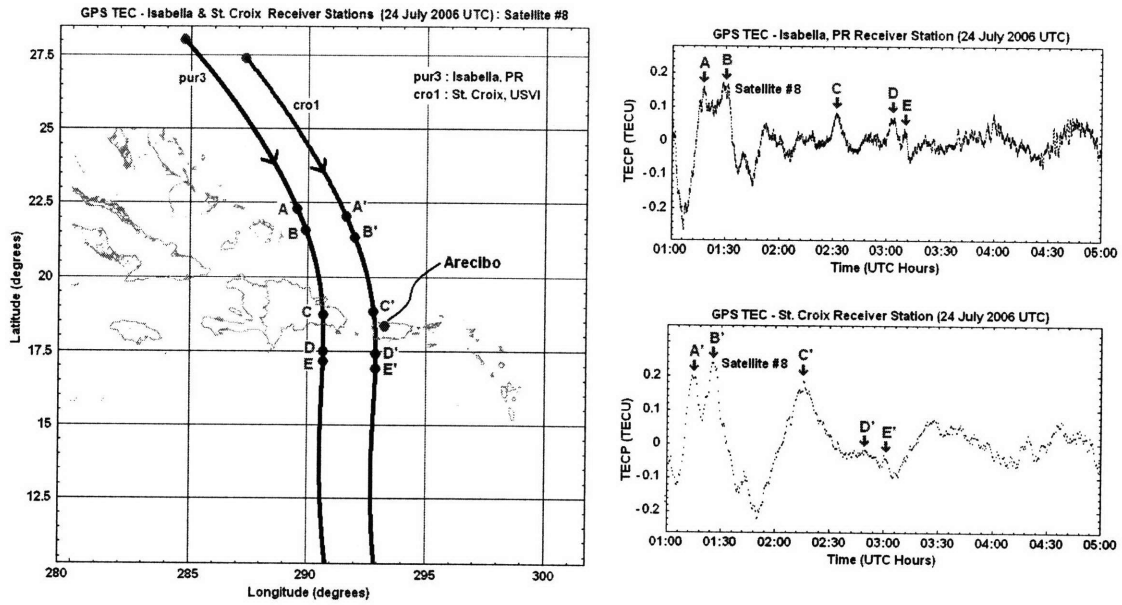


Figure 5-6: Trajectory lines of GPS satellite #8's ionospheric piercing points that correspond to TEC measurements made by Isabella and St. Croix GPS receiver stations, respectively. Also shown along these trajectories are the locations where each of the corresponding TID signatures A–E (Isabella station) and A'–E' (St. Croix station) were detected.

(satellite #8). If we compare the TECP signal from these two stations, we can see some similarities in the signal shape, i.e., a few similar-looking peaks/bumps occurring in the same sequential order. Figure 5-5 shows the TECP signal comparison between these two GPS receiver stations during time period 01:00 UT – 05:00 UT (21:00 LT – 01:00 LT) on 24 July 2006 UTC. From these two data sets, we can identify at least five peaks (each are marked with a red arrow) that made their appearance in both TECP signals.

Shown in Figure 5-6 are the IPP trajectory lines of GPS TEC measurements from Isabella receiver station (codename pur3) and St.Croix receiver station (codename cro1), respectively. St.Croix, USVI is located roughly to the south-east of Puerto Rico, therefore the IPPs of GPS TEC measurement from St.Croix receiver station will generally be located to the east of Isabella station's IPPs. As the IPP of these GPS TEC measurements progressed ~southward over time, TID signatures A–E (A'–E') were sequentially detected by the Isabella (St.Croix) receiver station. The position

of structures A–E and A'–E' along the IPP trajectory lines are depicted as blue dots with their corresponding labels.

Based on their sequential order of appearance and similarities in shape, each peak in one TECP signal should have a corresponding peak in the other TECP signal that had originated from the same TID wavefront (e.g. A & A' should have originated from one wavefront, similarly with B & B' etc). Here we are making an assumption of plane wave geometry, i.e., the TID structures should be \sim uniform along their wavefront. Since peaks A & A' had originated from the same wavefront, then by drawing a straight line connecting A & A', we will obtain one wavefront of these TID structures. By repeating the exact same procedure with pairs of peaks B & B' up to E & E', we will obtain four additional wavefronts. We thus have determined a total of five wavefronts using this analysis.

The five wavefronts that we have just determined are all roughly oriented east-west. Since the IPP trajectory lines are generally oriented north-south, the “perpendicular crossing” assumption that we had stated earlier is therefore well justified. Hence, our analysis of GPS TEC data reveals that the TID wavefronts are oriented approximately east-west, which gives possible northward or southward propagation directions. This is consistent with ASIS data during time period 22:31 LT – 23:31 LT on the night of 23/24 July 2006 which shows a southward airglow motion, as already discussed in Chapter 3 of this thesis.

Chapter 6

Data Discussion

In this chapter, we are going to combine the airglow and ISR diagnostics to obtain a complete picture of the observed ionospheric disturbances. The complete picture will include some information on the exact orientation of the plasma structure as well as the plasma drift speed. We are also going to discuss the potential sources of gravity waves that might have triggered these ionospheric plasma disturbances. We will narrow the possibilities down by ruling out gravity wave sources which were inactive during our stay at the Arecibo Observatory.

6.1 Combined Analysis of Airglow and ISR Diagnostics

Based on the direction of airglow motion, our observations of turbulent plasma structures so far can be divided into two main categories. The analysis for calculating the exact orientation and drift speed in each category is slightly different. The two categories are:

- **Southward propagation** — Plasma density striations in this case are oriented perpendicular to the meridional plane, while these plasma structures are drifting southward and downward. The density striations are expected to be field-aligned, i.e., they make an angle θ with respect to horizontal direction

where θ is the magnetic dip angle ($\approx 50^\circ$ at Arecibo). Figure 6-1 illustrates the geometry of these striations in this case. The $\mathbf{E} \times \mathbf{B}$ plasma drift speed v_d results in an apparent vertical speed \dot{z} in the ISR data and an apparent horizontal airglow motion v_h in the all-sky imager data. Since the angle θ is already known, the only unknown quantity left is the plasma drift speed which can be calculated independently using either ISR or ASIS data. These two independent calculations shall be cross-checked at the end to confirm that the striations are indeed field-aligned.

- **Westward propagation** — Plasma density striations in this case are making a wedge with the meridional plane, while these plasma structures are drifting westward and downward. The angle θ between the meridional plane and the horizontal direction will have to be determined in our analysis. The geometry of these striations in this case is shown in Figure 6-2. In the analysis, we will need to determine both the angle θ and the plasma drift speed v_d using the available information from ISR *and* ASIS data.

From the diagrams in Figure 6-1 or Figure 6-2, one can see that the relation between the apparent vertical speed \dot{z} and the actual plasma drift speed v_d is

$$\frac{v_d}{\dot{z}} = \cos \theta \quad (6.1)$$

whereas the speed of horizontal airglow motion v_h and the plasma drift speed v_d are related through

$$\frac{v_d}{v_h} = \sin \theta \quad (6.2)$$

Therefore, combining the above two equations, the angle θ can be expressed as

$$\theta = \tan^{-1} \left(\frac{\dot{z}}{v_h} \right) \quad (6.3)$$

where the quantity \dot{z} and v_h are determined experimentally from ISR and ASIS data, respectively. If the angle θ is readily known (the case of southward drift), or once the angle θ is determined via Equation 6.3 (the case of westward drift), then the plasma

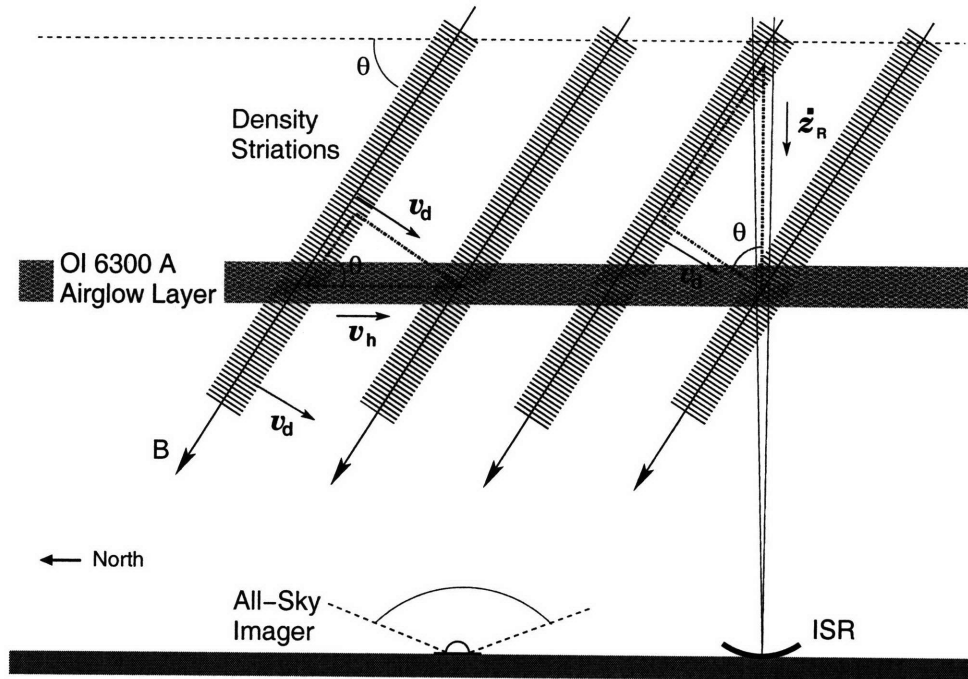


Figure 6-1: The geometry of plasma density striations when the TID structures are progressing southward.

drift speed can be calculated through

$$v_d = \begin{cases} v_h \sin \theta \\ \dot{z} \cos \theta \end{cases} \quad (6.4)$$

With these analytical expressions in hand, we shall now proceed with the analysis.

6.1.1 Train of Turbulent Filaments on The Night of 22/23 July 2006 — Westward Airglow Motion

During the time period when the train of turbulent filaments were observed on the night of 22/23 July 2006 (01:30 LT – 03:30 LT), ISR data shows an apparent vertical speed of $\dot{z} \approx 159.4$ m/s (c.f. Section 4.2.2 of Chapter 4) while ASIS data analysis gives a horizontal airglow motion speed of $v_h \approx 46.3$ m/s (c.f. Section 3.2 of Chapter 3). The ~westward airglow motion tells us that the configuration of these density striations follows the one depicted in Figure 6-2. The angle θ that these striations

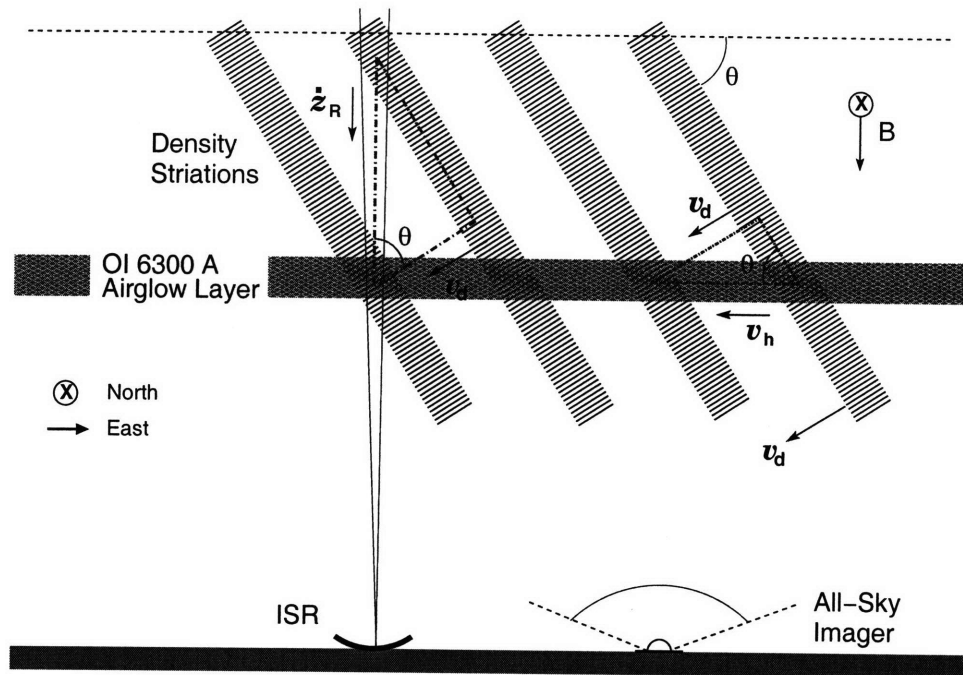


Figure 6-2: The geometry of plasma density striations when the TID structures are progressing westward.

make with respect to the horizontal direction can be calculated using Equation 6.3 to be $\theta = \tan^{-1}(159.4/46.3) \approx 73.8^\circ$. Finally, using either expressions in Equation 6.4, the plasma drift speed can be calculated to be $v_d \approx 44.5$ m/s.

6.1.2 Slanted Stripes on The Night of 23/24 July 2006 — Southward Airglow Motion

Our analysis of slanted stripes in the ISR backscatter power data on the night of 23/24 July 2006 (c.f. Section 4.3.1 of Chapter 4) gives us an apparent vertical speed of $\dot{z} \approx 117.8$ m/s. ASIS data around this time period (22:31 LT – 23:31 LT) had shown a \sim southward airglow motion with horizontal speed of $v_h \approx 97.7$ m/s (c.f. Section 3.3.1 of Chapter 3). The configuration of southward-moving density striations follows the geometry shown in Figure 6-1. The angle θ is evident in this situation ($\approx 50^\circ$, which is the magnetic dip angle) so that information from ISR and ASIS data can be used independently to calculate the plasma drift speed. The ISR data can be used

to determine the plasma drift speed using the second expression in Equation 6.4, which gives $v_d = \dot{z} \cos \theta \approx 76$ m/s. Meanwhile, ASIS data can be used to calculate the plasma drift speed using the first expression in Equation 6.4, which gives $v_d = v_h \sin \theta \approx 74.8$ m/s. We can see that the results of two independent calculations from different diagnostics are in a very good agreement.

Finally, the wavelength/scale size of these density striations can now be determined using the above results. Recall that, on average, the time interval between two adjacent stripes in this case was $\langle \Delta \tau \rangle = 588$ seconds (c.f. Section 4.3.1 of Chapter 4). The horizontal separation between neighboring density striations is then $\langle \Delta X \rangle = v_d \cdot \langle \Delta \tau \rangle / \sin \theta \approx 58.3$ km. Therefore, the wavelength can be calculated to be $\lambda_I = \langle \Delta X \rangle \cdot \sin \theta \approx 44.6$ km. Note that we had used $v_d = 76$ m/s and $\theta = 50^\circ$ for these calculations.

6.1.3 Filament Structures on The Night of 23/24 July 2006 — Westward Airglow Motion

The analysis of ISR data during time period 03:40 LT – 04:00 LT on the night of 23/24 July 2006 (c.f. Section 4.3.2 of Chapter 4) gives an apparent vertical speed of $\dot{z} \approx 228$ m/s associated with the observed filament structures/ quasi-periodic echoes. Meanwhile, ASIS data on the same night during time period 02:00 LT – 03:30 LT reveals a \sim westward airglow motion with horizontal speed of $v_h \approx 67.3$ m/s (c.f. Section 3.3.2 of Chapter 3). The configuration of these westward-moving density striations is specified by the angle θ which can be calculated using Equation 6.3 to be $\theta = \tan^{-1}(228/67.3) \approx 73.6^\circ$. Finally, the plasma drift speed can be calculated using Equation 6.4 to be $v_d \approx 64.5$ m/s.

It is also interesting to note that for both cases of westward airglow motion that we had, the two orientation angles (with respect to the horizontal direction) are approximately the same, i.e., $\theta \approx 74^\circ$.

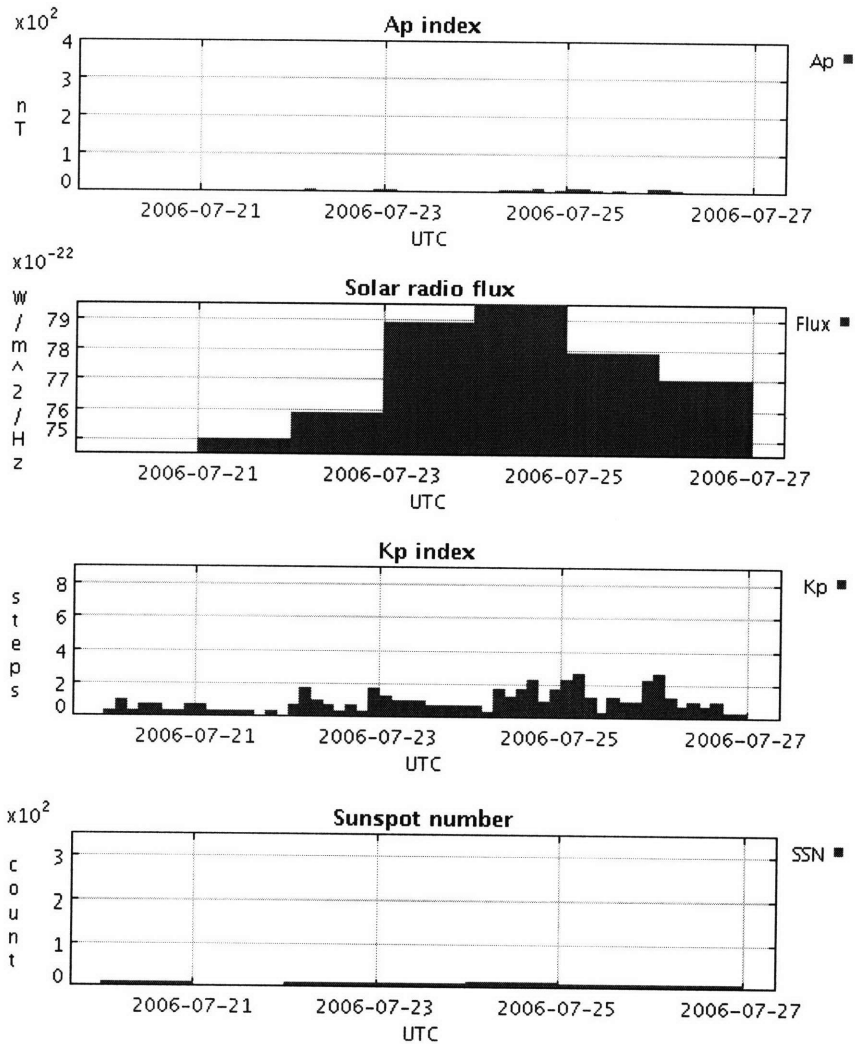


Figure 6-3: Summary plots of space weather condition on 21-27 July 2006 from NOAA’s Space Physics Interactive Data Resource (SPIDR) database [2006]. Low values of A_p and K_p indices show that the geomagnetic condition was quiet during our experiment.

6.2 The Search for Possible Gravity Wave Sources

The TID observed during our July 2006 experiment are likely to be caused by gravity waves that had reached the F region ionosphere from the lower atmosphere. There exist various possibilities for gravity wave sources in general, but we have to identify those ones that were responsible for triggering the observed ionospheric plasma turbulence in this case. Gravity waves could be generated by auroral substorms

[*Nicolls et al.*, 2004], earthquake and/or tsunamis [*Artru, Farges and Lognonne*, 2004; *Artru et al.*, 2005; *Lee et al.*, 2007], jetsreams [*O’Sullivan and Dunkerton*, 1995; *Sato, Kumakura and Takahashi*, 1998], hurricanes [*Bishop*, 2006], or other type of severe weather systems. We shall thoroughly examine these possibilities, rule out the improbable ones, and pin down the most likely source.

One possibility for gravity wave source is geomagnetic activity associated with auroral substorms. Geomagnetic disturbances are usually caused by solar activities such as coronal mass ejections, flares, and radio bursts. Two standard measures of geomagnetic activity are the planetary A_p and K_p indices, which represent the average magnetic field variations across the globe. Planetary A_p index values of $A_p = 29 - 50$ indicate a minor storm, $A_p = 49 - 100$ indicate a major storm, and $A_p > 100$ indicate a severe storm. On the other hand, $K_p \leq 4$ is below storm level while $K_p = 5, 6, \dots$ indicate magnetic storm level G1, G2, ... in NOAA scale [*SPIDR*, 2006].

Shown in Figure 6-3 are summary plots of space weather condition during our stay at the Arecibo Observatory (21–27 July 2006). The planetary A_p and K_p indices were low ($A_p < 29$ and $K_p < 4$), which indicate a generally quiet geomagnetic condition. The data on solar radio flux and sunspot number shows that there were little or no violent solar activities, which also explains the quiet geomagnetic condition during that time period. We can thus rule out auroral source of gravity wave for the observed ionospheric plasma turbulence on 22/23 and 23/24 July 2006.

One might note that there was a slight increase in the 2800 MHz (10.7 cm wavelength) solar radio flux on 23 July 2006 from ~ 75 sfu to ~ 79 sfu (sfu \equiv solar flux unit $\equiv 10^{-22} \text{ W m}^{-2} \text{ Hz}^{-1}$). The 2800 MHz solar radio flux is one of many indicators for the level of solar activity. The base/floor value is ~ 64 sfu, the average value during solar-maximum is ~ 200 sfu, and the “storm value” is around 200–300 sfu [*Belmont, Dartt and Ulstad*, 1965; *Tapping and DeTracey*, 1990]. Thus, the increase in solar radio flux to ~ 79 sfu on 23 July 2006 was generally not an important event as the flux is still far below the storm level. In principle, EM radiation at this microwave frequency (2800 MHz) could produce significant plasma density and magnetic field fluctuations if the power flux is intense enough [*Lee and Kuo*, 1984]. However, the

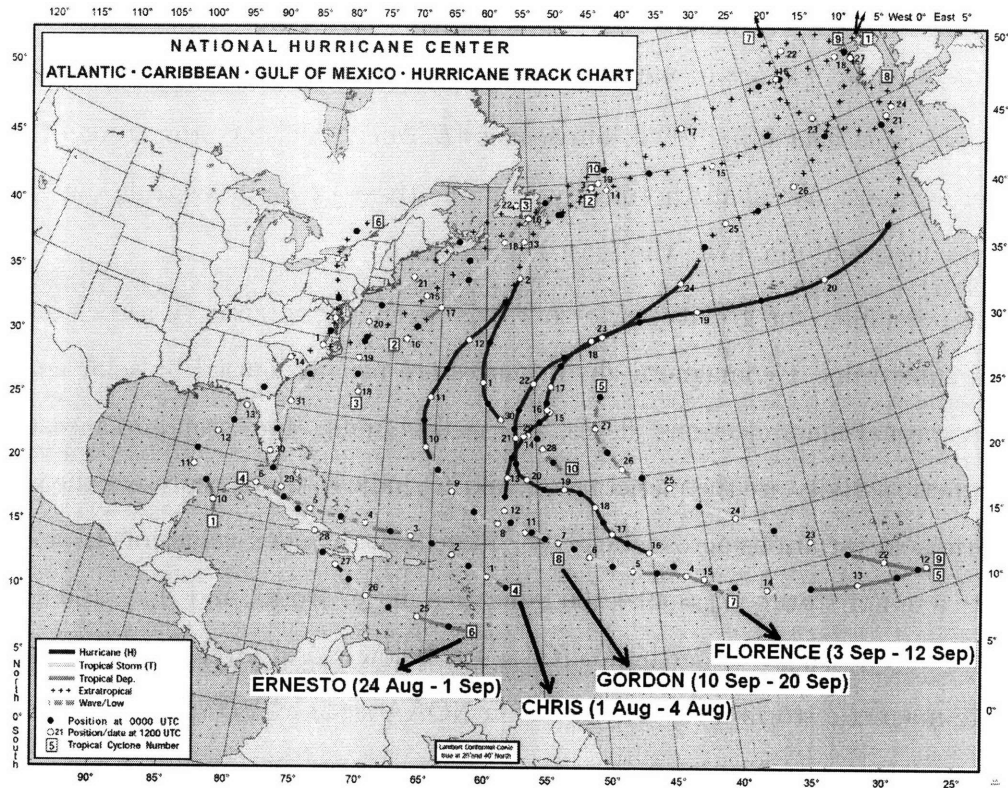


Figure 6-4: Hurricane track map for the 2006 Atlantic hurricane season [National Hurricane Center, 2006]. No major hurricane had passed near Puerto Rico during our experiment.

solar 2800 MHz radio flux intensity in any case is too weak (in the order of $10^{-22} \text{ W m}^{-2} \text{ Hz}^{-1}$) to have any direct effect on the Earth's ionosphere.

Since the geomagnetic condition was generally quiet during our experiment, we must now look for meteorological sources of gravity wave. Hurricane is one of the possibilities that we should look into. Hurricane is a potential source that can produce gravity waves with a broad spectrum of wavelengths [Bishop, 2006]. However, only large-scale (=long wavelength) gravity waves would be able to trigger plasma turbulence in the ionospheric F region. Short-scale gravity waves usually could not reach an altitude that high and would be dissipated at much lower altitudes.

Figure 6-4 shows the NOAA hurricane track chart for the 2006 Atlantic hurricane season [National Hurricane Center, 2006]. From this hurricane map, we can see that no major hurricane had passed near Puerto Rico during our stay at the Arecibo Observatory (21–27 July 2006). During the 2006 Atlantic hurricane season, the closest

encounters with Puerto Rico were hurricane Chris (1–4 August), Ernesto (24 August – 1 September), Gordon (10–20 September), and Florence (3–12 September). All of these encounters occurred weeks after our observations at the Arecibo Observatory had ended. We can thus rule out hurricanes as potential source of gravity waves that could have triggered the observed plasma structures on 22/23 and 23/24 July 2006.

Another potential source of gravity waves that could induce TID are earthquake and/or tsunamis. However, to the best of our knowledge, there was no major earthquake or tsunamis during our stay at the Arecibo Observatory (21–27 July 2006). Therefore, earthquake/tsunami-induced gravity waves shall be ruled out from the list of possible scenarios to explain our experimental result.

So far we have ruled out several major sources of gravity waves since none of them were active during our experiment. Let us recapitulate our findings so far: (1) We expect that the observed TID on the night of 22/23 and 23/24 July 2006 were induced by gravity waves; (2) The responsible source of gravity waves is expected to be meteorological/terrestrial in origin since the geomagnetic condition was quiet during that time period; and (3) No major hurricanes, earthquakes, nor tsunamis were present during that time period as a source of gravity waves.

From the intensity of the observed ionospheric plasma turbulence, we know that the energy source which produced these gravity waves should be a strong one. In order to obtain useful clues on the probable cause of these plasma turbulence, we thus have to find a major meteorological event that occurred coincidentally or overlapped with our TID observations at Arecibo.

A notable weather anomaly that occurred near the end of July 2006 was the heat waves that swept across North America from the northwest towards the southeast [ASDC, 2006; NASA, 2006]. During the last two weeks of July 2006, the reported land temperature over the United States was significantly higher than the past six year average by $\sim 10^{\circ}\text{C}$ or so [NASA, 2006]. Through convection and release of latent heat, intense gravity waves could be generated during such weather event [Nappo, 2002; Manzini and Hamilton, 1992]. Judging from the scale, magnitude, and timing of this weather anomaly, the July 2006 US heat waves shall definitely be considered

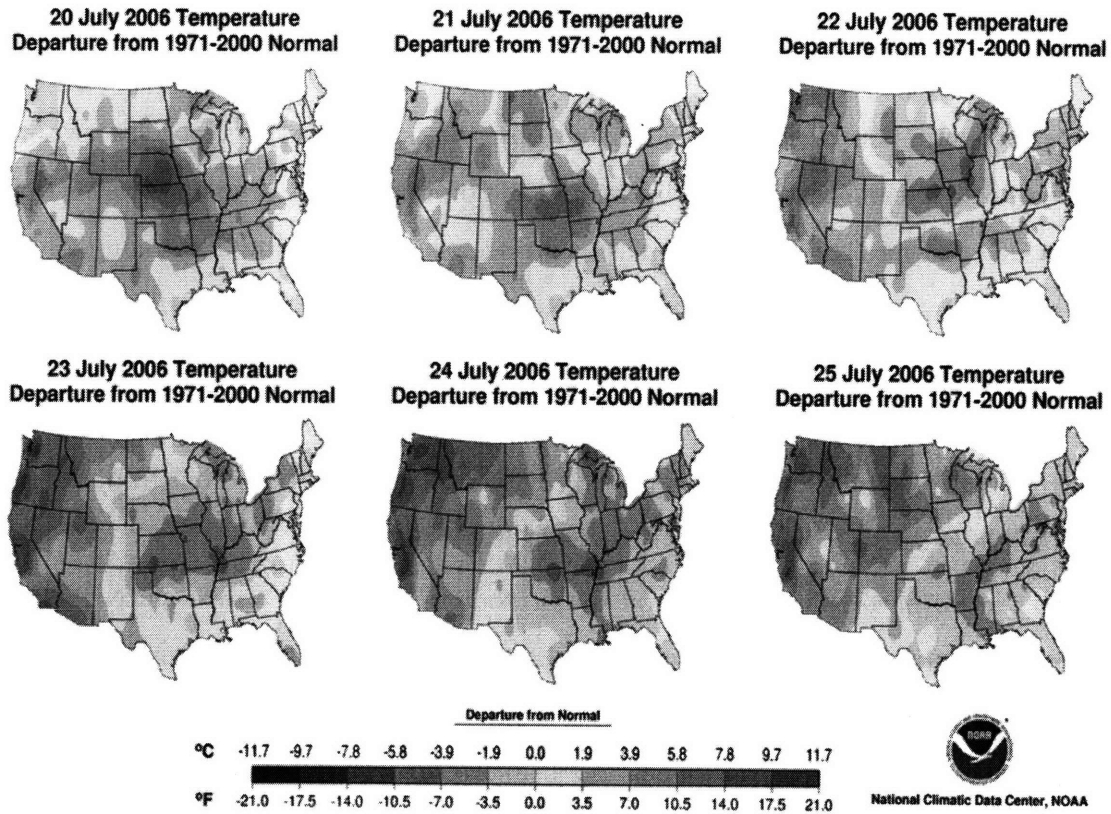


Figure 6-5: The progression of summer 2006 North American heat waves on 20–25 July 2006. Data from the National Climatic Data Center, NOAA [2006].

as a plausible source of gravity waves that we are searching for.

This speculation is not at all unreasonable because heat waves in general will control the formation of weather fronts, which in turn will become the driving source for various severe weather systems [Cole, 1980]. There had been reports on thunderstorms, wind, and tornadoes that occurred in various places as the heat waves swept across the United States [NOAA Weather Service, 2006]. It was thus possible that as the heat wave left the Southeastern United States, the transported heat then continued to seed more atmospheric disturbances over the Gulf of Mexico and the Caribbean.

Figure 6-5 shows the distribution of temperature anomaly—relative to the past 30-year average/normal temperature—over the United States during the last few days of July 2006 [NCDC, 2006]. From the depicted six-day evolution of temperature anomaly distribution on 20–25 July 2006, one can clearly see the southeastward

progression of the summer 2006 US heat waves. After passing through the United States, these hot air masses will eventually reach the coast where they could either move towards the Gulf of Mexico, the Caribbean, or the Atlantic Ocean. If the data coverage had included the temperature anomaly over the ocean as well, then it would have been clear how the heat waves continued to progress afterwards.

We thus have arrived at a resolution that the summer 2006 US heat wave was the most plausible source to have triggered the observed ionospheric plasma turbulence over Arecibo on 22/23 and 23/24 July 2006. This is the most likely scenario since other types of gravity wave source that we have considered so far were inactive around that time period. Based on the timing, magnitude, and scale of this weather event, the summer 2006 US heat wave seems to best fit the criteria for gravity wave source that we are searching for. Our analysis has revealed a scenario where temperature gradient associated with the heat wave is acting as a source of free energy to generate gravity waves which subsequently excite plasma disturbances in the ionosphere.

Chapter 7

Conclusion and Future Research

Using airglow, ISR, and GPS TEC diagnostics, we have examined the highly-structured ionospheric plasma turbulence over Arecibo that was observed on the nights of 22/23 and 23/24 July 2006. Primarily based on ASIS and Arecibo ISR data, we have accurately calculated the orientation and plasma drift speed of the associated density striations in each respective cases. The analysis also reveals that the wavelength/distance of separation between two adjacent striations is in the order of ~ 50 km (or, tens of kilometers in general).

The presence of wavy sporadic E plasma layer around the time period, when turbulent F region plasma structures were observed in the ISR data, indicates that these plasma disturbances were induced by internal gravity waves that had reached ionospheric F region altitudes from the lower atmosphere. We have considered various scenarios of possible gravity wave source that might be responsible for causing the observed ionospheric plasma turbulence, and we have ruled out gravity wave sources which were inactive during that time period. From all scenarios that we have considered, we finally found that it is highly likely for the summer 2006 US heat waves to be the driving source of these gravity waves.

The revealed potential connections between the intense ionospheric plasma turbulence and the heat waves could have a rather important implication on several other research areas/disciplines as well. The field of meteorology might be directly impacted because heat waves could yield severe weather events that would not nor-

July 2006 Heat Waves: North America & Western Europe

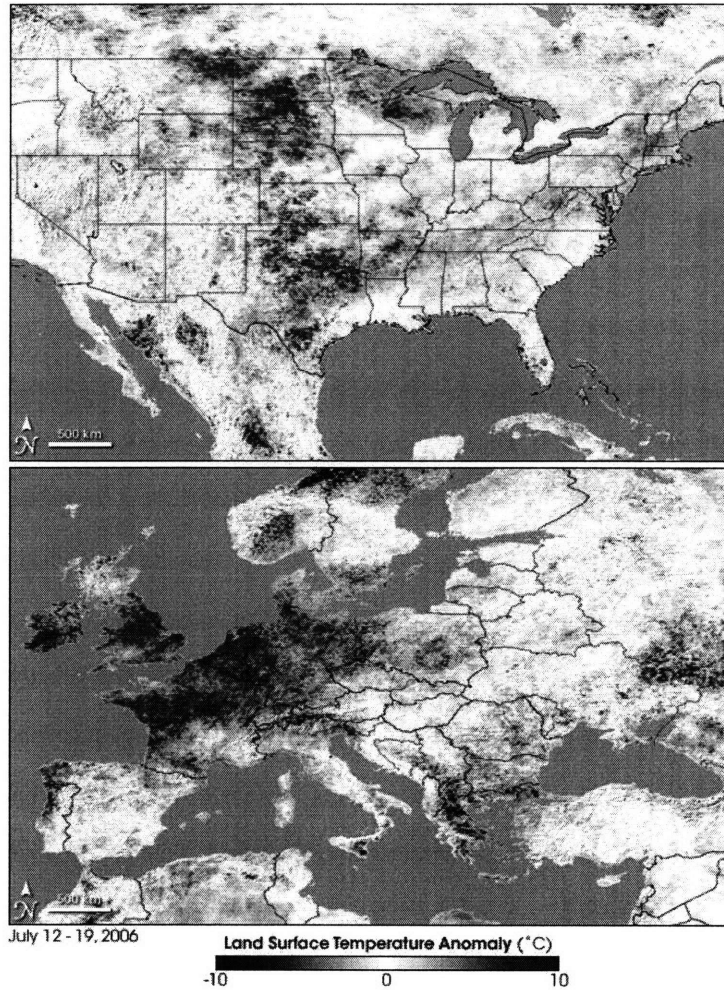


Figure 7-1: North American and West European heat waves during summer 2006 as mapped by the Moderate Resolution Imaging Spectroradiometer (MODIS) on NASA's Terra satellite [2006].

mally happen. Furthermore, the field of climatology might also become important in this case because climate change tends to bring forth more weather anomalies over time. Finally, the issue of global warming as the root of climate change could also be brought into the picture. This finding therefore suggests that climate change—with global warming as one of its driving factors—is going to affect not only tropospheric weather system but also space environment in general.

The theory that the summer 2006 US heat wave was the driving source of gravity waves to trigger the observed ionospheric plasma turbulence over Arecibo could lead

to a few additional predictions, which will need to be verified. If heat waves that had left the coast were able to cause intense TID over the Caribbean, then we can expect to have more ionospheric plasma turbulence over the mainland as the heat wave swept across North America during this time period. Furthermore, it should be noted that western Europe also experienced a heat wave during summer 2006, at about the same time as the US heat waves. This fact leads to another prediction that intense TID might have also occurred over the western Europe as the aforementioned heat wave swept across it. Figure 7-1 shows the temperature anomaly distribution over North America and Western Europe during these two respective heat wave events, as mapped by the Moderate Resolution Imaging Spectroradiometer (MODIS) on NASA's Terra satellite [NASA, 2006].

In the planned future research, the above predictions are going to be tested so that we can gain more insight to this phenomenon. Using the world-wide GPS TEC data set from Madrigal Database (<http://madrigal.haystack.mit.edu/>), we could compile 2-D geographical maps of TEC over various parts of the world to identify TID signatures. The world-wide GPS TEC data had been proven useful to image and identify gravity wave-induced TIDs, as demonstrated recently for the case of gravity waves caused by auroral substorms and by the 2004 Sumatra earthquake/tsunami [Lee *et al.*, 2007 and references therein]. Needless to say, the amount of data that need to be handled might be quite massive because this database integrates the recorded TEC data from almost all GPS receiver stations around the globe. After the TECP signals are successfully extracted from this data set, we would be able verify the existence of TID over the North American continent and Western Europe during this time period.

This research timely adds an important item to the list of potential ecological effects related to the global warming. That is, abnormal space weather conditions associated with intense plasma turbulence would alter the geoplasma environment [Pradipta *et al.*, 2007; Labno *et al.*, 2007], that would affect not only satellite operation and communications, and power systems on the Earth, but also the protection of astronauts from outer space radiations. Further investigation of the concerned physical process, namely, heat-source-induced gravity waves to trigger large space plasma

turbulence can be conducted at Gakona, Alaska using the newly constructed High-Frequency Active Auroral Research Program (HAARP) heating facility [*Pradipta et al.*, PARS Summer Experiments (I) and (II), 2007]. In short, quickly scanning and/or modulate ionospheric plasmas with the HAARP heater at ultra low frequency (ULF) would create temperature gradients to drive gravity waves for the controlled study of this intriguing phenomenon discovered at Arecibo.

Appendix A

Geocoordinate Transformations for All-Sky Imaging Data

In performing airglow measurements for ionospheric plasma diagnostics, a fisheye lens (180° field of view) is used on the all-sky imaging system (ASIS). Consequently, the acquired image will show a warped (distorted) snapshot of airglow spatial distribution. In order to perform intensive analysis of the airglow data (e.g. tracking of airglow motion), the data array must be transformed (unwarped) properly into linear geographic coordinates first. This transformation will give us a spatial distribution of airglow in terms of zonal (east-west) and meridional (south-north) distances from the location of ASIS.

A.1 Data Array Manipulations

The raw data array from ASIS (650×670) has a structure similar to that of image files (i.e. top row of the image is located in the beginning of the datafile). Thus, surface plots of ASIS data generated using standard plotting commands in MATLAB or Mathematica will give us an upside-down image of the actual airglow snapshots recorded by ASIS. In the airglow lab at the Arecibo Observatory, ASIS was mounted such that each original snapshots will show the eastern sky at the top of the frame and the northern sky at the right side of the frame. Therefore, the first step of our

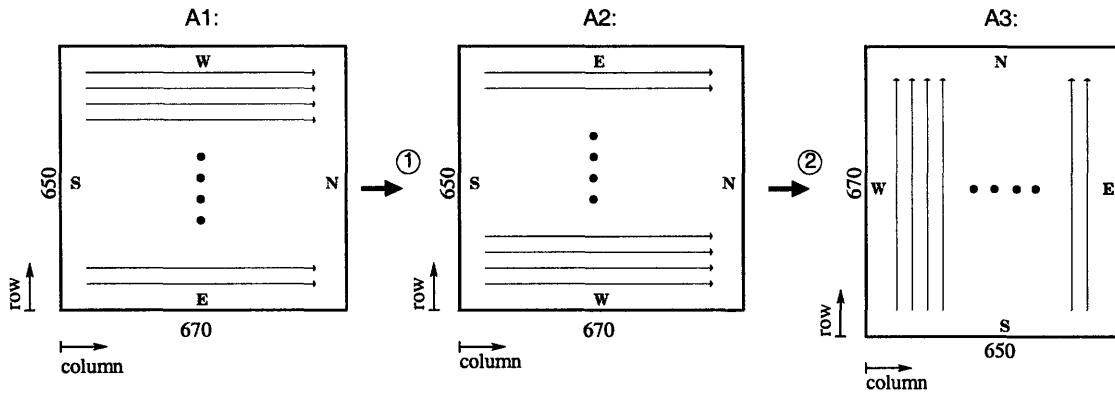


Figure A-1: A schematic description of the first two steps of the required array manipulations before a more intensive analysis can be performed on the ASIS airglow data.

array manipulation is to correct the raw data array format so that standard plotting commands in MATLAB and Mathematica will be able to properly display the original snapshots.

The original ASIS snapshots are “bottom-view” images because the camera is looking up the sky from the ground. In a bottom-view image, the direction of North (South) and East (West) are interchanged, unlike in typical maps, thus creating a potential confusion when examining the airglow data. Therefore, the second step is to transform bottom-view images into top-view images where the direction/orientation of North (South) and East (West) are more intuitive.

The above two steps are illustrated graphically in Figure A-1. Array **A1** is the raw data array format, which can be transformed into the bottom-view array **A2** by reversing/flipping it. The top-view array **A3** is then obtained through transposing the array **A2**.

Once the data arrays are “top-view” images, the sense of direction/orientation has become more convenient for data examination. However, the top-view images do not represent the spatial distribution of airglow in terms of linear distances in geographic coordinates that we need for a more intensive analysis of the data. Therefore, the final step of our array manipulation is to transform top-view images into geographical airglow intensity map represented in linear distances (e.g. kilometers).

In top-view images, each pixel corresponds to a certain direction within the all-sky

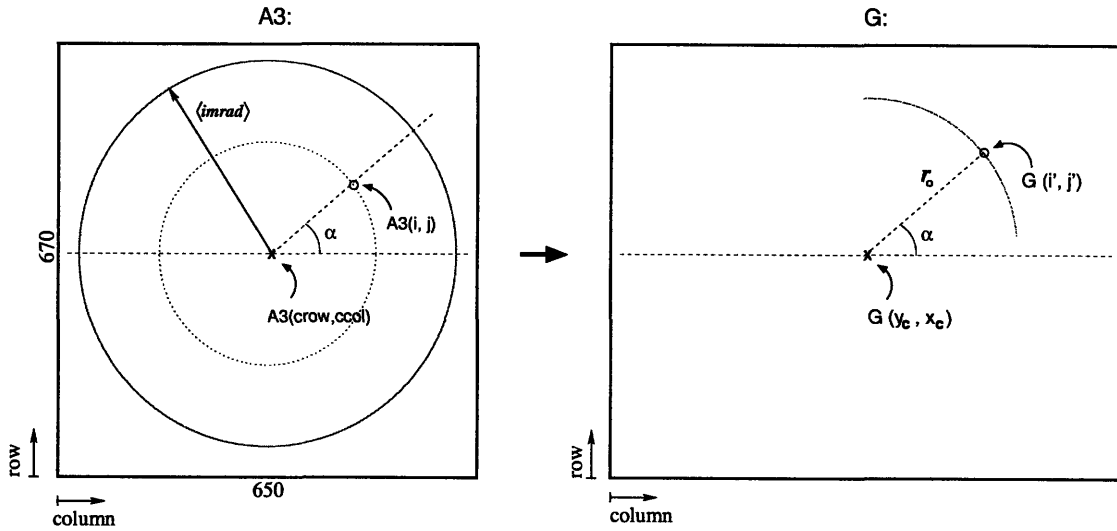


Figure A-2: Transformations from the top-view array **A3** into the geographical array **G**. Matrix element $\mathbf{A3}(i, j)$ from top-view array will become matrix element $\mathbf{G}(i', j')$ in geographical array.

imager's field of view. This direction is specified by two angles: the azimuth angle α (taken to be counter-clockwise from the east) and the zenith angle θ (zero zenith angle will be directly overhead). The azimuth angle α can be determined directly if we know the location of center pixel $\mathbf{A3}(crow, ccol)$ that corresponds to zenith direction. Furthermore, the zenith angle θ can be determined if we also know the radius of the image $\langle imrad \rangle$, which is equal to the distance from the center pixel to the image edge where the zenith angle there by definition is 90° . This is illustrated schematically in Figure A-2. Note that the azimuth angle α is an invariant between the top-view array **A3** and the geographical array **G**.

For a given matrix element $\mathbf{A3}(i, j)$, the analytical expressions for these angles in terms of the center row $crow$, center column $ccol$, and image radius $\langle imrad \rangle$ are:

$$\theta = 90^\circ \times \frac{\sqrt{(i - crow)^2 + (j - ccol)^2}}{\langle imrad \rangle} \quad (\text{A.1})$$

$$\sin \alpha = \frac{(i - crow)}{\sqrt{(i - crow)^2 + (j - ccol)^2}} \quad (\text{A.2})$$

$$\cos \alpha = \frac{(j - ccol)}{\sqrt{(i - crow)^2 + (j - ccol)^2}} \quad (\text{A.3})$$

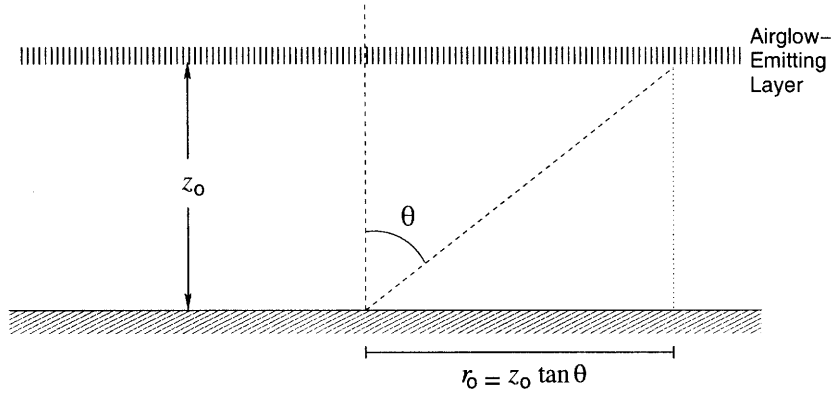


Figure A-3: Basic geometry relating the height of airglow layer to the horizontal extent of airglow measurement using an all-sky imager.

In practice, the center row $crow$, center column $ccol$, and image radius $\langle imrad \rangle$ will be obtained from curve fitting of the image edge location using a sample image.

In order to perform the transformation into geographical array \mathbf{G} , we also need to assume the height of the airglow-emitting layer z_0 . From z_0 and θ , we can determine the horizontal distance r_0 between the all-sky imager's location and the point where the airglow is emitted. This is depicted in Figure A-3. Assuming that the all-sky imager's location corresponds to the matrix element $\mathbf{G}(y_c, x_c)$ in the geographical array, the transformed location for the matrix element $\mathbf{A3}(i, j)$ will be $\mathbf{G}(i', j')$ where i' and j' are given by

$$i' = y_c + z_0 \tan \theta \sin \alpha \quad (\text{A.4})$$

$$j' = x_c + z_0 \tan \theta \cos \alpha \quad (\text{A.5})$$

The actual height of the airglow layer is roughly 90 km for 5577 Å OI green emission, and around 250-300 km for 6300 Å OI red emission. Note, however, that the value of parameter z_0 in the array transformation does not have to strictly follow these actual values. Essentially, the parameter z_0 is only going to control the size of the geographical array \mathbf{G} . A large value of z_0 will give us a good resolution around zenith but will cause the airglow intensity map to be severely fragmented near the edge, and vice versa. Therefore, the value of z_0 can be adjusted to meet the specific

needs of a particular analysis. Thus, one is free to choose the value of z_0 but has to keep the actual airglow height (in kilometers) in mind when scaling the final plot. In this thesis, the value of z_0 has been chosen to be $z_0 = 50$ to obtain a reasonable zenith resolution without fragmenting the edges.

A.2 Determining Center Pixel and Image Radius

The 90° edge of an ASIS image is approximately a circle, closely following the shape of all the lenses/apertures inside the optical instrument. Thus, by locating the image edges and fitting these edge points analytically to a circle, we can determine the center pixel ($crow$, $ccol$) and the image radius ($imrad$). Figure A-4 shows an ASIS image that was used for this analysis. For a pixel outside the 90° edge, none (or very few) of the photon that originates from airglow emission will be impinging on it. Hence, electron counts at such pixel will be purely random dark noise due to thermal agitation at the CCD. In other words, outside the 90° edge, the nature of the CCD signal pattern will be almost completely random. We are going to use this as a standard for finding the image edge.

From the contour plot of sample ASIS image shown in Figure A-4, we can see a more or less clear boundary between region with “clean” contours and region with clusters of random pattern. This boundary can be determined with ~ 2 pixel precision by visually examining the data. The next step is to fit these edge points to an analytical function for a circular curve:

$$\begin{aligned}
 (x - ccol)^2 + (y - crow)^2 &= \langle imrad \rangle^2 \\
 y - crow &= \pm \sqrt{\langle imrad \rangle^2 - (x - ccol)^2} \\
 y &= crow \pm \sqrt{\langle imrad \rangle^2 - (x - ccol)^2} \tag{A.6}
 \end{aligned}$$

where the +ve (-ve) sign corresponds to the upper (lower) arc of the circle.

The presence of a square root expression can cause some problems in the curve fitting process because it potentially gives an imaginary number when the quantity

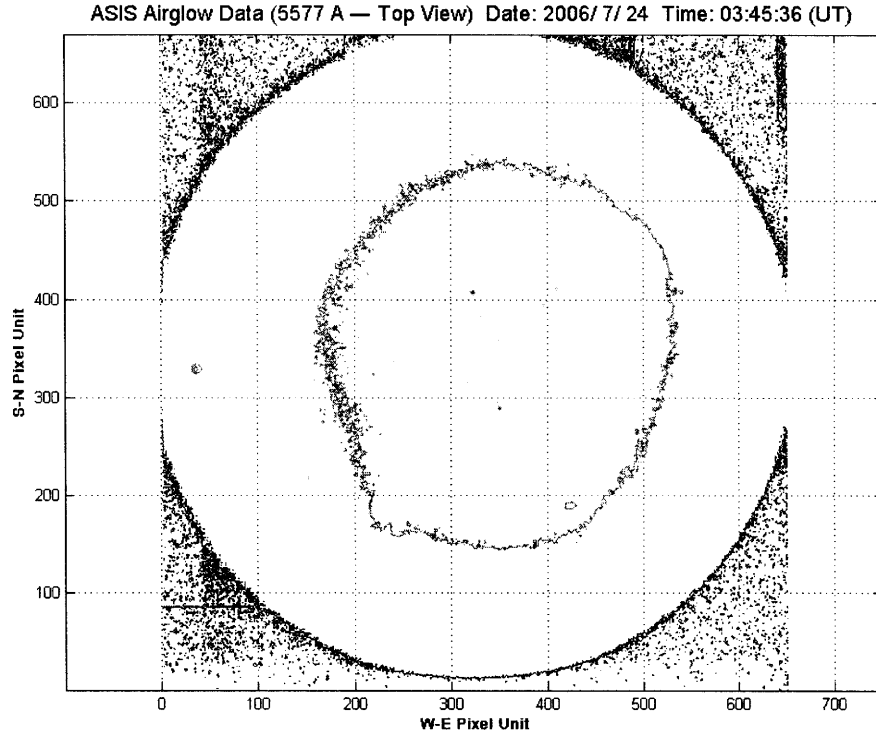


Figure A-4: Contour map of a sample airglow intensity data recorded using ASIS. The image edge is located at the transition between the area where the contour is clean and the area where clusters of random dark noise start to develop. Center pixel and image radius is determined through analytical curve fitting of the image edge.

under the square root is negative. A simple trick using Taylor expansion can be applied to avoid this difficulty. The approximated fitting function then becomes:

$$\begin{aligned}
 y &= c_{row} \pm \langle imrad \rangle \left[1 - \frac{(x - ccol)^2}{\langle imrad \rangle^2} \right]^{1/2} \\
 &\approx c_{row} \pm \langle imrad \rangle \left[1 - \frac{(x - ccol)^2}{2\langle imrad \rangle^2} - \frac{(x - ccol)^4}{8\langle imrad \rangle^4} - \frac{(x - ccol)^6}{16\langle imrad \rangle^6} - \dots \right]
 \end{aligned}
 \tag{A.7}$$

In this thesis, terms up to order $(x - ccol)^{12}/\langle imrad \rangle^{12}$ were retained in the fitting function to make sure that the expansion works for most part of the curve.

The results of curve fitting process for both lower and upper arcs are shown in Figure A-5. From the plots one can see that the fitting for the upper arc actually works better than that for the lower arc. This is also reflected in the values of reduced-

Table A.1: The values for the center pixel and the image radius that were obtained from the curve fitting of the image edge. Shown are the individual fitting parameter results from upper and lower arc, together with the weighed average of the two results.

	Upper Arc	Lower Arc	Weighted Average
$\langle imrad \rangle$	329.9 ± 0.8	337 ± 1	333 ± 1
$ccol$	322.6 ± 0.3	320.6 ± 0.5	322 ± 1
$crow$	351 ± 1	346 ± 2	349 ± 2

chi-squared for each cases. While this could be caused by some erroneous data points for the lower arc, it is also possible that the actual image edge itself is slightly non-circular for the lower arc. The inferred values for the center pixel locations ($crow$, $ccol$) and the image radius $\langle imrad \rangle$ are tabulated in Table A.1. With this fitting result, we have now determined all parameter values that are needed for the geocoordinate transformation.

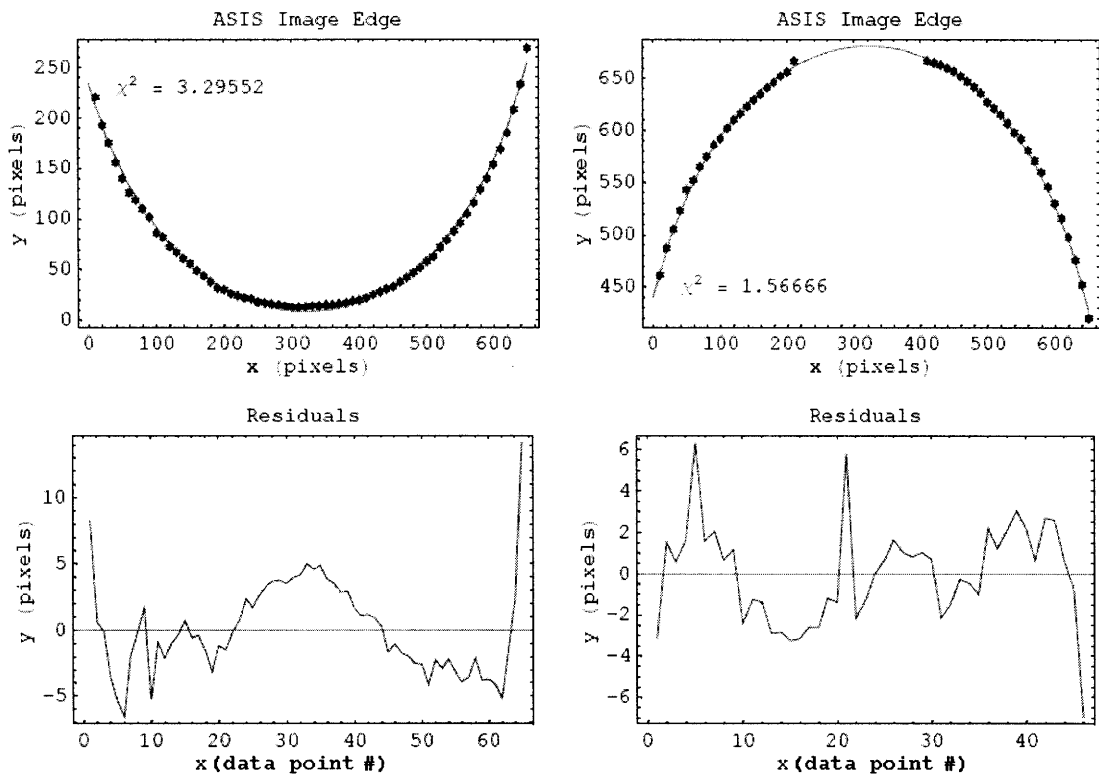


Figure A-5: Curve fitting results of ASIS image edge for the lower arc (left) and for the upper arc (right), respectively.

Appendix B

Airglow Structure Tracking

When airglow structures were seen to be moving across the all-sky imager's field of view, we would like to be able to accurately determine the direction and speed of this horizontal motion. Being able to do so will provide us with a very useful information that can be combined with other diagnostics result (e.g. ISR power profile) to learn more details about the observed plasma turbulence. Presented here is the description of a set of computational procedures that can be used to track airglow structures recorded by ASIS.

The airglow structure tracking procedures can be divided into three main stages:

1. Tracking/finding the location of airglow structures at a given time.
2. Deducing the direction of motion.
3. Calculating the speed of this horizontal motion.

The results from one particular stage will be used to perform the computation at the next stage. Thus, each stage will need to be completed before we can move onto the next stage.

The basic procedures for the first stage is illustrated in Figure B-1. When a moving airglow structure of interest starts to appear in the ASIS data, we will need to mark it so that we can track/locate it in each of the next few ASIS snapshots. In the reference ASIS snapshot, we will mark an airglow structure by constructing a rectangular frame

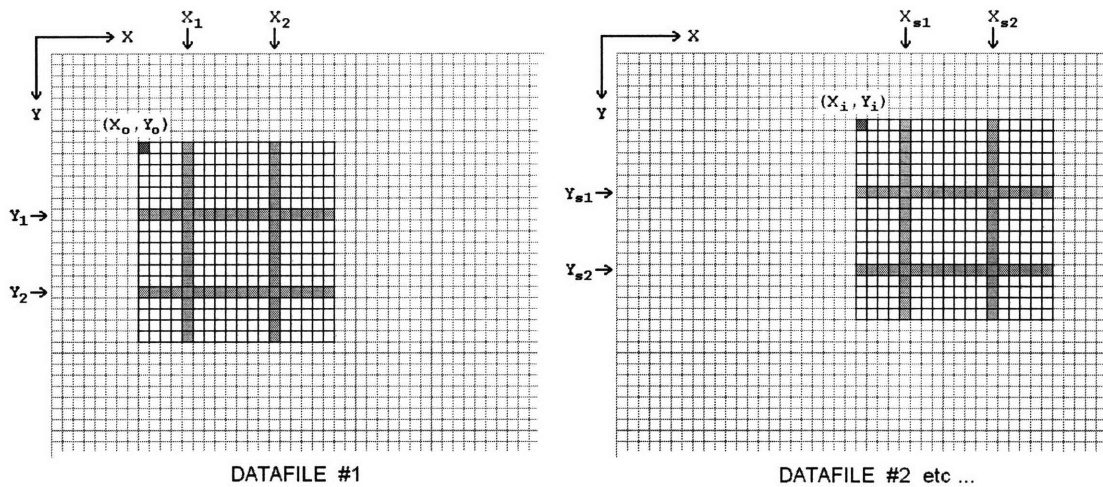


Figure B-1: Basic schematics of the airglow structure tracking procedures. The distinctive part of airglow structure is “locked-on” first in Datafile #1. We will then locate the new position of this structure in Datafile #2 onwards by scanning the “lock-on” frame around, looking for the best-matched pattern.

that properly encloses the distinctive part of this structure. Then, we are going to sample two horizontal slices (vector arrays \mathbf{Y}_1 and \mathbf{Y}_2) and two vertical slices (vector arrays \mathbf{X}_1 and \mathbf{X}_2) of the airglow structure. Once the airglow structure has been “locked-on”, we can start tracking it in the next few ASIS snapshots.

In each of the next ASIS snapshots, we are going to find the new location of the tracked airglow structure using the same frame that we had used to “lock-on” the structure in the first place. One corner of the tracking frame will be at coordinate (X_i, Y_i) , and we will be sampling two horizontal slices (vector arrays \mathbf{Y}_{s1} and \mathbf{Y}_{s2}) and two vertical slices (vector arrays \mathbf{X}_{s1} and \mathbf{X}_{s2}) from this frame, similar to what we did before. We then calculate a “chi-squared”:

$$\chi^2 = 1 + |\mathbf{X}_{s1} - \mathbf{X}_1|^2 + |\mathbf{X}_{s2} - \mathbf{X}_2|^2 + |\mathbf{Y}_{s1} - \mathbf{Y}_1|^2 + |\mathbf{Y}_{s2} - \mathbf{Y}_2|^2 \quad (\text{B.1})$$

and stored this “chi-squared” value in another data array.

We need to repeat the process of computing χ^2 for various (X_i, Y_i) . A sufficiently large portion of the ASIS snapshot has to be scanned to obtain a 2-D map of χ^2 values. We finally define a quantity called “likelihood” which is defined by $\equiv 1/\chi^2$. One can see that if the tracking frame is coincident with the tracked airglow structures, the

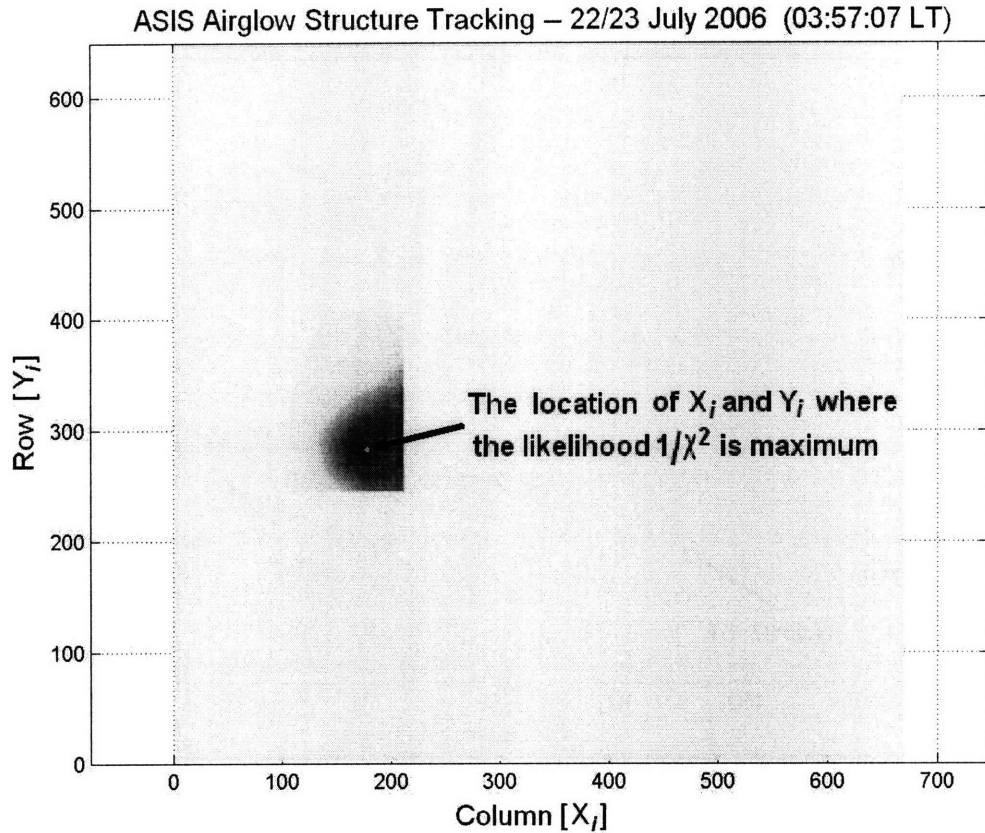


Figure B-2: A sample likelihood surface plot that was obtained after scanning an ASIS snapshot. In each ASIS snapshots following the reference snapshot, the tracked airglow structure position is found by locating the coordinate (X_i, Y_i) where the likelihood is maximum.

“chi-squared” will be minimum and the “likelihood” will be maximum. The official location of the tracked airglow structure is then set by finding the coordinate (X_i, Y_i) at which the likelihood $1/\chi^2$ is the largest. Figure B-2 shows a 2-D surface plot of the likelihood from an ASIS snapshots. The location (X_i, Y_i) where the likelihood is maximum tells us where the tracked airglow structure is located in a given ASIS snapshot.

After we determine (X_i, Y_i) where the likelihood is maximum in one ASIS snapshot, we need to move onto subsequent ASIS snapshots and repeat the process of computing likelihood for various locations and finding the location with the largest likelihood. Finally, we are going to obtain a set of data points specifying the location of the tracked airglow structures at each moment in time. In other words, we will

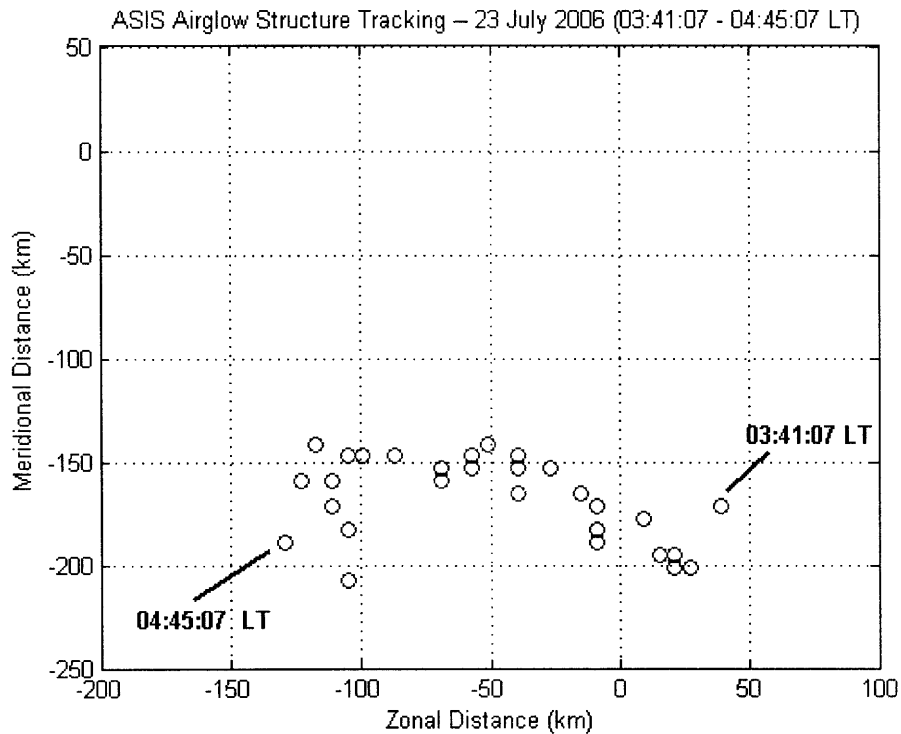


Figure B-3: A plot of the tracked airglow structure positions from a number of ASIS snapshots following a particular reference snapshot. This airglow trail is the end result of the first stage in our tracking procedures.

have a trail of the airglow motion. This is the end of the first stage in our tracking analysis. Figure B-3 shows a sample result of this repeated process, which will be used in the second stage of our airglow structure tracking procedures.

The goal of the second stage in our tracking procedures is to determine the overall direction of airglow motion based on the tracked locations from the first stage. To the lowest order, the overall airglow motion can be well approximated with a straight-line trajectory. In the cases where the airglow structures are actually turning or changing direction, the approximation may still apply provided that we are able to properly split the original trajectory into piecewise straight-line trajectory. In short, our task in the second stage is to perform linear regression to the trail of airglow motion that we have obtained from the first stage.

To optimize the linear regression for finding the overall straight-line trajectory, we will treat the airglow trails as data points of $y(x)$ if it is closer to east-west

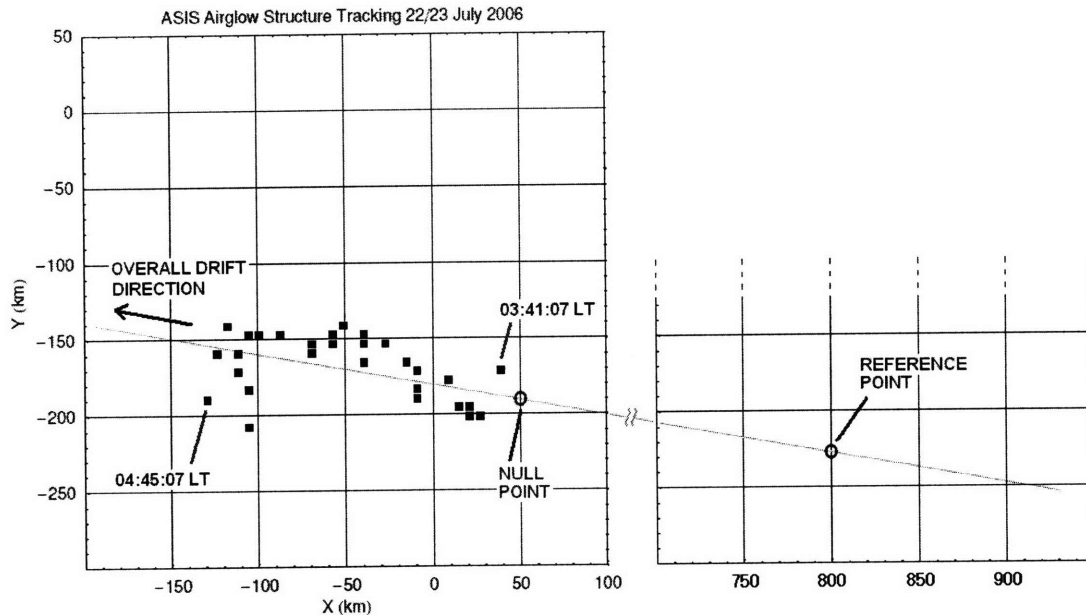


Figure B-4: A sample linear regression result in determining the overall airglow motion direction from the airglow trails. Also shown in the figure is a schematic illustration of the *reference point* and the *null point* that are used in the “projection” procedures as a preliminary step for determining the speed of airglow motion.

alignment. And conversely, we will treat the airglow trails as data points of $x(y)$ if it is closer to north-south alignment. This is necessary because standard linear regression only considers vertical discrepancy δy , while in finding path/trajectory we need to account for the overall discrepancy $\sqrt{\delta x^2 + \delta y^2}$ between the line and data points. Our treatment of discriminating between $y(x)$ and $x(y)$ for different trail alignment does not completely solve the problem, but it can significantly reduce possible errors that might happen in the extreme cases.

After the direction of airglow motion has been determined through linear regression, the last stage of our tracking procedure would be to determine the speed of this airglow motion. In order to do so, we need to “project” each data points in the airglow trail onto the fitted trajectory line, and determine how fast these points progress forward along the line. We will perform the “projection” numerically as follows: We will first compute the distances of each data points relative to a *reference point* (on the trajectory line) that is located far away. We will then subtract these distances by the distance between the *reference point* and the so-called *null point* (also on the

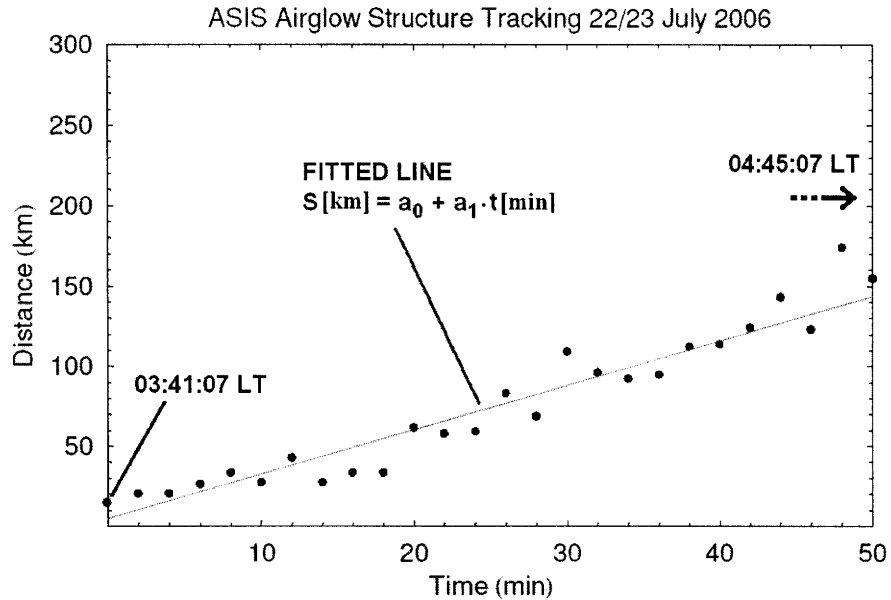


Figure B-5: Determining the airglow motion speed through curve fitting. Most of the time, we only need linear regression since the airglow motion speed is \sim constant.

trajectory line). Figure B-4 shows the result of the second stage in finding the overall trajectory, as well as a schematic illustration of the procedures for “projecting” each data points onto the line.

After projecting each data points in the airglow trail onto the trajectory line, we will have a set of data points for the distances (along the line) from the null point as a function of time. This tells us how far the airglow structure has progressed away from the null point at each instant. In most cases, the distances are most conveniently expressed in unit of kilometers [km], and the elapsed time in unit of minutes [min]. Assuming that the airglow structure is moving at a \sim constant speed, we can fit these data points into a straight line:

$$S[km] = a_0 + a_1 \cdot t[min] \tag{B.2}$$

and the airglow motion speed is directly given by the fitting parameter a_1 . Shown in Figure B-5 is a sample fitting result to determine the airglow motion speed, where the \sim constant speed approximation can be well justified. This calculation concludes our airglow structure tracking procedures.

Bibliography

- [1] J. Artru et al. (2005), *Ionospheric Detection of Gravity Waves Induced by Tsunamis*, *Geophys. J. Int.*, **160**, 840.
- [2] J. Artru, T. Farges, and P. Lognonne (2004), *Acoustic Waves Generated from Seismic Surface Waves: Propagation Properties Determined from Doppler Sounding Observation and Normal-modes Modeling*, *Geophys. J. Int.*, **158**, 1067.
- [3] Atmospheric Science Data Center, *Ceres Image: Oppressive Heat Wave Moves across United States*, NASA Langley Research Center (September 2006).
(http://eosweb.larc.nasa.gov/PRODOCS/ceres/featured_imagery/heatwave_2006.html)
- [4] P. Bauer (1975), *Theory of Waves Incoherently Scattered*, *Philosophical Transactions of the Royal Society of London, Series A, Mathematical and Physical Sciences*, Vol. 280, No. 1293, 167–191.
- [5] A.D. Belmont, D.G. Dartt, and M.S. Ullstad (1965), *The 10.7-cm Solar Flux and the 26-Month Oscillation*, *Journal of the Atmospheric Sciences*, **23**, 314–319.
- [6] P.A. Bernhardt (2002), *The Modulation of Sporadic-E Layers by Kelvin-Helmholtz Billows in the Neutral Atmosphere*, *Journal of Atmospheric and Solar-Terrestrial Physics*, **64**, 1487–1504.
- [7] R.L. Bishop (2006), *Arecibo Observations of Ionospheric Perturbations Associated with the Passage of Tropical Storm Odette*, *Journal of Geophysical Research*, **111**, A11320.

- [8] H.C. Carlson, Jr. and A. Egeland, in *Introduction to Space Physics*, Editors: M.G. Kivelson & C.T. Russell (Cambridge, 1995).
- [9] J.W. Chamberlain, *Physics of the Aurora and Airglow* (Academic Press, New York and London, 1961).
- [10] P.F. Checcacci, *Measurements of Total Electron Content by Means of Satellite Radio Emissions*, Physics of the Upper Atmosphere (Editrice Compositori, 1970).
- [11] F.W. Cole, *Introduction to Meteorology, 3rd Ed.* (John Wiley & Sons, 1980).
- [12] J.P. Dougherty and D.T. Farley (1960), *A Theory of Incoherent Scattering of Radio Waves by a Plasma*, Proceedings of the Royal Society of London. Series A, Mathematical and Physical Sciences, Vol. 259, No. 1296, 79–99.
- [13] D.T. Farley, J.P. Dougherty, and D.W. Barron (1961), *A Theory of Incoherent Scattering of Radio Waves by a Plasma II: Scattering in a Magnetic Field*, Proceedings of the Royal Society of London, Series A, Mathematical and Physical Sciences, Vol. 263, No.1313, 238–258.
- [14] A.A. Gore, Jr., *Testimony of the Honorable Al Gore before the US House of Representatives and the Science & Technology Committee*, US House of Representatives (21 March 2007).
- [15] C.O. Hines (1960), *Internal Gravity Waves at Ionospheric Heights*, Canadian Journal of Physics **38**, 1441–1481.
- [16] W.H. Hooke (1968), *Ionospheric Irregularities Produced by Internal Atmospheric Gravity Waves*, Journal of Atmospheric and Terrestrial Physics, **30**, 795–823.
- [17] M.C. Kelley, *The Earth's Ionosphere: Plasma Physics and Electrodynamics* (Academic Press, 1989).
- [18] A. Labno et al. (2007), *Whistler-Mode Wave Interactions with Ionospheric Plasmas over Arecibo*, Journal of Geophysical Research, **112**, A03306.
doi:10.1029/2007GL029807

- [19] J. Lastovicka (2006), *Forcing of the Ionosphere by Waves from Below*, Journal of Atmospheric and Solar-Terrestrial Physics, **68**, 479–497.
- [20] M.C. Lee and S.P. Kuo (1984), *Earth's Magnetic Field Perturbations as the Possible Environmental Impact of the Conceptualized Solar Power Satellite*, Journal of Geophysical Research, **89**, A12.
- [21] M.C. Lee et al. (1998), *Generation of Large Sheet-like Ionospheric Plasma Irregularities at Arecibo*, Geophysical Research Letters, **25**, 579.
- [22] M.C. Lee et al., *Did Tsunami-Launched Gravity Waves Trigger Ionospheric Turbulence over Arecibo?*, to be published in Journal of Geophysical Research (2007).
- [23] E. Manzini and K. Hamilton (1992), *Middle Atmospheric Travelling Waves Forced by Latent and Convective Heating*, Journal of the Atmospheric Sciences, **50**, 14.
- [24] C.J. Nappo, *An Introduction to Atmospheric Gravity Waves* (Academic Press, 2002).
- [25] NASA Earth Observatory Newsroom, *Heat Wave in North America and Western Europe*, National Aeronautics and Space Administration (August 2006).
(http://earthobservatory.nasa.gov/Newsroom/NewImages/images.php3?img_id=17355)
- [26] National Climatic Data Center, *Daily US ASOS Temperature Maps*, National Oceanic and Atmospheric Administration.
(<http://www.ncdc.noaa.gov/oa/climate/dusam/index.php>)
- [27] National Hurricane Center, *Atlantic Hurricane Track Chart*, National Oceanic and Atmospheric Administration (2006).
(<http://www.aoml.noaa.gov/hrd/hurdat/Track-Maps.html>)
- [28] NOAA's National Weather Service, *Heat Wave and Severe Weather July 2006*, National Oceanic and Atmospheric Administration (August 2006).
(http://www.crh.noaa.gov/lx/?n=july_2006)

- [29] M.J. Nicolls et al. (2004), *Imaging the Structure of a Large-scale TID Using ISR and TEC Data*, Geophysical Research Letters, **31**, 1029.
- [30] D. O'Sullivan and T.J. Dunkerton (1995), *Generation of Inertia-Gravity Waves in a Simulated Life Cycle of Baroclinic Instability*, Journal of the Atmospheric Sciences, **52**, 21.
- [31] R. Pradipta et al. (2007), *Electron Precipitation from the Inner Radiation Belt above Arecibo*, Geophysical Research Letters, **34**, L08101.
doi:10.1029/2007GL029807
- [32] R. Pradipta et al. (2007), PARS 2007 Summer Experiments (I) and (II).
- [33] W. Rideout and A.J. Coster (2006), *Automated GPS Processing for Global Total Electron Content Data*, GPS Solution, **10**, 219–228.
- [34] K. Sato, T. Kumakura, and M. Takahashi (1998), *Gravity Waves Appearing in a High-Resolution GCM Simulation*, Journal of the Atmospheric Sciences, **56**, 8.
- [35] G.L. Siscoe, *Solar System Magnetohydrodynamics*, Solar-Terrestrial Physics: Principles and Theoretical Foundations (D. Reidel Publishing Co., 1983).
- [36] Space Physics Interactive Data Resource (SPIDR), National Oceanic and Atmospheric Administration.
(<http://spidr.ngdc.noaa.gov/spidr/index.jsp>)
- [37] K.F. Tapping and B. DeTracey (1990), *The Origin of the 10.7 cm Flux*, Solar Physics, **127**, 321–332.
- [38] K.C. Yeh and C.H. Liu, *Theory of Ionospheric Waves* (Academic Press, New York and London, 1972).